Quantitative Anisotropy Imaging based on Spectral Interferometry

Chengshuai Li

Dissertation submitted to the faculty of the Virginia Polytechnic Institute and State University in partial fulfillment of the requirements for the degree of

Doctor of Philosophy

In

Electrical Engineering

Yizheng Zhu, Chairman

Ting-Chung Poon

Hans D Robinson

Ahmad Safaai-Jazi

Anbo Wang

Oct 9, 2018

Blacksburg, Virginia

Keywords: spectral interferometry, quantitative phase imaging, quantitative polarization microscopy, frequency estimation, sensitivity analysis.

Quantitative Anisotropy Imaging based on Spectral Interferometry

Chengshuai Li

Abstract

Spectral interferometry, also known as spectral-domain white light or low coherence interferometry, has seen numerous applications in sensing and metrology of physical parameters. It can provide phase or optical path information of interest in single shot measurements with exquisite sensitivity and large dynamic range. As fast spectrometer became more available in 21st century, spectral interferometric techniques start to dominate over time-domain interferometry, thanks to its speed and sensitivity advantage.

In this work, a dual-modality phase/birefringence imaging system is proposed to offer a quantitative approach to characterize phase, polarization and spectroscopy properties on a variety of samples. An interferometric spectral multiplexing method is firstly introduced by generating polarization mixing with specially aligned polarizer and birefringence crystal. The retardation and orientation of sample birefringence can then be measured simultaneously from a single interference spectrum. Furthermore, with the addition of a Nomarski prism, the same setup can be used for quantitative differential interference contrast (DIC) imaging. The highly integrated system demonstrates its capability for noninvasive, label-free, highly sensitive birefringence, DIC and phase imaging on anisotropic materials and biological specimens, where multiple intrinsic contrasts are desired.

Besides using different intrinsic contrast regime to quantitatively measure different biological samples, spectral multiplexing interferometry technique also finds an exquisite match in imaging single anisotropic nanoparticles, even its size is well below diffraction limit. Quantitative birefringence spectroscopy measurement over gold nanorod particles on glass substrate demonstrates that the proposed system can simultaneously determine the polarizability-induced birefringence orientation, as well as the scattering intensity and the phase differences between major/minor axes of single nanoparticles. With the anisotropic nanoparticles' spectroscopic polarizability defined prior to the measurement with calculation or simulation, the system can be further used to reveal size, aspect ratio and orientation information of the detected anisotropic nanoparticle.

Alongside developing optical anisotropy imaging systems, the other part of this research describes our effort of investigating the sensitivity limit for general spectral interferometry based systems. A complete, realistic multi-parameter interference model is thus proposed, while corrupted by a combination of shot noise, dark noise and readout noise. With these multiple noise sources in the detected spectrum following different statistical behaviors, Cramer-Rao Bounds is derived for multiple unknown parameters, including optical pathlength, system-specific initial phase, spectrum intensity as well as fringe visibility. The significance of the work is to establish criteria to evaluate whether an interferometry-based optical measurement system has been optimized to its hardware best potential.

An algorithm based on maximum likelihood estimation is also developed to achieve absolute optical pathlength demodulation with high sensitivity. In particular, it achieves Cramer-Rao bound and offers noise resistance that can potentially suppress the demodulation jump occurrence. By simulations and experimental validations, the proposed algorithm demonstrates its capability of achieving the Cramer-Rao bound over a large dynamic range of optical pathlengths, initial phases and signal-to-noise ratios.

Quantitative Anisotropy Imaging based on Spectral Interferometry

Chengshuai Li

General Audience Abstract

Optical imaging is unique for its ability to use light to provide both structural and functional information from microscopic to macroscopic scales. As for microscopy, how to create contrast for better visualization of detected objects is one of the most important topic. In this work, we are aiming at developing a noninvasive, label-free and quantitative imaging technique based on multiple intrinsic contrast regimes, such as intensity, phase and birefringence.

Spectral multiplexing interferometry method is firstly introduced by generating spectral interference with polarization mixing. Multiple parameters can thus be demodulated from single-shot interference spectrum. With Jones Matrix analysis, the retardation and orientation of sample birefringence can be measured simultaneously. A dual-modality phase/birefringence imaging system is proposed to offer a quantitative approach to characterize phase, polarization and spectroscopy properties on a variety of samples. The high integrated system can not only deliver label-free, highly sensitive birefringence, DIC and phase imaging of anisotropic materials and biological specimens, but also reveal size, aspect ratio and orientation information of anisotropic nanoparticles of which the size is well below diffraction limit.

Alongside developing optical imaging systems based on spectral interferometry, the other part of this research describes our effort of investigating the sensitivity limit for general spectral interferometry based systems. The significance of the work is using Cramer-Rao Bounds to establish criteria to evaluate whether an optical measurement system has been optimized to its hardware best potential. An algorithm based on maximum likelihood estimation is also developed to achieve absolute optical pathlength demodulation with high sensitivity. In particular, it achieves Cramer-Rao bound and offers noise resistance that can potentially suppress the demodulation jump occurrence.

To my Parents and my Wife

Acknowledgement

It has been a few years since I came to US and started my PhD study at Virginia Tech. It was a long journey which involves some hard working day and night, some struggles in front of obstacles and of course a lot of rewarding moments. I really appreciate this experience, not only for the academic work completed, but also for the people I've been worked with and the things I've learned.

Thank you, Dr. Yizheng Zhu, for bringing me here and offering your support along the way. Your passion and dedication in research really helped me to grow. It was truly my honor to work with you for the past 5 years, and I really appreciate the motivation, care and patience you kindly shared with me.

I also want to take a moment to thank my committee members, Dr. Anbo Wang, Dr. Hans Robinson, Dr. Ting-Chung Poon, and Dr. Ahmad Safaai-Jazi. Thanks for your insightful comments and practical suggestions into my projects. I'm also feeling grateful to some faculty members with project collaboration: Dr. Kiho Lee, Dr. Raffaella De Vita, Dr. Yong Xu and Dr. Michael Klemba. Thanks for all your time and effort involved.

I also want to say thank you for all the wonderful lab members and colleagues I've been worked with: Shichao Chen, Zhixing He, Dr. Aram Lee, Dr. Dong Wang, Dr. Ting Tan, Junghyun Ryu, Joe Thomas, Ruibo Shang, Jacob Black, Dr. Fang Liu, Dr. Xiaona Li, Ruohan Zhou, Sizhe Guo, Dr. Bo Dong, Dr. Zhihao Yu, Dr. Chennan Hu, Dr. Lingmei Ma, Dr. Di Hu, Dr. Yuanyuan Guo, Dr. Amiya Behera, Dr. Li Yu, Ziang Feng, Yunzhi Wang, Shuo Yang, Jiaji He, Scott Zhang, etc. It made my research life so easy with your professionalism and kindness.

In addition, I owe my thanks to a lot of friends I met in Blacksburg. Thanks for the company. I feel so lucky to share this enjoyable journey with you, and wish you all a bright future.

Last but not least, I want to say thank you to my dear parents, Changqing Li and Hui Jiang and my sister, Bo Shao. I'll not be here without your unconditional support. And Dr. Guigui Wan, thank you for being my best friend and my wife. Meeting you on my very first day in Blacksburg is the best thing happened to me in my life. I can't wait to explore this world with you.

Table of Contents

List of Figures

List of Tables

Chapter 1 Introduction

1.1. Motivation

The utility of light as a tool to either see things from distance or magnify minuscule objects to be visualized is largely based on its noninvasive nature, which has been playing an irreplaceable role in scientific investigations. Optical imaging is unique in its ability to provide both structural and functional information from microscopic to macroscopic scales. As for microscopy, how to create contrast for better visualization perhaps is the most important area where much of the effort has been devoted to [1].

There are mainly two kinds of contrast mechanisms: exogenous and endogenous. Exogenous contrast is created by attaching contrast agents attached to the structures of interest, such as chemically bonded stains and fluorophores [2]. On the other hand, the endogenous (intrinsic) contrast is generated by the inner physical structures and/or chemical composition of the objects [3], such as the attenuation from light scattering observed with conventional microscopes.

Exogenous contrast agents enable the labeling of particular structures and introduce high quality imaging contrast, which is widely used in pathology and cell biology. Additionally, the recent development of some super-resolution microscopy techniques, such as SIM (Structured illumination microscopy) [4], STED (Stimulated emission depletion) [5, 6], PALM (photo activated localization microscopy) [7], and STORM (Stochastic optical reconstruction microscopy) [8], can even exceed the resolution barrier set by optical diffraction. However, adding foreign chemicals is bound to affect the function of original biological objects. Fluorescence molecules have been proven to be toxic to cells and also to suffer from photo-bleaching, which limits their applications on live cell imaging [9].

In the following research, we seek to develop label-free, quantitative imaging techniques using the objects' intrinsic phase contrast, aimed at examining live cells in their natural state without killing, fixing or staining them. Specifically, we investigate label-free multimodal contrast imaging based on QPI and quantitative polarized light microscopy (PLM). In addition, we will take the fundamental sensitivity advantage of spectral interferometry and study its demodulation algorithms for quantitative phase imaging (QPI).

1.2. Literature Review

1.2.1. Qualitative phase imaging

The main obstacle in imaging optically thin biological specimens using endogenous contrast is that, generally, they do not exhibit sufficient contrast if only light intensity is observed. Compared with transmitted or scattered light intensity, optical phase is more critical in imaging these samples [10]. Even a thin semi-transparent tissue can significantly modify the wavefront of the input light, which can then strongly enhance image contrast and reveal details of cellular structures.

Phase contrast microscopy (PCM) was developed by Zernike [11] in 1930s with the interferogram generated by unscattered incident light and scattered light. The phase of unscattered light is shifted by a quarter wavelength to produce enhanced contrast. PCM significantly improves the visualization of transparent specimens without affecting resolution, and can reveal inner structure of transparent specimens without exogenous contrast agents. Another contrast-enhanced microscopy technique, differential interference contrast (DIC) microscopy, was introduced by Nomarski in 1950s [12]. DIC produces contrast by visually showing the directional phase gradients instead of the phase itself. Nowadays, PCM and DIC have become standard modalities on commercial microscopes. They convert light phase or phase derivatives to changes in amplitude, which can be visualized as difference in brightness.

In 1940s, in-line holography was first demonstrated by Gabor [13] introducing the use of complex analytic signals (both amplitude and phase instead of usual intensity) to describe optical field in the form of electromagnetic waves. Off-axis holography [14] had also been demonstrated to further improve the signal to noise ratio (SNR). After discarding single side of frequency components in the original signal's Fourier interferogram, the amplitude and phase information of the light field can be recorded from a hologram at the same time. Advances in the information theory and technological progress in digital recording devices brought holography technique into a new digital holography era [15-17], with the speed and performance of numerical processing greatly improved by 2D fast Fourier transform (FFT) [18].

Although these methods represent significant advances in microscopy, they are, however, inherently qualitative and incapable of quantifying the phase delay induced by the image object

because of the nonlinear mixing of phase and intensity in image formation. Therefore, these methods are largely recognized as visualization techniques rather than quantitative approaches.

Quantitative phase imaging (QPI) [19, 20], instead, takes the approach of measuring the optical phase/pathlength delay introduced by specimens quantitatively. Two optical beams are used by most QPI systems, which are usually generated by the same source to exploit their coherence. Two beams will be superimposed later to cause interference: an object beam that transmits through or reflects back from the sample which carries the sample footprint and another beam offers as a reference. In fact, the concept of QPI can be seen as a combination of interferometry, microscopy, and holography techniques.

1.2.2. Full field quantitative phase imaging

Full field quantitative phase imaging takes holography one step further and uses interferometry to extract the phase information separately from its amplitude. Full field QPI techniques mainly fall into two categories: off-axis and phase-shifting (on-axis).

In off-axis configuration [21-23], a small tilt angle is set between the reference beam and the sample beam, which can create fringe patterns in the interferogram along the tilt direction. Complex signals can be reconstructed from a single acquisition of real full-field image using Hilbert transform. Based on the phase information decoded with Fourier domain analysis, the optical pathlength profile over the sample can be achieved. Due to its single-shot nature, off-axis QPI technique can measure phase profile at a high acquisition speed.

Phase-shifting configuration [24, 25], on the other hand, needs to capture multiple acquisitions with certain modulated phase changes between the sample and the reference beam, while the optical phase difference being calculated comparing different frames. Two interference beams can both propagate along the main axis (on-axis). In addition, the phase differences between different frames are normally the same, which can facilitate further linear calculation between frames. With calculations performed only in the time domain between different frames point-by-point, phase-shifting technique, compared with off-axis configuration, can maintain diffraction-limit resolution and large field of view at the expense of acquisition speed. Recently, wavelength shifting interferometry (WSI) [26] was also proposed to improve imaging speed by switching to use several wavelength bands.

Generally speaking, full field QPI techniques can achieve high temporal resolution which can be used for studying fast dynamic phenomenon. However, the spatial sensitivity can be severely corrupted by foreign particles or unexpected debris in the detecting range of light source. For example, laser illumination, typically equipped with coherence length longer than 20cm, can easily generate speckle noises, and thus severely limits the image contrast and lowers the spatial sensitivity [27]. Using broadband illumination fields, or equivalently, short coherence light can remove the speckle structure almost entirely.

As an example, spatial light interference microscopy (SLIM) [28] was developed by Popescu's group based on PCM with white light illumination. A liquid crystal phase modulator was incorporated into a conventional phase contrast microscope, introducing additional spatial modulation to the image field, as in traditional phase-shifting interferometry. Speckle-free quantitative phase imaging can be achieved at high spatial and temporal sensitivity. Additionally, optical depth sectioning can also be achieved by short coherence length of white light, which enables white-light diffraction tomography [29].

1.2.3. Spectral domain quantitative phase imaging

Spectral interferometry has its roots in the long, rich history of low coherence interferometry (LCI). Since the 1960s, LCI has seen numerous applications in sensing and metrology of physical parameters [30-32]. Later, it was introduced into biomedical imaging as the basis of OCT [33]. As an intensity-based interferometric technique, OCT utilizes low coherence broadband light sources, and can perform cross-sectional tomographic imaging. Early time domain OCT techniques need mechanical scanning, which limits the acquisition speed and affects the phase stability in the measurements. As fast spectrometers became more available in the 2000s, spectral interferometric technique starts to dominate, thanks to its speed and sensitivity advantages [34-36].

Fourier domain OCT offers a fast alternative to acquire depth-resolved signals and leads to the development of point-scanning QPI. In 2005, two independent groups [37, 38] reported on using spectra domain OCT to achieve QPI for live cell imaging. They employed a point scanning, common-path configuration, and the phase changes were extracted from the interference between the top and bottom reflections of the sample chamber.

Compared with full-field implementation, point-scanning phase microscopy based on spectral-domain low-coherence interferometry (SD-LCI) can improve phase sensitivity by more than an order of magnitude [39]. Such sensitivities are keys for quantifying minute cellular dynamics. The drawback of point-scanning QPI is the relatively limited temporal resolution, however, SD-LCI not only offers super resolution in the measurement of optical pathlength, but also provides possibility to extract spectroscopic information from the interference spectrum acquired at each geometric position.

Another advantage of spectral interferometry based techniques is spectral encoding, originally proposed to improve the speed of confocal reflection microscopy [40]. One spatially spectral encoding approach uses a grating to spread a line illumination and encodes sample image in the spectrum. The technique has found applications in endoscopy for reduced scan complexity [41], and in parallel OCT to improve speed but at the expense of severely degraded spatial resolution [42]. Similar ideas can also be borrowed from the theory of communication signal processing to take advantage of the high information capacity of spectral interferometry, which we will discuss in Chapter 4.

1.2.4. Polarized light microscopy and birefringence imaging

Besides above phase imaging techniques, polarization light microscopy (PLM) [43] has also been used to analyze the a specimen's anisotropic properties when interacting with optical field, free of exogenous dyes and fluorescent markers. Two polarizers with their polarizing axes orthogonal to each other are often used to examine the sample birefringence for conventional PLM systems, with the one after source normally called polarizer and the latter after the sample called analyzer. For the areas that the sample doesn't change the polarization state of incident light, no light will go through the analyzer, which makes the corresponding image to be dark. However, if the sample birefringence exists or the specimen generates scattered light with random polarizing direction, certain fraction of light can pass through the analyzer. PLM can introduce enhanced image contrast on birefringent samples or optical path boundaries, when compared with bright-field or phase contrast techniques.

Over the years, several quantitative PLM techniques have been proposed to exploit the overwhelming contrast strength when using polarized light as illumination. To quantitatively

determine the birefringence, one needs to determine not only the pathlength retardation but also the azimuth angle of slow axis. To demodulate both parameters, most proposed imaging systems use some polarizing elements rotated mechanically [44-46] and/or a variable retarder controlled electrically [47]. An elegant birefringence LC-PolScope system was proposed and commercialized by researchers at Marine Biological Laboratory [48] with a circularly polarized light illumination and a liquid crystal universal compensator. The universal compensator is built from two variable electro-optical retarders and a linear polarizer and is able to generate any polarization in need. Generally, five images were recorded with different polarization analyzer settings, which can be further demodulated to produce images of birefringence retardance and slow axis orientation.

The advantage of PLM lies in the unique contrast when examining the alignment of molecular bonds or fine structural form in natural objects and synthetic indicators, including biological structures such as collagen [49], cell membrane/wall [50, 51], mitotic/meiotic spindle [52-54], red blood cell [55], and brain fiber tracts [56]. System stability and reproducibility are essential in order to achieve high accuracy and sensitivity. However, most birefringence imaging systems reported are based on multiple acquisitions, which limits system speed and hinders their applications to study fast dynamics.

1.2.5. Multimodal imaging systems

The task of optical imaging system is to evaluate target sample based on its morphology and functions, which can lend optical imaging modalities based on different contrast mechanisms enormous advantage over single-function ones. However, designing a multimodal imaging system often involves challenges in multiple respects, from theory/performance to hardware/compactness.

A highly integrated microscope was reported by Boppart's group [57] for combining optical coherence microscopy (OCM) with multiphoton microscopy (MPM). Both back scattering and fluorescence contrasts have been used for 3D functional imaging of cells.

There are also several multimodal imaging systems utilizing quite different contrast regimes from our research and will not be discussed in details here, such as the combination of MPM with anti-Stokes Raman scattering [58], or OCT with photoacoustic microscopy (PAM)

[59]. In the following research, we still seek to make full use of intrinsic contrasts of the imaging object to obtain as much information as possible.

1.3. Research Overview

In Chapter 2, we propose an interferometric spectral multiplexing method for measuring birefringent specimens with simple configuration and high sensitivity. The retardation and orientation of sample birefringence are simultaneously encoded onto two spectral carrier waves, generated interferometrically by a birefringent crystal through polarization mixing. With 2D raster scanning, single-shot birefringence measurements are demonstrated on a regenerated cellulose dialysis tubing film sample.

Chapter 3 presents a multi-modality birefringence/phase imaging system, with the addition of a Nomarski prism. The approach is analyzed theoretically with Jones calculus and validated experimentally with malaria-infected red blood cells. Inherit from point-scanning spectral-domain interferometry, the proposed system is capable of doing quantitative birefringence, DIC and phase imaging with exquisite sensitivity on weakly birefringent or scattered samples.

Based on spectral multiplexing interfereometry technique, Chapter 4 presents quantitative birefringence spectroscopy measurement on gold nanorod particles. Simultaneous quantification of orientation and spectroscopy can be used to determine single nanorod direction as well as to infer size/aspect ratio information, even when the nanorod particle size is well below diffraction limit.

In Chapter 5, a complete, realistic multi-parameter interference model is firstly built to investigate the fundamental sensitivity limit in optical pathlength estimation with a given spectral interferometry system. The Fisher information matrix and Cramer-Rao bounds are derived for all model parameters, including intensity, visibility, optical pathlength (frequency) and initial phase.

In Chapter 6, we develop a new spectral interference signal demodulation algorithm based on maximum likelihood estimation to achieve Cramer-Rao bound for absolute optical pathlength demodulation, over a large dynamic range of optical pathlength, initial phases and

signal-to-noise ratios. The advantage of proposed algorithm has been verified with both simulations and experiments, showing high sensitivity and noise resistance.

Conclusion and future work will be discussed in Chapter 7.

References

[1] "Milestones in light microscopy," *Nature Cell Biology,* vol. 11, no. 10, p. 1165, Oct 2009.

[2] R. Tsien, "The green fluorescent protein," *Annual Review of Biochemistry,* vol. 67, pp. 509-544, 1998.

[3] J. Goodman, *Introduction to Fourier optics*. Roberts and Company Publishers, 2005.

[4] M. Gustafsson, "Surpassing the lateral resolution limit by a factor of two using structured illumination microscopy," *Journal of Microscopy-Oxford,* vol. 198, pp. 82-87, May 2000.

[5] S. Hell and J. Wichmann, "Breaking the diffraction resolution limit by stimulated emission: stimulated-emission-depletion fluorescence microscopy," *Optics Letters,* vol. 19, no. 11, pp. 780-782, Jun 1994.

[6] T. Klar and S. Hell, "Subdiffraction resolution in far-field fluorescence microscopy," *Optics Letters,* vol. 24, no. 14, pp. 954-956, Jul 1999.

[7] E. Betzig *et al.*, "Imaging intracellular fluorescent proteins at nanometer resolution," *Science,* vol. 313, no. 5793, pp. 1642-1645, Sep 2006.

[8] M. Rust, M. Bates, and X. Zhuang, "Sub-diffraction-limit imaging by stochastic optical reconstruction microscopy (STORM) ," *Nature Methods,* vol. 3, no. 10, pp. 793-795, Oct 2006.

[9] J. Lippincott-Schwartz and G. Patterson, "Development and use of fluorescent protein markers in living cells," *Science,* vol. 300, no. 5616, pp. 87-91, Apr 2003.

[10] M. Born and E. Wolf, *Principles of optics: electromagnetic theory of propagation, interference and diffraction of light*. Elsevier, 2013.

[11] F. Zernike, "Phase contrast, a new method for the microscopic observation of transparent objects," *Physica,* vol. 9, no. 7, pp. 686-698, Jul 1942.

[12] G. Nomarski, "Differential microinterferometer with polarized waves," *J. Phys. Radium,* vol. 16, no. 9, pp. 9S-11S, 1955.

[13] D. Gabor, "A new microscopic principle," *Nature,* vol. 161, no. 4098, pp. 777-778, 1948.

[14] E. N. Leith and J. Upatnieks, "Reconstructed wavefronts and communication theory," *Journal of the Optical Society of America,* vol. 52, no. 10, p. 1123, 1962.

[15] B. R. Brown and A. W. Lohmann, "Complex spatial filtering with binary masks," *Applied Optics,* vol. 5, no. 6, p. 967, 1966.

[16] J. W. Goodman and R. W. Lawrence, "Digital image formation from electronically detected holograms", *Applied Physics Letters,* vol. 11, no. 3, p. 77, 1967.

[17] T.-C. Poon, *Digital holography and three-dimensional display: Principles and Applications*. Springer Science & Business Media, 2006.

[18] J. Cooley and J. Tukey, "An Algorithm for the Machine Calculation of Complex Fourier Series," *Mathematics of Computation,* vol. 19, no. 90, pp. 297-301, 1965.

[19] G. Popescu, "The power of imaging with phase, not power," *Physics today,* vol. 70, no. 5, pp. 35-40, 2017.

[20] Y. Park, C. Depeursinge, and G. Popescu, "Quantitative phase imaging in biomedicine," *Nature Photonics,* vol. 12, no. 10, pp. 578-589, Oct 2018.

[21] M. Takeda, H. Ina, and S. Kobayashi, "Fourier-transform method of fringe-pattern analysis for computer-based topography and interferometry", *Journal of the Optical Society of America,* vol. 72, no. 1, pp. 156-160, 1982.

[22] U. Schnars and W. Juptner, "Direct recording of holograms by a CCD target and numerical reconstruction," *Applied Optics,* vol. 33, no. 2, pp. 179-181, Jan 1994.

[23] E. Cuche, F. Bevilacqua, and C. Depeursinge, "Digital holography for quantitative phase-contrast imaging," *Optics Letters,* vol. 24, no. 5, pp. 291-293, Mar 1999.

[24] D. Zicha and G. A. Dunn, "An image processing system for cell behaviour studies in subconfluent cultures," *Journal of Microscopy-Oxford,* vol. 179, pp. 11-21, Jul 1995.

[25] D. Hogenboom, C. DiMarzio, T. Gaudette, A. Devaney, and S. Lindberg, "Three-dimensional images generated by quadrature interferometry," *Optics Letters*, vol. 23, no. 10, pp. 783-785, May 1998.

[26] S. Chen, C. Li, and Y. Zhu, "Low-coherence wavelength shifting interferometry for high-speed quantitative phase imaging," *Optics Letters*, vol. 41, no. 15, pp. 3431-3434, Aug 2016.

[27] J. Goodman, *Speckle phenomena in optics: theory and applications*. Roberts and Company Publishers, 2007.

[28] Z. Wang *et al.*, "Spatial light interference microscopy (SLIM)," *Optics Express*, vol. 19, no. 2, pp. 1016-1026, Jan 2011.

[29] T. Kim *et al.*, "White-light diffraction tomography of unlabelled live cells," *Nature Photonics*, vol. 8, no. 3, pp. 256-263, Mar 2014.

[30] Y. Zhu and A. Wang, "Miniature fiber-optic pressure sensor," *IEEE Photonics Technology Letters*, vol. 17, no. 2, pp. 447-449, 2005.

[31] A. Wang, H. Xiao, J. Wang, Z. Wang, W. Zhao, and R. May, "Self-Calibrated Interferometric-Intensity-Based Optical Fiber Sensors," *Journal of Lightwave Technology*, vol. 19, no. 10, p. 1495, Oct 2001.

[32] J. Schwider and L. Zhou, "Dispersive interferometric profilometer," *Optics Letters*, vol. 19, no. 13, pp. 995-997, Jul 1994.

[33] D. Huang *et al.*, "Optical coherence tomography," *Science*, vol. 254, no. 5035, pp. 1178-1181, Nov 1991.

[34] M. Choma, M. Sarunic, C. Yang, and J. Izatt, "Sensitivity advantage of swept source and Fourier domain optical coherence tomography," *Optics Express*, vol. 11, no. 18, pp. 2183-2189, Sep 2003.

[35] J. de Boer, B. Cense, B. Park, M. Pierce, G. Tearney, and B. Bouma, "Improved signal-to-noise ratio in spectral-domain compared with time-domain optical coherence tomography," *Optics Letters*, vol. 28, no. 21, pp. 2067-2069, Nov 2003.

[36] R. Leitgeb, C. Hitzenberger, and A. Fercher, "Performance of fourier domain vs. time domain optical coherence tomography," *Optics Express*, vol. 11, no. 8, pp. 889-894, Apr 2003.

[37] M. Choma, A. Ellerbee, C. Yang, T. Creazzo, and J. Izatt, "Spectral-domain phase microscopy," *Optics Letters*, vol. 30, no. 10, pp. 1162-1164, May 2005.

[38] C. Joo, T. Akkin, B. Cense, B. Park, and J. de Boer, "Spectral-domain optical coherence phase microscopy for quantitative phase-contrast imaging," *Optics Letters*, vol. 30, no. 16, pp. 2131-2133, Aug 2005.

[39] R. Shang, S. Chen, C. Li, and Y. Zhu, "Spectral modulation interferometry for quantitative phase imaging," (in English), *Biomedical Optics Express*, vol. 6, no. 2, pp. 473-479, Feb 2015.

[40] G. Tearney, R. Webb, and B. Bouma, "Spectrally encoded confocal microscopy," *Optics Letters*, vol. 23, no. 15, pp. 1152-1154, Aug 1998.

[41] M. Merman, A. Abramov, and D. Yelin, "Theoretical analysis of spectrally encoded endoscopy," *Optics Express*, vol. 17, no. 26, pp. 24045-24059, Dec 2009.

[42] D. Yelin, B. Bouma, J. Rosowsky, and G. Tearney, "Doppler imaging using spectrally-encoded endoscopy," *Optics Express*, vol. 16, no. 19, pp. 14836-14844, Sep 2008.

[43] W. McCrone, *Polarized light microscopy*. Ann Arbor: Ann Arbor Science Publishers, 1978.

[44] Y. Otani, T. Shimada, T. Yoshizawa, and N. Umeda, "Two-dimensional birefringence measurement using the phase shifting technique," *Optical Engineering*, vol. 33, no. 5, pp. 1604-1609, 1994.

[45] A. L. Bajor, "Automated polarimeter–macroscope for optical mapping of birefringence, azimuths, and transmission in large area wafers. Part I. Theory of the measurement," *Review of Scientific Instruments*, vol. 66, no. 4, pp. 2977-2990, 1995.

[46] Y. Zhu, T. Koyama, T. Takada, and Y. Murooka, "Two-dimensional measurement technique for birefringence vector distributions: measurement principle," *Applied Optics*, vol. 38, no. 11, pp. 2225-2231, Apr 1999.

[47] Y. Zhu, T. Takada, and Y. Murooka, "Two-dimensional optical measurement techniques based on optical birefringence effects," *Optical Engineering,* vol. 41, no. 12, pp. 3183-3192, 2002.

[48] M. Shribak and R. Oldenbourg, "Techniques for fast and sensitive measurements of two-dimensional birefringence distributions," *Applied Optics,* vol. 42, no. 16, pp. 3009-3017, Jun 2003.

[49] A. Changoor *et al.*, "A polarized light microscopy method for accurate and reliable grading of collagen organization in cartilage repair," *Osteoarthritis and Cartilage,* vol. 19, no. 1, pp. 126-135, Jan 2011.

[50] L. Cohen, R. Keynes, and B. Hille, "Light Scattering and Birefringence Changes during Nerve Activity," *Nature,* vol. 218, no. 5140, pp. 438-441, May 1968.

[51] Y. Abraham and R. Elbaum, "Quantification of microfibril angle in secondary cell walls at subcellular resolution by means of polarized light microscopy," *New Phytologist,* vol. 197, no. 3, pp. 1012-1019, 2013.

[52] R. Oldenbourg, E. Salmon, and P. Tran, "Birefringence of Single and Bundled Microtubules," *Biophysical Journal,* vol. 74, no. 1, pp. 645-654, Jan 1998.

[53] L. Liu, R. Oldenbourg, J. Trimarchi, and D. Keefe, "A reliable, noninvasive technique for spindle imaging and enucleation of mammalian oocytes," *Nat Biotech,* vol. 18, no. 2, pp. 223-225, Feb 2000.

[54] W. Wang, L. Meng, R. Hackett, and D. Keefe, "Developmental ability of human oocytes with or without birefringent spindles imaged by Polscope before insemination," *Human Reproduction,* vol. 16, no. 7, pp. 1464-1468, Jul 2001.

[55] A. Dharmadhikari, H. Basu, J. Dharmadhikari, S. Sharma, and D. Mathur, "On the birefringence of healthy and malaria-infected red blood cells," *Journal of Biomedical Optics,* vol. 18, no. 12, p. 125001, 2013.

[56] M. Axer *et al.*, "High-Resolution Fiber Tract Reconstruction in the Human Brain by Means of Three-Dimensional Polarized Light Imaging," *Frontiers in Neuroinformatics,* vol. 5, p. 34, Dec 2011.

[57] C. Vinegoni, T. Ralston, W. Tan, W. Luo, D. Marks, and S. Boppart, "Integrated structural and functional optical imaging combining spectral-domain optical coherence and multiphoton microscopy," *Applied Physics Letters*, vol. 88, no. 5, p. 3, Jan 2006, 053901.

[58] T. Le, I. Langohr, M. Locker, M. Sturek, and J. Cheng, "Label-free molecular imaging of atherosclerotic lesions using multimodal nonlinear optical microscopy," *Journal of Biomedical Optics*, vol. 12, no. 5, p. 10, 054007, Sep-Oct 2007.

[59] S. Jiao, Z. Xie, H. Zhang, and C. Puliafito, "Simultaneous multimodal imaging with integrated photoacoustic microscopy and optical coherence tomography," *Optics Letters*, vol. 34, no. 19, pp. 2961-2963, Oct 2009.

Chapter 2 Quantitative Polarized Light Microscopy using Spectral Multiplexing Interferometry

In this chapter, we propose an interferometric spectral multiplexing method for measuring birefringent specimens with simple configuration and high sensitivity. The retardation and orientation of sample birefringence are simultaneously encoded onto two spectral carrier waves, generated interferometrically by a birefringent crystal through polarization mixing. A single interference spectrum hence contains sufficient information for birefringence determination, eliminating the need for mechanical rotation or electrical modulation. The technique is analyzed theoretically and validated experimentally on cellulose film. System simplicity permits the possibility of mitigating system birefringence background. Further analysis demonstrates the technique's exquisite sensitivity as high as ~20pm for retardation measurement.

2.1. Introduction

Polarized light microscopy (PLM) is perhaps best known for its long-standing role in petrology and mineralogy, but has also been extensively used in material sciences and biology for characterization of optically anisotropic structures [1], which are often difficult to visualize with other label-free techniques such as phase contrast [2] and differential interference contrast [3] microscopy. PLM has received growing attention in recent years for their capability of quantifying the birefringent formation of fine biological structures such as collagen [4], cell membrane/wall [5, 6], mitotic/meiotic spindle [7-9], red blood cell [10], and brain fiber tracts [11].

For birefringence measurements, one needs to determine not only the pathlength retardation but also the azimuth angle of slow axis. Most PLM techniques require multiple acquisitions by manipulating polarizing elements mechanically [12-15] and/or electrically [16, 17] for demodulating both parameters. Therefore, system stability and reproducibility are essential in order to achieve high accuracy and sensitivity. Additionally, multiple measurements

limit system speed, hindering their application to studying fast dynamics. Recently, spectral-domain interferometry has been found useful to address this challenge by mixing light [18] using two birefringent crystals with different retardation orientated at 45°, permitting simultaneous demodulation of both birefringence parameters of the sample from a single channeled spectrum based on Mueller matrix analysis. The dual-crystal configuration, however, is inconvenient when probing large areas of the sample.

In this chapter, we propose a more compact system, using only one crystal retarder that provides interferometric spectral multiplexing for single-shot birefringence measurement. When oriented at an angle, the crystal causes polarization mixing and its large pathlength retardation generates two carrier waves within a single spectrum of single- and double-frequency, onto which sample birefringence is encoded. The simple geometry allows for a Jones calculus derivation of an analytical expression for the detected signal, thus facilitating the understanding of signal demodulation scheme. In addition, it provides a theoretical basis for fully analyzing the system's sensitivity of birefringence retardation and azimuth angle measurements, confirming its highly sensitive performance. Such theoretical sensitivity analysis, although important, has not been reported for quantitative PLM techniques.

2.2. System and Method

The system is based on a reflected light imaging configuration, as shown in Fig. 2.1(a). Broadband light of a single-mode superluminescent diode (Superlum; 837nm, FWHM 54nm) is collimated into free space from a 50/50 fiber coupler. It then passes through a linear polarizer and a birefringent crystal (LiNbO3, thickness 2.75mm), both oriented at fixed, predetermined angles. A fiber polarization controller maximizes the power transmitted through the polarizer. A compound objective consisting of two achromatic doublets focuses the light onto the birefringent specimen, which is placed on a reflective surface for double-pass transmission measurement. Return light is again modified by the crystal and filtered by the polarizer (now as analyzer) before detected by a custom spectrometer built with a high-speed linescan camera (e2v; EM1, 1024 pixels, line rate 78kHz). Two-dimensional images are acquired by a pair of galvo scanners.

Signal propagation through the system can be analyzed using Jones calculus, with the angle of each polarizing components defined as in Fig. 2.1(b). For convenience, the coordinate

system is chosen such that the x axis is aligned with the transmission direction of the polarizer. The slow axes of the birefringent crystal and the sample orient at angles α and β relative to the x axis, respectively.

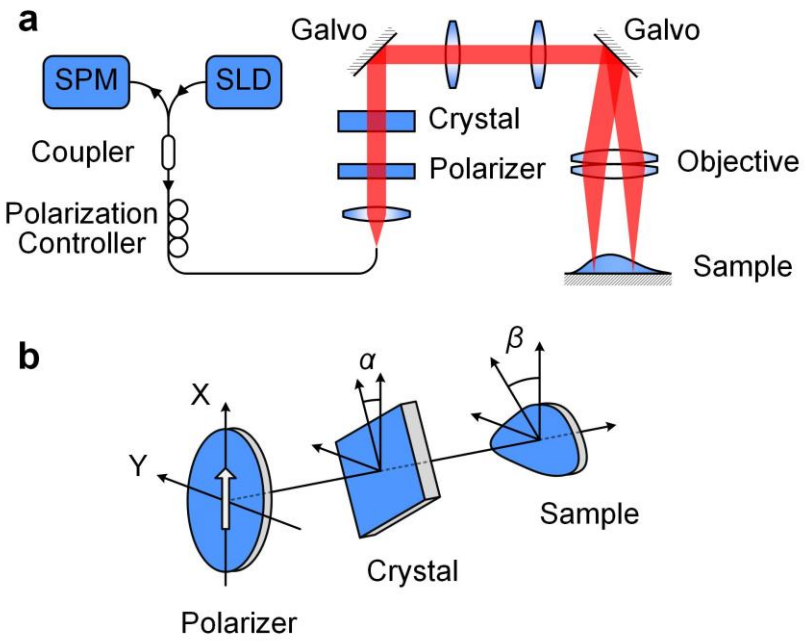

Figure 2.1 (a) System schematic. SLD, superluminescent diode. SPM, spectrometer. (b) Orientation of polarizing components.

Assuming the normalized Jones vector after the polarizer is $\begin{bmatrix}\mathbf{1} & \mathbf{0}\end{bmatrix}^{\mathrm{T}}$, one can then obtain the field after a double-pass transmission through the system. Upon returning, only the x polarization will remain at the output, which can be written as:

$$\mathbf{E}_{out} = \begin{bmatrix}\mathbf{1} & \mathbf{0}\end{bmatrix}\mathbf{R}(-\alpha)\mathbf{T}_{\mathrm{c}}\mathbf{R}(\alpha-\beta)\mathbf{T}_{\mathrm{s}}\mathbf{R}(\beta-\alpha)\mathbf{T}_{\mathrm{c}}\mathbf{R}(\alpha)\begin{bmatrix}\mathbf{1}\\ \mathbf{0}\end{bmatrix}. \tag{2.1}$$

where $\mathbf{R}(\varphi)$ is the rotation matrix,

$$\mathbf{R}(\varphi) = \begin{bmatrix}\cos\varphi & \sin\varphi\\ -\sin\varphi & \cos\varphi\end{bmatrix}, \tag{2.2}$$

and $\mathbf{T}_c$ and $\mathbf{T}_s$ are the wavenumber-dependent transmission matrices of the crystal and the sample, respectively, as in the following,

$$\mathbf{T}_c(k)=\begin{bmatrix} e^{jkL} & \mathbf{0} \\ \mathbf{0} & \mathbf{1} \end{bmatrix} \text{ and } \mathbf{T}_s=\begin{bmatrix} e^{j2kd(x,y)} & \mathbf{0} \\ \mathbf{0} & \mathbf{1} \end{bmatrix}, \tag{2.3}$$

where k is the wavenumber, L is the pathlength retardation between slow and fast axes of the crystal, and $d(x,y)$ is the retardation of the sample at (x,y). For simplicity, we use only d hereinafter. It should be noted that $\mathbf{T}_c$ accounts for the single-pass retardation and $\mathbf{T}_s$ combines both passes. Substituting Eqs. (2.2) and (2.3) into Eq. (2.1), $\mathbf{E}_{out}$ can be determined. Since $\mathbf{E}_{out}$ is based on a normalized input vector, we add the spectrum envelope $I_0(k)$ back to obtain the output spectral intensity:

$$I(k,x,y)=I_0(k)\left|\mathbf{E}_{out}\right|^2=I_{DC}(k)+\left[I_{1f}(k)+c.c.\right]+\left[I_{2f}(k)+c.c.\right], \tag{2.4}$$

where *c.c.* denotes the complex conjugate of corresponding terms and

$$I_{DC}(k)=I_0(k)\left[\mathbf{1}-\frac{\mathbf{1}}{\mathbf{2}}\sin^2 2\alpha-\left(\mathbf{1}-\frac{\mathbf{3}}{\mathbf{2}}\sin^2 2\alpha\right)\sin^2 2(\beta-\alpha)\sin^2 kd\right].$$

$$I_{1f}(k)=\frac{\mathbf{1}}{\mathbf{4}}\sin 4\alpha I_0(k)\left[j\sin 2(\beta-\alpha)\sin 2kd-\frac{\mathbf{1}}{\mathbf{2}}\sin 4(\beta-\alpha)\sin 2kd\tan kd\right]e^{jkL}. \tag{2.5}$$

$$I_{2f}(k)=\frac{\mathbf{1}}{\mathbf{4}}\sin^2 2\alpha I_0(k)\left[j\cos 2(\beta-\alpha)\sin 2kd+\cos 2kd+\sin^2 2(\beta-\alpha)\sin^2 kd\right]e^{j2kL}.$$

Eq. (2.5) clearly indicates that the system generates two separate interference terms in the detected spectrum, $I_{1f}(k)$ and $I_{2f}(k)$, with e^{jkL} and e^{j2kL} being the respective carrier waves, corresponding to single- and double-pass crystal retardation. With a relatively large carrier frequency L (typically hundreds of microns), these two terms appear as well separated peaks in Fourier domain, and their complex amplitudes contain sufficient information about sample birefringence. Specifically, their imaginary parts contain $\sin 2(\beta-\alpha)\sin 2kd$ and $\cos 2(\beta-\alpha)\sin 2kd$, from which d and β can be extracted.

The signal demodulation hence involves bandpass filtering, frequency downshifting and intensity normalization of the two peaks. These steps require the knowledge of angle α, spectrum intensity $I_0(k)$ and carrier waves e^{jkL} and e^{j2kL}, all of which are determined as described below. First, we note that if

$$\mathbf{1}-\frac{\mathbf{3}}{\mathbf{2}}\sin^2 \mathbf{2}\alpha = \mathbf{0} \text{ so that } \alpha = \mathbf{27.37}^\circ \triangleq \alpha_0, \tag{2.6}$$

$I_{DC}(k)$ simply becomes $\frac{\mathbf{2}}{\mathbf{3}} I_0(k)$ and sample independent. Therefore, in our experiment setup the crystal's slow axis is oriented at α_0 from the polarizer transmission axis and $I_0(k)$ is determined from each spectrum's DC component. It should be noted that for small sample birefringence d at nanometer level, $\sin^2 kd$ is negligible and $I_{DC}(k)$ may be regarded as sample independent and used for intensity normalization without restricting the value of α.

The carrier waves are obtained from system spectra without birefringence sample, i.e. $d = \mathbf{0}$. Under this condition Eq. (2.5) gives $I_{1f}(k) = \mathbf{0}$ and $I_{2f}(k) = \frac{\mathbf{1}}{\mathbf{6}} I_0(k) e^{j2kL}$, from which the phase term $\varphi(k) = \mathbf{2}kL$ is extracted to reconstruct the single- and double-frequency carrier waves as $e^{-j\varphi(k)/2}$ and $e^{-j\varphi(k)}$. Such spectra can be obtained from birefringence-free areas of the image or from a separate measurement without sample.

With the carrier waves, $I_{1f}(k)$ and $I_{2f}(k)$ in Eq. (2.5) can be downshifted to baseband to obtain their complex amplitudes. Following the extraction of their imaginary parts and proper normalization, one can then obtain two intermediate parameters,

$$\begin{aligned} A(k) &= \frac{\mathrm{Im}\left[I_{1f}(k) \cdot e^{-j\varphi(k)/2} \right]}{\sin \mathbf{4}\alpha_0 \cdot I_0(k)/\mathbf{4}} = \sin \mathbf{2}(\beta - \alpha_0) \sin \mathbf{2}kd, \\ B(k) &= \frac{\mathrm{Im}\left[I_{2f}(k) \cdot e^{-j\varphi(k)} \right]}{\sin^2 \mathbf{2}\alpha_0 \cdot I_0(k)/\mathbf{4}} = \cos \mathbf{2}(\beta - \alpha_0) \sin \mathbf{2}kd, \end{aligned} \tag{2.7}$$

and sample birefringence can be determined as

$$d = \text{avg}\left[\arcsin\sqrt{A(k)^2 + B(k)^2}\,/\,2k\right],$$
$$\beta = \text{avg}\left[\frac{1}{2}\arctan\frac{A(k)}{B(k)} + \alpha_0\right], \tag{2.8}$$

where avg(·) denotes averaging over the range of k.

Therefore a single spectrum is sufficient to determine both d and β, eliminating the need for mechanical rotation or electrical modulation. Furthermore, average of retardation and axis azimuth over the whole wavelength range provides more accurate results. Due to arcsin(·)'s restricted domain, d is limited to below one-eighth of the shortest wavelength of the system, or about 100.8nm, which is still sufficiently large for most biological birefringence at cellular level, such as meiotic spindles.

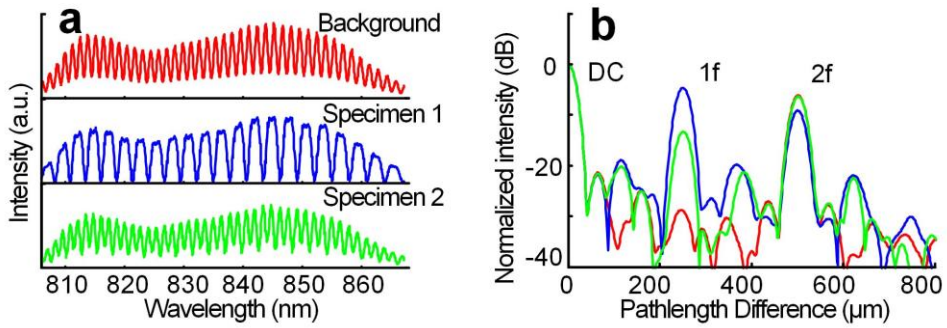

Figure 2.2. (a) Interference spectrum obtained on background (red) and on two different cellulose film specimens (blue and green). (b) Corresponding Fourier spectra.

2.3. Birefringence Imaging of Cellulose Film

We validated this single-crystal, spectral-multiplexing approach using a regenerated cellulose dialysis tubing film as sample (Fisher Scientific; thickness 24.6 μm, measured by Mitutoyo digital linear gage). Using crossed polarizers, the film's slow and fast axes were approximately marked, along which two rectangular specimens were cut. They were then placed on a silver mirror, covered by a microscope slide, and immersed in index liquid (n=1.444). The liquid can sufficiently reduce the surface reflection to legible level. An area of 2mm×2mm was imaged with 500×500 pixel resolution using raster scan.

Figure 2.2 shows representative intensity spectra of the background and the two specimens as well as their Fourier transform, where the 1f and 2f peaks are clearly seen and vary in phase and magnitude. Bandpass filtering can isolate either peak or the DC component. When needed, a window function can be used to minimize or eliminate spectral leakage. In Fig. 2.2, the spectra were first normalized with the source intensity envelope and then a Blackman-Harris window is applied, providing excellent peak separation.

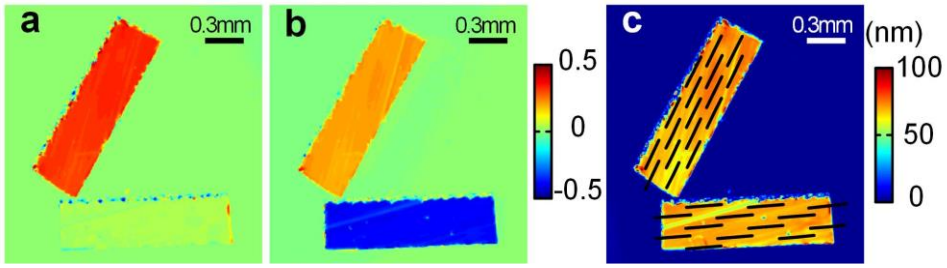

Figure 2.3. (a)(b) Distribution of measured parameter *A* and *B* after average over the whole wavelength range. (c) Distribution of birefringence retardation and slow axis orientation.

Figures 2.3(a) and 2.3(b) show the distribution of intermediate parameters *A* and *B* in Eq. (2.7), respectively, after averaging over the detected spectral range. Figure 2.3(c) reveals sample birefringence distribution. The short, black lines indicate slow axis orientation, which is consistent with the fact that the specimens were cut along its axes. As expected, although *A* and *B* are dramatically different, the retardations of the two specimens are similar because they are from the same dialysis tubing film. The averaged values for the upper and lower pieces are 70.50nm and 69.84nm, respectively.

2.4. System Birefringence Background Calibration and Sensitivity Analysis

2.4.1. Birefringence background

In polarized light microscopy, internal strains in system optics often produce a birefringence background, affecting sample measurement accuracy. When strain-free optics is used, these background can be minimized and the residue system birefringence may be removed by a subtraction process [16]. Due to their high cost, however, most systems are not built with these special parts. For such systems, we show that the single crystal configuration may provide substantial mitigation of birefringence background. The idea is to align the axes of the crystal to

those of system birefringence such that the latter can be incorporated as part of carrier retardation, hence minimizing the residue. Its efficacy is shown in Fig. 2.4, where the polarizer and the crystal are rotated together (their angle still fixed at α_0) to different angles and the sample-free birefringence background is measured.

As the parts rotate, the effective system birefringence varies substantially, with a minimum at 110°, where average background birefringence is 0.75nm, as compared to up to 2.88nm at other angles. If only the 300×300 pixel (1.2mm×1.2mm) area in the upper right is considered, this ratio becomes 0.39nm to 2.66nm. This result verifies the advantage of our single crystal approach in background birefringence mitigation. The film measurements were performed at this particular angle.

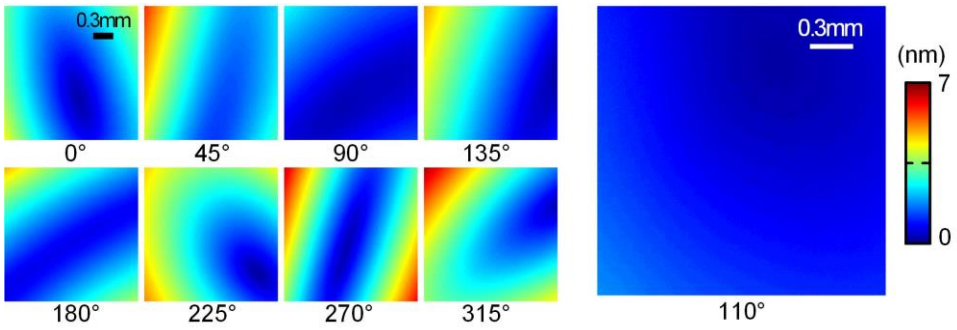

Figure 2.4. Background birefringence distribution at different polarizer orientation.

2.4.2. Theoretical analysis and experimental validation on measurement sensitivity

We also investigate system measurement sensitivity, which is a crucial performance parameter depending on noise level. In general, birefringence measurement systems have sufficient signal power and are primarily limited by shot noise. In our system, it is reflected as the spectrum intensity fluctuation on the linescan camera, which follows Poisson distribution but can be closely approximated as Gaussian noise because of the high signal power. For sensitivity analysis, we consider the two signal peaks in Fourier domain with corresponding noises, i.e. $I_{1f}+n_{1f}$ and $I_{2f}+n_{2f}$. Since n_{1f} and n_{2f} are the Fourier components of the Gaussian-approximated shot-noise spectrum, they are Gaussian random variables as well. They will also be factored into A and B through Eq. (2.7) and subsequently into d and β through Eq. (2.8).

Therefore, Gaussian noises are introduced into demodulated results. The measurement sensitivity, defined as the standard deviation of d and β, can then be approximated as

$$\sigma_d \approx \frac{4}{3k_0 \cos 2k_0 d}\sqrt{\left(\frac{\sin 2(\beta-\alpha_0)}{\sin 4\alpha_0}\right)^2+\left(\frac{\cos 2(\beta-\alpha_0)}{\sin^2 2\alpha_0}\right)^2}\cdot\sigma,$$
$$\sigma_\beta \approx \frac{4}{3\sin 2k_0 d}\sqrt{\left(\frac{\cos 2(\beta-\alpha_0)}{\sin 4\alpha_0}\right)^2+\left(\frac{\sin 2(\beta-\alpha_0)}{\sin^2 2\alpha_0}\right)^2}\cdot\sigma, \quad \textbf{(2.9)}$$

where k_0 is the center wavenumber and σ is the normalized noise standard deviation, which is the same for both n_{1f} and n_{2f}. Following a discrete Fourier transform of shot noise spectrum, it can be seen that,

$$\sigma = \frac{\sigma[\mathrm{Im}(n_{1f,2f})]}{\sum_{n=1}^{N} I_n} = \frac{1}{\sqrt{2N_e}} \text{ with } N_e = g\sum_{n=1}^{N} I_n, \quad \textbf{(2.10)}$$

where g is electronic gain of the linescan camera; I_n is the spectral intensity reading of the *n*-th pixel; N_e is thus the total number of photogenerated electrons or total detected power.

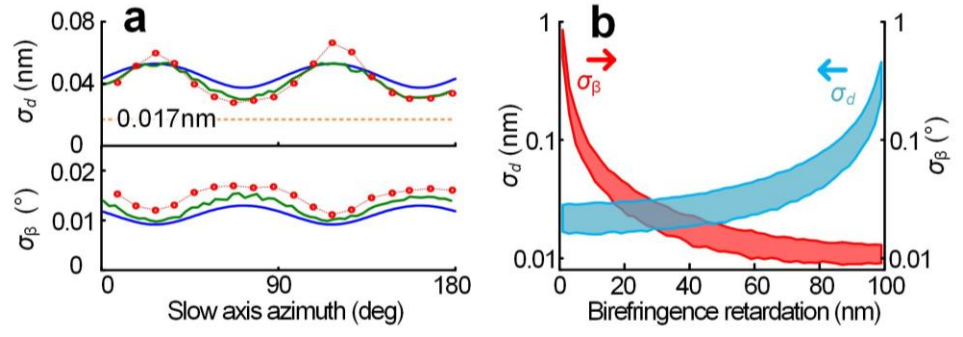

Figure 2.5. (a) Theoretical (blue), simulated (green) and experimental (red) sensitivity of birefringence retardation and axis azimuth for d=70nm. Experimental sensitivity of background birefringence retardation (dashed line) is 0.017nm. (b) Simulated sensitivity range of birefringence retardation and azimuth angle.

As expected, Eqs. (2.9) and (2.10) indicate that sensitivities are inversely proportional to the square root of detected optical power [19]. To verify these analytical results, they are

compared with simulation for d=70nm, showing excellent agreement in Fig. 2.5(a). The slight discrepancy results from various approximations made in the derivation, especially treating n_{1f} and n_{2f} as independent random variables when they are weakly correlated. From these plots, it is clear that the specific choice of α_0 leads to the periodic dependence of σ_d and σ_β on β, oscillating between maximum and minimum values. This range of possible sensitivities is plotted in Fig. 2.5(b) for each d. For ~90% of the measurement range, retardation sensitivity better than 0.1nm and angular sensitivity better than 0.1° could potentially be achieved. Further, for small d (<10nm), often seen in cellular structures, the retardation sensitivity could in theory reach ~20pm with sub-degree angular sensitivity.

To further substantiate our analysis, we measure the sensitivity for a single spot on the specimen (d≈70nm), and repeat the procedure by rotating its slow axis at 10° steps. Figure 2.5(a) shows that the measurement is in good agreement with both theoretical and simulated curves.

We also measure the sensitivity for sample-free background to be 17pm, which corresponds to the case where sample retardation is diminishingly small. This result is also consistent with theoretical prediction and represents the highest possible performance for the current system. Further improvement can be achieved by increasing detected signal power, as clearly suggested in Eq. (2.10).

2.5. Conclusion

In summary, we have demonstrated a simple system with a single birefringent crystal retarder combined with interferometric spectral multiplexing for single-shot birefringence measurement. For monitoring a single point, the speed is only limited by that of the spectrometer. For 1D and 2D measurement, the reflected light geometry is compatible with galvo scanning, opening up the possibilities for observing fast birefringent dynamics. In addition, the single crystal implementation makes it possible to significantly reduce birefringence background inherent in the system, potentially relaxing the requirement for costly strain-free optics when high measurement accuracy is needed. Finally, the simplicity of the system leads to a complete analytical description of its signals, which also offers a means of theoretically analyzing the system's sensitivity, a parameter fundamental to understanding system performance and

interpreting measured data. The analysis reveals the exquisite sensitivity of the proposed system and points direction for future improvement.

References

[1] S. Inoué, "Polarization Microscopy," in *Current Protocols in Cell Biology*: John Wiley & Sons, Inc., 2001.

[2] F. Zernike, "Phase contrast, a new method for the microscopic observation of transparent objects," *Physica,* vol. 9, no. 7, pp. 686-698, Jul 1942.

[3] G. Nomarski, "Differential microinterferometer with polarized waves," *J. Phys. Radium,* vol. 16, no. 9, pp. 9S-11S, 1955.

[4] A. Changoor *et al.*, "A polarized light microscopy method for accurate and reliable grading of collagen organization in cartilage repair," *Osteoarthritis and Cartilage,* vol. 19, no. 1, pp. 126-135, Jan 2011.

[5] L. Cohen, R. Keynes, and B. Hille, "Light Scattering and Birefringence Changes during Nerve Activity," *Nature,* 10.1038/218438a0 vol. 218, no. 5140, pp. 438-441, May 1968.

[6] Y. Abraham and R. Elbaum, "Quantification of microfibril angle in secondary cell walls at subcellular resolution by means of polarized light microscopy," *New Phytologist,* vol. 197, no. 3, pp. 1012-1019, 2013.

[7] W. Wang, L. Meng, R. Hackett, and D. Keefe, "Developmental ability of human oocytes with or without birefringent spindles imaged by Polscope before insemination," *Human Reproduction,* vol. 16, no. 7, pp. 1464-1468, Jul 2001.

[8] R. Oldenbourg, E. Salmon, and P. Tran, "Birefringence of Single and Bundled Microtubules," *Biophysical Journal,* vol. 74, no. 1, pp. 645-654, Jan 1998.

[9] L. Liu, R. Oldenbourg, J. Trimarchi, and D. Keefe, "A reliable, noninvasive technique for spindle imaging and enucleation of mammalian oocytes," *Nat Biotech,* vol. 18, no. 2, pp. 223-225, Feb 2000.

[10] A. Dharmadhikari, H. Basu, J. Dharmadhikari, S. Sharma, and D. Mathur, "On the birefringence of healthy and malaria-infected red blood cells," *Journal of Biomedical Optics,* vol. 18, no. 12, p. 125001, 2013.

[11] M. Axer *et al.*, "High-Resolution Fiber Tract Reconstruction in the Human Brain by Means of Three-Dimensional Polarized Light Imaging," *Frontiers in Neuroinformatics,* vol. 5, p. 34, Dec 2011.

[12] Y. Otani, T. Shimada, T. Yoshizawa, and N. Umeda, "Two-dimensional birefringence measurement using the phase shifting technique," *Optical Engineering,* vol. 33, no. 5, pp. 1604-1609, 1994.

[13] A. L. Bajor, "Automated polarimeter–macroscope for optical mapping of birefringence, azimuths, and transmission in large area wafers. Part I. Theory of the measurement," *Review of Scientific Instruments,* vol. 66, no. 4, pp. 2977-2990, 1995.

[14] Y. Zhu, T. Koyama, T. Takada, and Y. Murooka, "Two-dimensional measurement technique for birefringence vector distributions: measurement principle," *Applied Optics,* vol. 38, no. 11, pp. 2225-2231, Apr 1999.

[15] J. Park, H. Yu, J.-H. Park, and Y. Park, "LCD panel characterization by measuring full Jones matrix of individual pixels using polarization-sensitive digital holographic microscopy," *Optics Express,* vol. 22, no. 20, pp. 24304-24311, Oct 2014.

[16] M. Shribak and R. Oldenbourg, "Techniques for fast and sensitive measurements of two-dimensional birefringence distributions," *Applied Optics,* vol. 42, no. 16, pp. 3009-3017, Jun 2003.

[17] Y. Zhu, T. Takada, and Y. Murooka, "Two-dimensional optical measurement techniques based on optical birefringence effects," *Optical Engineering,* vol. 41, no. 12, pp. 3183-3192, 2002.

[18] T. Wakayama, Y. Otani, and N. Umeda, "One-shot birefringence dispersion measurement based on channeled spectrum technique," *Optics Communications,* vol. 281, no. 14, pp. 3668-3672, Jul 2008.

[19] M. Choma, A. Ellerbee, C. Yang, T. Creazzo, and J. Izatt, "Spectral-domain phase microscopy," *Optics Letters,* vol. 30, no. 10, pp. 1162-1164, May 2005.

Chapter 3 Integrated Quantitative Phase and Birefringence Microscopy

In this chapter, a multimodal birefringence/phase imaging system is presented. The system features a crystal retarder that provides polarization mixing and generates two interferometric carrier waves in a single signal spectrum. The retardation and orientation of sample birefringence can then be measured simultaneously based on spectral multiplexing interferometry (SXI). Further, with the addition of a Nomarski prism, the same setup can be used for quantitative differential interference contrast (DIC) imaging. Sample phase can then be obtained with 2D integration. In addition, birefringence-induced phase error can be corrected using the birefringence data. This dual-modality approach is analyzed theoretically with Jones calculus and validated experimentally with malaria-infected red blood cells. The system generates not only corrected DIC and phase images, but birefringence map that highlights the distribution of hemozoin crystals.

Attribution

For the work described in this chapter, red blood cell samples were prepared by Dr. Michael Klemba from Department of Biochemistry.

3.1. Introduction

Label-free imaging of biological specimens typically employs optical phase as the primary contrast mechanism, as seen in techniques such as phase contrast microscopy [1] and differential interference contrast microscopy [2], and quantitative phase imaging (QPI) has received growing attention in recent years [3]. In many samples, however, birefringence can offer crucial contrast when revealing fine biological substructures such as collagen [4], cell membrane [5, 6], mitotic spindle [7], and hemozoin crystal [8]. Different from phase imaging, in birefringence measurements, one needs to determine two parameters, its retardation as well as the orientation of its axes. Previous attempts on experimental determination of both birefringence

parameters often require multiple acquisitions by adjusting polarizing optics, such as waveplates and liquid crystal phase modulators, either mechanically [9-12] or electrically [13, 14].

Functionally, the combination of quantitative phase and birefringence imaging will enhance contrast and may provide additional sample information by comparing registered images of different nature. Such integration, however, is traditionally difficult since the two approaches employ fundamentally different principles and optical setups. A recent advance in quadriwave lateral shearing interferometry has demonstrated such a combination, where birefringence is computed by curve-fitting a series of phase images obtained with a rotating polarizer [15].

3.2. System Setup

Here we propose a high-sensitivity spectral interferometry approach. Previously, we have demonstrated a single-shot, quantitative birefringence imaging technique [16] and a quantitative DIC technique for non-birefringent samples [17]. Implemented with spectral-domain low coherence interferometry for high sensitivity, they were based on similar hardware but unrelated signal analysis and processing. In this Letter, we provide a unifying theory to integrate these modalities into a single system for quantitative birefringence, DIC and phase imaging. Additionally, such theory allows to address the issues of system birefringence background and birefringence-induced DIC/phase distortion, thus achieving improved accuracy.

The system setup is based on a common-path, reflective interferometer, as shown in Fig. 3.1(a). It utilizes a broadband superluminescent diode (Superlum; 837 nm, FWHM 54 nm) as light source. A linear polarizer and a birefringent crystal ($LiNbO_3$, thickness 2.75 mm) are oriented at a pre-determined angle to introduce polarization mixing. For quantitative DIC imaging, a Nomarski prism is inserted at the back of the microscope objective (Nikon; 40×, 0.75 NA), splitting o- and e- waves by a small angle that leads to a lateral shear on the sample. Return light will pass through the system again, modified by the crystal and filtered by the polarizer before being collected by the single-mode fiber. The spectral interference carrying intensity and phase information is then detected by a custom spectrometer. Two galvanometers, separated by a 4-*f* system, provide two-dimensional point scanning of the specimen. For quantitative birefringence imaging, the Nomarski prism is simply removed to eliminate the shear.

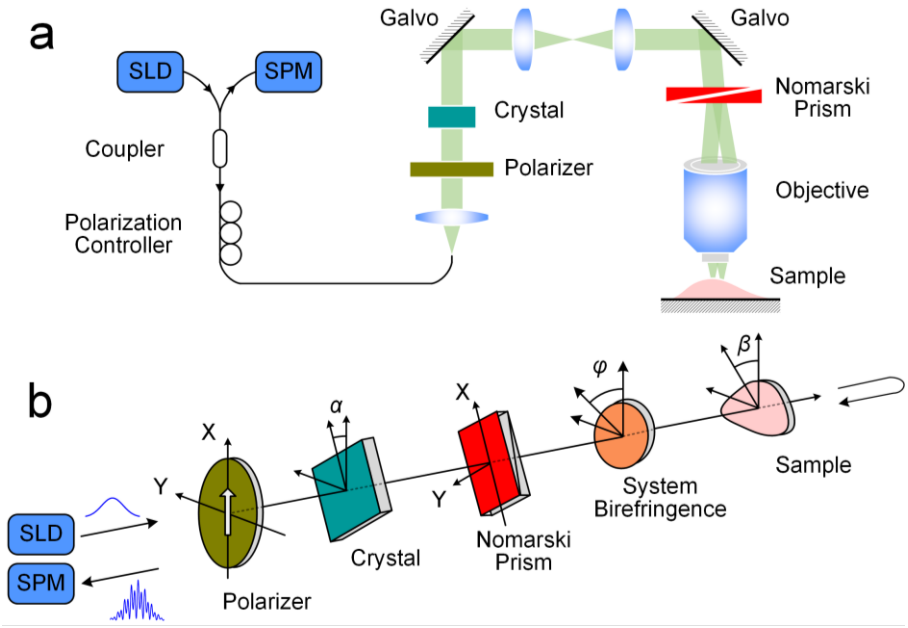

Figure 3.1. (a) Schematic of the integrated quantitative phase and birefringence imaging system. SLD, superluminescent diode. SPM, spectrometer. (b) Orientation of polarization components of the imaging system.

3.3. Single Shot Birefringence Imaging

Signal propagation through the system can be analyzed with Jones calculus using Fig. 3.1(b). For convenience, the transmission direction of the polarizer is chosen to be the *x* axis. The slow axes of the birefringent crystal and the sample orient at angles α and β relative to the *x* axis, respectively. For non-birefringent samples, β can be any angle since they are optically isotropic and in fact, it will be eliminated from the formula. System birefringence, arising from the residual birefringence of various system optics, can be treated as a lumped element with its slow axis oriented at angle φ [14].

We first analyze birefringence imaging, i.e. without the Nomarski prism in Fig. 3.1(b). Assuming the normalized Jones vector after the polarizer is $\begin{bmatrix}\mathbf{1} & \mathbf{0}\end{bmatrix}^{\mathrm{T}}$, the field after a double-pass transmission through the entire system can be obtained by

$$\mathbf{E}_O = \begin{bmatrix}\mathbf{1} & \mathbf{0}\end{bmatrix}\mathbf{R}(-\alpha)\mathbf{T}(\theta_C)\mathbf{R}(\alpha-\varphi)\mathbf{T}(\theta_B)\mathbf{R}(\varphi-\beta)$$
$$\mathbf{T}(2\theta_S)\mathbf{R}(\beta-\varphi)\mathbf{T}(\theta_B)\mathbf{R}(\varphi-\alpha)\mathbf{T}(\theta_C)\mathbf{R}(\alpha)\begin{bmatrix}\mathbf{1}\\ \mathbf{0}\end{bmatrix}, \quad \textbf{(3.1)}$$

where $\mathbf{R}$ is the rotation matrix and $\mathbf{T}$ is the transmission matrix for polarizing components, as in

$$\mathbf{R}(\varphi) = \begin{bmatrix}\cos\varphi & \sin\varphi\\ -\sin\varphi & \cos\varphi\end{bmatrix} \text{ and } \mathbf{T}(\theta) = \begin{bmatrix}\mathbf{1} & \mathbf{0}\\ \mathbf{0} & e^{j\theta}\end{bmatrix}. \quad \textbf{(3.2)}$$

Additionally, $\theta_C(k) = kL_C$, $\theta_B(k) = kL_B(x,y)$, and $\theta_S(k) = kL_S(x,y)$, where k is the wavenumber, L_C is the optical pathlength (OPL) retardation of the crystal retarder, and $L_B(x,y)$ and $L_S(x,y)$ stand for the retardation of system birefringence and sample birefringence at (x,y), respectively.

Since both L_B and L_S in live cell imaging are typically small compared to wavelength, small angle approximation is valid for θ_B and θ_S [12]. With Eqs. (3.1) and (3.2), the detected interference spectrum can be shown as

$$I = I_{\mathbf{0}}(k)\left|\mathbf{E}_O\right|^2 = I_{DC}(k) + \left[I_{\mathbf{1}f}(k) + c.c.\right] + \left[I_{\mathbf{2}f}(k) + c.c.\right], \quad \textbf{(3.3)}$$

where $I_{\mathbf{0}}(k)$ is the spectrum envelope,

$$I_{DC}(k) = I_{\mathbf{0}}(k)\left[\cos^{\mathbf{4}}\alpha + \sin^{\mathbf{4}}\alpha\right],$$
$$I_{\mathbf{1}f}(k) = \frac{\mathbf{1}}{\mathbf{4}}\sin\mathbf{4}\alpha I_{\mathbf{0}}(k)\left[jA_S(k) + jA_B(k)\right]e^{jkL_C}, \quad \textbf{(3.4)}$$
$$I_{\mathbf{2}f}(k) = \frac{\mathbf{1}}{\mathbf{4}}\sin^{\mathbf{2}}\mathbf{2}\alpha I_{\mathbf{0}}(k)\left[jB_S(k) + jB_B(k) + \mathbf{1}\right]e^{j\mathbf{2}kL_C},$$

and *c.c.* denotes the complex conjugate of corresponding terms. Equation (3.4) clearly indicates that $I_{\mathbf{1}f}$ and $I_{\mathbf{2}f}$ are two interference terms in the detected spectrum with carriers of e^{jkL_C} and $e^{j\mathbf{2}kL_C}$, generated by the large OPL retardation of the crystal retarder. In addition, sample and

system birefringence parameters are simultaneously modulated onto the complex amplitude of the carrier waves, but are found to be decoupled from each other, as seen in the following intermediate parameters:

$$\begin{cases} A_S(k) = \mathbf{2}\theta_S(k)\sin\mathbf{2}(\alpha-\beta) \\ B_S(k) = \mathbf{2}\theta_S(k)\cos\mathbf{2}(\alpha-\beta) \end{cases}, \begin{cases} A_B(k) = \mathbf{2}\theta_B(k)\sin\mathbf{2}(\alpha-\varphi) \\ B_B(k) = \mathbf{2}\theta_B(k)\cos\mathbf{2}(\alpha-\varphi) \end{cases}. \quad \textbf{(3.5)}$$

Based on above derivation, we can perform a system birefringence calibration without sample to acquire A_B and B_B, and remove them from sample measurement to obtain A_S and B_S only for the determination of sample birefringence parameters.

As for the choice of α, a wide range of angles may be used except when $\sin\mathbf{4}\alpha = \mathbf{0}$ or $\sin^2\mathbf{2}\alpha = \mathbf{0}$ in Eq. (3.4). We set α at 31.7° so that $\sin\mathbf{4}\alpha = \sin^2\mathbf{2}\alpha$, which leads to identical coefficients for both interference terms in Eq. (3.4). Thus the sensitivity of both sample birefringence retardation and azimuth angle will be independent of sample birefringence orientation. A detailed sensitivity analysis can be found in [16].

With the knowledge of α, $I_{\mathbf{0}}(k)$ can also be determined from I_{DC}. The signal demodulation hence involves bandpass filtering of $I_{\mathbf{1}f}$ and $I_{\mathbf{2}f}$, normalizing them using α and $I_{\mathbf{0}}$, and frequency downshifting. With the carrier waves obtained from the interference spectra without sample, $I_{\mathbf{1}f}$ and $I_{\mathbf{2}f}$ can be downshifted to baseband for extracting A_S and B_S from the imaginary part of the complex amplitude after removing A_B and B_B. Sample birefringence is therefore

$$\begin{aligned} L_S &= \mathrm{avg}\left[\sqrt{A_S(k)^2 + B_S(k)^2}\Big/\mathbf{2}k\right], \\ \beta &= \mathrm{avg}[-\frac{\mathbf{1}}{\mathbf{2}}\arctan\frac{A_S(k)}{B_S(k)} + \alpha], \end{aligned} \quad \textbf{(3.6)}$$

where avg(·) denotes averaging over the range of *k*. This process allows the background-free measurement of L_S and β from one single spectrum.

To demonstrate the birefringence imaging capability, we chose *Plasmodium falciparum*-infected human RBCs. During their asexual replication cycle within RBCs, malaria parasites consume host cell hemoglobin and produce birefringent hemozoin crystals. For imaging, an *in vitro* culture of *P. falciparum*-infected erythrocytes was fixed with 0.1% glutaraldehyde in phosphate buffered saline (PBS). Fixed parasites were then washed with PBS to remove glutaraldehyde prior to imaging.

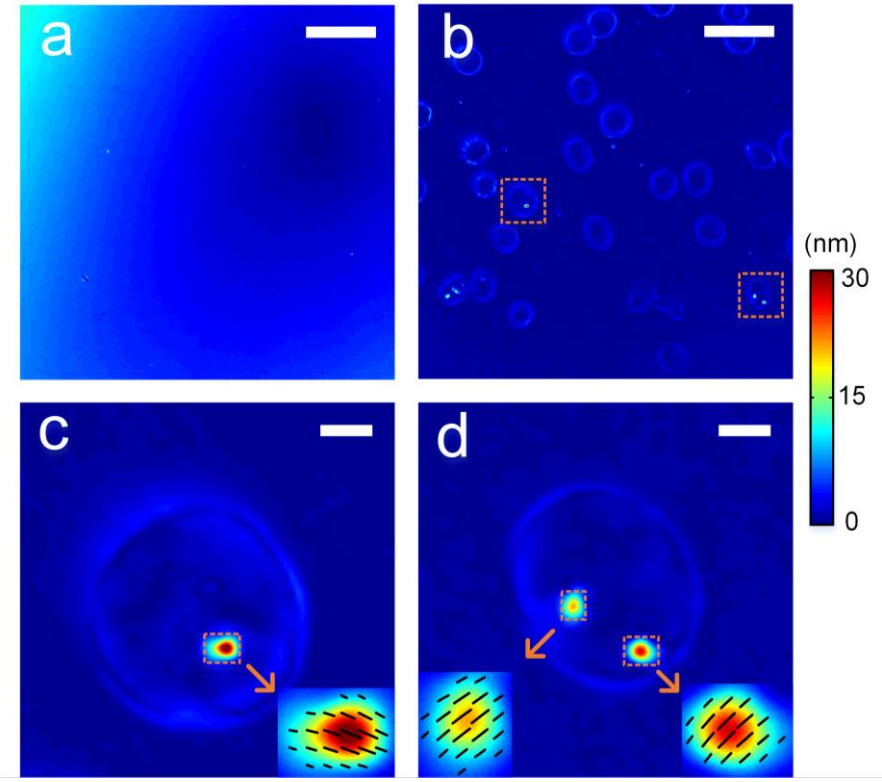

Figure 3.2. (a) System birefringence background. Scale bar 20μm. (b) Birefringence retardation image of *P. falciparum*-infected human RBCs. Scale bar 20μm. (c)(d) Birefringence retardation images of single infected RBCs from (b). Scale bar 2μm. Inset: The line direction and length indicate the local optical axes orientation and birefringence retardation of the hemozoin crystals.

To quantify RBC birefringence, we first calibrate system birefringence background. Its magnitude map is shown in Fig. 3.2(a), with an averaged retardation of 4.12 nm over the field of view. Figure 3.2(b) shows the birefringence retardation image of the RBCs after background subtraction based on Eqs. (3.4) and (3.5). Among the imaged cells, the infected ones can be clearly identified by the hemozoin crystals inside. The magnitude of hemozoin birefringence

retardation in the infected RBCs is about 30 nm and is much stronger than the birefringence of cell body, which is believed to be originated largely from local heterogeneity. Enlarged images of two infected RBCs are also depicted in Figs. 3.2(c) and 3.2(d) with slow axis orientation illustrated. One and two crystals are revealed respectively with the birefringence slow axis distributed uniformly for each crystal. The presence of two crystals likely indicates that this red cell has been invaded by two parasites.

3.4. Integrated Quantitative Phase Imaging with Nomarski Prism

In addition to single-shot birefringence imaging, the same setup can also be used for quantitative DIC imaging. Note that as shown in Fig. 3.1(b), the direction of the inserted Nomarski prism should be parallel to the axes of crystal retarder. With the Nomarski prism splitting the incident beam into two by a small angle, the o- and e- waves will experience different polarization mixing in the specimen. The Jones analysis now becomes

$$\begin{aligned}\mathbf{E}_O = &\begin{bmatrix}\mathbf{1} & \mathbf{0}\end{bmatrix}\mathbf{R}(-\alpha)\mathbf{T}(\theta_C)\mathbf{R}(\alpha-\varphi)\mathbf{T}(\theta_B)\mathbf{R}(\varphi-\alpha)\cdot \\ &\left[\mathbf{R}(\alpha-\beta)\mathbf{T}_{S1}\mathbf{R}(\beta-\alpha)\begin{pmatrix}\mathbf{1} & \mathbf{0}\\ \mathbf{0} & \mathbf{0}\end{pmatrix}+\mathbf{R}(\alpha-\beta)\mathbf{T}_{S2}\mathbf{R}(\beta-\alpha)\begin{pmatrix}\mathbf{0} & \mathbf{0}\\ \mathbf{0} & \mathbf{1}\end{pmatrix}\right] \\ &\cdot\mathbf{R}(\alpha-\varphi)\mathbf{T}(\theta_B)\mathbf{R}(\varphi-\alpha)\mathbf{T}(\theta_C)\mathbf{R}(\alpha)\begin{bmatrix}\mathbf{1}\\ \mathbf{0}\end{bmatrix},\end{aligned} \tag{3.7}$$

where $\mathbf{T}_{S1}$ and $\mathbf{T}_{S2}$ denote the respective transmission matrices for sample retardation for the two waves at their corresponding positions,

$$\mathbf{T}_{S1}=\begin{pmatrix}e^{j2kL_{1e}} & \mathbf{0}\\ \mathbf{0} & e^{j2kL_{1o}}\end{pmatrix} \text{ and } \mathbf{T}_{S2}=\begin{pmatrix}e^{j2kL_{2e}} & \mathbf{0}\\ \mathbf{0} & e^{j2kL_{2o}}\end{pmatrix}. \tag{3.8}$$

Similar to birefringence imaging, Eq. (3.7) is expanded and the second interference term (2*f*) can be obtained as

$$I_{2f}=\frac{\mathbf{1}}{\mathbf{4}}\sin^2 2\alpha I_0(k)e^{jk(L_{2e}-L_{1e}+L_{2o}-L_{1o})}\left[jB_S(k)+jB_B(k)+\mathbf{1}\right]e^{j2kL_C}. \tag{3.9}$$

For non-birefringent samples, the o- and e- waves are identical. When system birefringence is also ignored, Eq. (3.9) can be simplified to

$$I_{2f} = \frac{1}{4}\sin^2 2\alpha I_0(k) e^{j2k(L_2-L_1)} e^{j2kL_C}, \quad \textbf{(3.10)}$$

which, as expected, is essentially identical to the previously reported expression [18]. The quantitative DIC signal is simply the phase of downshifted I_{2f}.

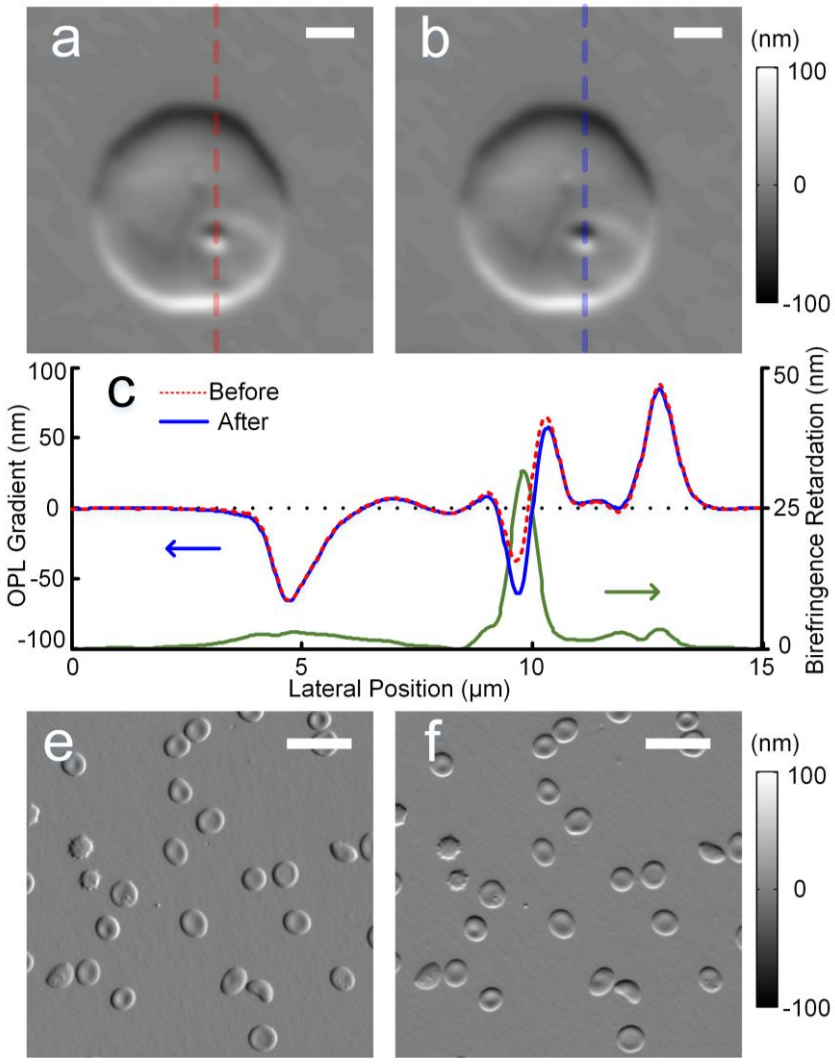

Figure 3.3. DIC gradient of an infected RBC before (a) and after (b) phase distortion correction. Scale bar 2μm. (c) Red and blue curves: OPL gradient along the lines in (a) and (b). Green curve: sample birefringence retardation along the same line. (e)(f) Corrected DIC images of RBCs with horizontal and vertical shear, respectively.

In contrast, for birefringent samples, the OPL gradient term in I_{2f} is $e^{jk(L_{2e}-L_{1e}+L_{2o}-L_{1o})}$. It can be interpreted as the average OPL gradients of o- and e- waves. Also, we have an additional complex term, $\left[jB_S(k) + jB_B(k) + \mathbf{1} \right]$, which is determined by system and sample birefringence. This birefringence-induced coefficient thus introduces a phase error in OPL gradient measurement. Fortunately, it is identical to the term in I_{2f} in Eq. (3.4), and is therefore already known from birefringence measurement. As a result, the birefringence-induced phase error can be corrected using the birefringence data.

Figure 3.3(a) and 3.3(b) show the OPL gradient images before and after the birefringence correction. In Fig. 3.3(c), closer examination of these DIC data reveals clear difference at the position of hemozoin crystal. The corrected positive and negative DIC peaks (blue) become symmetric about zero, which is a typical indication of birefringence-free DIC signal. This confirms that the phase error from sample anisotropy has been removed effectively. We also observe that, for low-birefringence areas away from the hemozoin, the OPL gradient data before and after correction are still in good agreement. The OPL gradient images of the infected RBCs after correction are also given in Figs. 3.3(e) and 3.3(f) for horizontal and vertical shear directions, respectively.

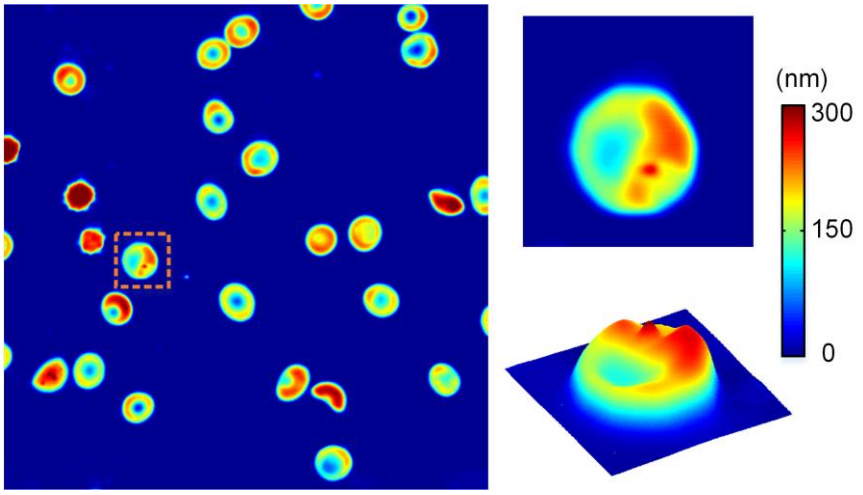

Figure 3.4. Quantitative phase image based on 2D integration of Figs. 3.3(e) and 3.3(f). Enlarged 2D OPL topography and 3D representation of the infected cell shown in Fig. 3.2(c).

Further, with these two directional OPL gradient images and 2D phase reconstruction algorithms [19, 20], quantitative phase image of the sample can be obtained. The process

involves image registration between the two gradient images and FFT-based 2D phase integration. The results are shown in Fig. 3.4.

3.5. Conclusion

In conclusion, we proposed and demonstrated a dual-modality system for quantitative birefringence and phase imaging. Imaging modes can be easily switched by the insertion and removal of a Nomarski prism. A unified theoretical treatment provides rigorous foundation for both techniques. From the theory, a process for system birefringence background subtraction is derived to improve birefringence measurement accuracy. This is particularly important for imaging live cells, whose birefringence is often weak and can be significantly distorted by background. The theory also enables the correction of birefringence-induced phase error, thus opens doors to precision phase imaging of birefringent samples. Experiments on *P. falciparum*-infected human RBCs demonstrate the system's capability for highly sensitive birefringence, DIC and phase imaging. Hemozoin crystals are visualized with high contrast and can potentially be used for quantitative study of crystal formation and growth. This highly integrated system may find applications in label-free imaging of biological specimens where multiple intrinsic contrasts are desired.

References

[1] F. Zernike, "Phase contrast, a new method for the microscopic observation of transparent objects," *Physica,* vol. 9, no. 7, pp. 686-698, Jul 1942.

[2] G. Nomarski, "Differential microinterferometer with polarized waves," *J. Phys. Radium,* vol. 16, no. 9, pp. 9S-11S, 1955.

[3] G. Popescu, *Quantitative phase imaging of cells and tissues*. McGraw Hill Professional, 2011.

[4] A. Changoor *et al.*, "A polarized light microscopy method for accurate and reliable grading of collagen organization in cartilage repair," *Osteoarthritis and Cartilage,* vol. 19, no. 1, pp. 126-135, Jan 2011.

[5] L. Cohen, R. Keynes, and B. Hille, "Light Scattering and Birefringence Changes during Nerve Activity," *Nature,* vol. 218, no. 5140, pp. 438-441, May 1968.

[6] Y. Abraham and R. Elbaum, "Quantification of microfibril angle in secondary cell walls at subcellular resolution by means of polarized light microscopy," *New Phytologist,* vol. 197, no. 3, pp. 1012-1019, 2013.

[7] R. Oldenbourg, E. Salmon, and P. Tran, "Birefringence of Single and Bundled Microtubules," *Biophysical Journal,* vol. 74, no. 1, pp. 645-654, Jan 1998.

[8] A. Dharmadhikari, H. Basu, J. Dharmadhikari, S. Sharma, and D. Mathur, "On the birefringence of healthy and malaria-infected red blood cells," *Journal of Biomedical Optics,* vol. 18, no. 12, p. 125001, 2013.

[9] Y. Otani, T. Shimada, T. Yoshizawa, and N. Umeda, "Two-dimensional birefringence measurement using the phase shifting technique," *Optical Engineering,* vol. 33, no. 5, pp. 1604-1609, 1994.

[10] I. H. Shin, S.-M. Shin, and D. Kim, "New, simple theory-based, accurate polarization microscope for birefringence imaging of biological cells," *Journal of Biomedical Optics,* vol. 15, no. 1, pp. 016028-6, 2010.

[11] J. Park, H. Yu, J.-H. Park, and Y. Park, "LCD panel characterization by measuring full Jones matrix of individual pixels using polarization-sensitive digital holographic microscopy," *Optics Express,* vol. 22, no. 20, pp. 24304-24311, Oct 2014.

[12] Z. Wang, L. Millet, M. Gillette, and G. Popescu, "Jones phase microscopy of transparent and anisotropic samples," *Optics Letters,* vol. 33, no. 11, pp. 1270-1272, Jun 2008.

[13] Y. Zhu, T. Takada, and Y. Murooka, "Two-dimensional optical measurement techniques based on optical birefringence effects," *Optical Engineering,* vol. 41, no. 12, pp. 3183-3192, 2002.

[14] M. Shribak and R. Oldenbourg, "Techniques for fast and sensitive measurements of two-dimensional birefringence distributions," *Applied Optics,* vol. 42, no. 16, pp. 3009-3017, Jun 2003.

[15] S. Aknoun, P. Bon, J. Savatier, B. Wattellier, and S. Monneret, "Quantitative retardance imaging of biological samples using quadriwave lateral shearing interferometry," *Optics Express,* vol. 23, no. 12, pp. 16383-16406, Jun 2015.

[16] C. Li and Y. Zhu, "Quantitative polarized light microscopy using spectral multiplexing interferometry," *Optics Letters,* vol. 40, no. 11, pp. 2622-2625, Jun 2015.

[17] C. Li and Y. Zhu, "Spectral-domain interferometry for quantitative DIC microscopy," vol. 8949, pp. 89491D-5, 2014.

[18] Y. Zhu, N. Shaked, L. Satterwhite, and A. Wax, "Spectral-domain differential interference contrast microscopy," *Optics Letters,* vol. 36, no. 4, pp. 430-432, Feb 2011.

[19] P. Bon, S. Monneret, and B. Wattellier, "Noniterative boundary-artifact-free wavefront reconstruction from its derivatives," *Applied Optics,* vol. 51, no. 23, pp. 5698-5704, Aug 2012.

[20] M. Arnison, K. Larkin, C. Sheppard, N. Smith, and C. Cogswell, "Linear phase imaging using differential interference contrast microscopy,", *Journal of microscopy,* vol. 214, no. Pt 1, pp. 7-12, Apr 2004.

Chapter 4 Quantitative Birefringence Spectroscopy on Gold Nanorods

Light scattered by a nanostructure alters the phase of the light in a manner that depends on incident light polarization and the polarizability of the nanostructure. In this chapter, quantitative birefringence spectroscopy technique is developed to provide insights into anisotropic nanostructures, even with the size of nanostructure within diffraction limit. The spectral signature of the scattered light from the nanostructure is measured using spectral multiplexing interferometry method. The footprint of nanostructure's plasmon resonance can be recorded by quantifying the scattering intensity and the birefringence information from detected interference spectra. As the quantifiable phase shift introduced by the scattering scales as D^3 for a particle of diameter D, birefringence spectroscopy can be much more sensitive than the typical intensity-based nanoparticle detection, which scales as D^6 and thus vanishes quickly for small particles. The sample of gold nanorod particles deposited on glass substrate is used to demonstrate the proposed technique. With the scattering properties of single gold nanorod particle computed with discrete dipole approximation, quantitative birefringence spectroscopy measurement was shown being able to determine the orientation and size/aspect ratio of nanorod particles using scattering intensity and birefringence information.

Attribution

For the work described in this chapter, the sample preparation of gold nanorod particles on glass substrate as well as scattering field numerical simulations were established by Zhixing He from Department of Physics, Virginia Tech.

4.1. Introduction

Fabricating precise, pre-determined, ordered constructs of nanoparticles is one of the greatest unsolved challenges of nanotechnology, and has attracted significant interest for decades [1]. A wide range of applications has also been developed based on plasmonic nanoparticles, such as dynamic biological labelling [2] and subwavelength integrated optics [3]. Optical detection and spectroscopic characterization of nanoparticles are thus desired. However, the nanoparticles behave as Rayleigh scatters, making themselves unfeasible to be characterized only by scattering intensity.

Light scattered from nanoparticles strongly depends on the composition, size, and shape of the nanostructures, as well as the wavelength and polarization of the incident light. The phase shift introduced by sub-tenth micron dielectric particles' scattering has been experimentally validated based on bright field interferometer decades ago [4]. Later on, researchers explored the possibility of single spherical nanoparticle detection based on plasmon spectra analysis using supercontinuum laser source [5]. The detected spectra were shown inherently related to the polarizability of nanoparticles.

As demonstrated in published works, the presence of a nanoparticle in a focused beam will cause a phase shift that scales as D^3, with D denoting the diameter of the nanoparticle. While anisotropic nanostructures have vastly different polarizabilities along different directions, the scattered light will exhibit phase birefringence that can be experimentally quantified. Characterizing the scattering intensity and the birefringence spectroscopic behavior of scattered light can provide unprecedented insights into nanoparticles' morphological structure and even their dynamic changes. The polarization state of scattered field will be inherently immune to the other scattered or non-scattered background, which enables quantitative characterization of the polarizability and the birefringence from anisotropic nanoparticles.

In the following, we first discuss Quantitative Birefringence Spectroscopy (QBS) technique implemented via Spectral Multiplexing Interferometry (SXI) method. The interference spectrum model is shown to be able to carry the birefringence and scattering intensity parameters related to the properties of detected nanostructures. To understand how the birefringence is formed, a physical model for the scattering field detected from nanorod particles is built up for both transmission and reflection cases, and shows the advantage of using weak-reflection measurement setup. Discrete Dipole Approximation (DDA) simulation has thus been established for estimating the polarizability of gold nanorod particles in experimental setup, which are deposited on glass-water interface under investigation. At last, the scattering intensity and birefringence spectra are measured on single gold nanorod particles and compared to the previous simulation results. The capability of QBS technique is demonstrated not only on determining the orientation of single gold nanorod particles, but also on analyzing the polarizability-induced spectroscopic behavior with the detected scattering field.

4.2. Quantitative Birefringence Spectroscopy System

Quantitative Birefringence Spectroscopy measurement is implemented based on SXI method, which was discussed in Chapter 2&3 [6, 7]. By generating spectral interference with polarization mixing, the intensity and phase/birefringence information from sample can be modulated onto carrier oscillations and further demodulated with interference spectra model.

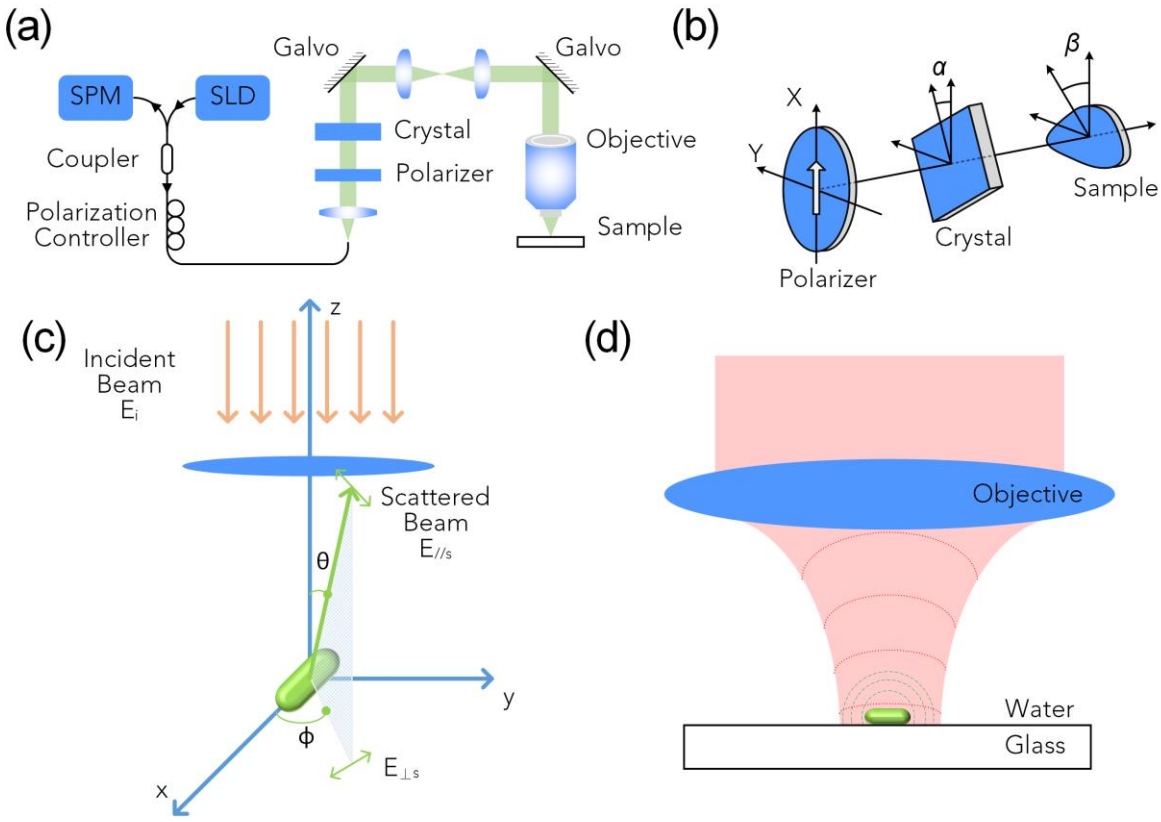

Figure 4.1. (a) Optical system setup for QBS measurement. (b) Polarization-related component alignment. (c) Illustration of incident beam and scattered light. (d) Schematics of interaction between a gold nanorod and focused optical field.

Figures 4.1(a) and 4.1(b) show a typical SXI configuration. Specifically, an optical birefringent crystal is used for polarization mixing in order to generate two carrier waves in a single detected spectrum, upon which both birefringence retardation and angle can be encoded and subsequently demodulated. Light from a broadband source passes through a linear polarizer and a birefringent crystal before being focused onto the detected specimen. Reflected light is again modified by the crystal/polarizer for polarization mixing and detected by a high-speed

spectrometer. Assuming the normalized Jones vector after the polarizer is $\begin{bmatrix}\mathbf{1} & \mathbf{0}\end{bmatrix}^{\mathrm{T}}$, the field after a double-pass transmission through the entire system can be obtained by

$$\mathbf{E}_{out} = \begin{bmatrix}\mathbf{1} & \mathbf{0}\end{bmatrix}\mathbf{R}(-\alpha)\mathbf{T_c}\mathbf{R}(\alpha-\beta)\mathbf{T_s}\mathbf{R}(\beta-\alpha)\mathbf{T_c}\mathbf{R}(\alpha)\begin{bmatrix}\mathbf{1}\\ \mathbf{0}\end{bmatrix}. \tag{4.1}$$

The derivation can follow the similar approach as stated in Chapter 2. The only difference is for sample matrix T_S, in addition to the birefringence retardation/orientation parameters, a scattering intensity ratio is also introduced. This is because the scattering intensity can be orientation-dependent for anisotropic nanostructures in focal plane. Thus the Jones Matrix for detected sample can be written as

$$T_s = \begin{pmatrix} s_2 e^{j\theta_{s2}} & \mathbf{0} \\ \mathbf{0} & s_1 e^{j\theta_{s1}} \end{pmatrix} = s_2 e^{j\theta_{s2}} \begin{pmatrix} \mathbf{1} & \mathbf{0} \\ \mathbf{0} & \frac{s_1}{s_2} e^{j(\theta_{s1}-\theta_{s2})} \end{pmatrix} = s_2 e^{j\theta_{s2}} \begin{pmatrix} \mathbf{1} & \mathbf{0} \\ \mathbf{0} & s' e^{j\theta_s} \end{pmatrix}, \tag{4.2}$$

where the scattering intensity ratio between the major/minor axes is denoted by $s' = \frac{s_1}{s_2}$ and birefringence retardation, i.e. the phase difference between major/minor axes, is $\theta_s = \theta_{s1} - \theta_{s2}$. Three unknown parameters can thus be found in the full Jones Matrix expression in Eq. (4.1): birefringence retardation θ_s, orientation β, and scattering intensity ratio s'.

The expression for the detected spectra can be derived with $I_0(k)$ denoting the spectrum envelope,

$$I(k,x,y) = I_0(k)\left|\mathbf{E}_{out}\right|^2 = s_1^2 I_0(k)\left\{I_{DC}(k) + \left[I_{1f}(k) + c.c.\right] + \left[I_{2f}(k) + c.c.\right]\right\},$$

$$I_{DC}(k) \overset{\theta_s = 0}{=} \cos^4\alpha + \sin^4\alpha,$$

$$I_{1f}(k) = e^{jkL_C}\cdot\left\{\begin{array}{l} -\frac{1}{2}\sin 2\alpha\cdot\sin 2(\alpha-\beta)\left[\sin^2(\alpha-\beta)\left(\cos^2\alpha s'^2 - \sin^2\alpha\right) + \right. \\ \left.\cos^2(\alpha-\beta)\left(-\cos^2\alpha + \sin^2\alpha s'^2\right) + \cos 2\alpha\cdot s'\cos\theta_s\cos 2(\alpha-\beta)\right] \\ -j\cdot\frac{1}{4}\cdot\sin 4\alpha\cdot\sin 2(\alpha-\beta)\cdot s'\sin\theta_s \end{array}\right\}, \qquad \textbf{(4.3)}$$

$$I_{2f}(k) = e^{j2kL_C}\cdot\left\{\begin{array}{l} \frac{1}{4}\sin^2 2\alpha\cdot\left[\frac{1}{4}\sin^2 2(\alpha-\beta)\left(1+s'^2\right) + \left(1 - \frac{1}{2}\sin^2 2(\alpha-\beta)\right)s'\cos\theta_s\right] \\ +j\cdot\frac{1}{4}\sin^2 2\alpha\cdot\cos 2(\alpha-\beta)\,s'\sin\theta_s \end{array}\right\}.$$

Two spectral carrier frequencies (1f and 2f) are thus created in the interference spectrum, corresponding to the single- and double-pass retardation of the crystal (kL_C and $2kL_C$). From the imaginary parts of two interference components, one can demodulate β and $s'\sin\theta_s$ as a function of wavelength. The real part of 2f term can be further used to separate s' and θ_s from $s'\sin\theta_s$.

With the above Jones Matrix derivation, theoretical analysis on QBS technique has shown its capability of not only finding the major axis orientation (β) for the polarizability of a given nanostructure, but also quantifying the scattering intensity ratio (s') and phase difference (θ_s) between major and minor axes. To reveal the size and shape information of detected nanoparticles based on the scattering and birefringence information, the scattering behavior of single anisotropic nanoparticles has to be understood first. The object for the following section is to establish a relationship between the physical size, shape and orientation of nanoparticles, and the parameters which can be detected using QBS technique, i.e. the scattering intensity ratio and the birefringence retardation/orientation.

4.3. Nanoparticle Scattering-induced Optical Birefringence

The case of a plasmonic nanostructure locating within the focal plane of a focusing lens will be discussed. Its schematic can be found in Fig. 4.1(c). Electrical field analysis method [8] is used to model the intensity and phase changes introduced on the incident light field, by given nanoparticles with known size, shape and orientation. We will start from general case to describe the relationship between incident field and scattered field. And it can be shown that, for anisotropic nanoparticles, the scattered field is determined by both the polarization of incident field and nanoparticles' polarizability. Both transmission-based and reflection-based measurement setups will be discussed for combined field expressions.

4.3.1. Scattered field analysis using scattering matrix

Assume a nanoparticle with its polarizability α_1, α_2 and α_3 along its three principal axes. Its principle axes are at angles to the main coordinate system (*xyz* or **123**) relative to the incident beam with a rotation transformation matrix $A=\{\alpha_{ij}\}$. The polarizability tensor can thus be expressed as

$$\alpha_{ij}=\alpha_{ji}=\sum_{k=1}^{3}\alpha_k a_{ki} a_{kj},\ or\ \{\alpha_{ij}\}=A^T\{\alpha_i\}A, \tag{4.4}$$

The relationship between scattered and incident field can be expressed using amplitude scattering matrix S as

$$\begin{pmatrix} E_{\|s} \\ E_{\perp s} \end{pmatrix}=\frac{e^{jkr}}{-jkr}\begin{pmatrix} S_2 & S_3 \\ S_4 & S_1 \end{pmatrix}\begin{pmatrix} E_{\|i} \\ E_{\perp i} \end{pmatrix}, \tag{4.5}$$

where the scattered field is uniformly divergent in far field (kr is large).

The corresponding amplitude scattering matrix can be written as

$$
\begin{aligned}
S_1 &= \frac{-ik^3}{4\pi}\left(\alpha_{11}\sin^2\varphi - 2\alpha_{12}\sin\varphi\cos\varphi + \alpha_{22}\cos^2\varphi\right),\\
S_2 &= \frac{-ik^3}{4\pi}\begin{bmatrix}\cos\theta\left(\alpha_{11}\cos^2\varphi + 2\alpha_{12}\sin\varphi\cos\varphi + \alpha_{22}\sin^2\varphi\right)\\ -\sin\theta\left(\alpha_{13}\cos\varphi + \alpha_{23}\sin\varphi\right)\end{bmatrix},\\
S_3 &= \frac{-ik^3}{4\pi}\begin{Bmatrix}\cos\theta\left[\alpha_{11}\sin\varphi\cos\varphi + \alpha_{12}\left(\sin^2\varphi - \cos^2\varphi\right) - \alpha_{22}\sin\varphi\cos\varphi\right]\\ -\sin\theta\left(\alpha_{13}\sin\varphi - \alpha_{23}\cos\varphi\right)\end{Bmatrix},\\
S_4 &= \frac{-ik^3}{4\pi}\left[\alpha_{11}\sin\varphi\cos\varphi + \alpha_{12}\left(\sin^2\varphi - \cos^2\varphi\right) - \alpha_{22}\sin\varphi\cos\varphi\right].
\end{aligned}
\tag{4.6}
$$

For simplicity, we will only discuss the nanoparticles with their principle axes aligned with xyz, $A = diag\{\alpha_i\}$. The amplitude scattering matrix in Eq. (4.3) can be simplified to

$$
\begin{aligned}
S_1 &= \frac{-ik^3}{4\pi}\left(\alpha_1\sin^2\varphi + \alpha_2\cos^2\varphi\right),\\
S_2 &= \frac{-ik^3}{4\pi}\cos\theta\left(\alpha_1\cos^2\varphi + \alpha_2\sin^2\varphi\right),\\
S_3 &= \frac{-ik^3}{4\pi}\cos\theta\left(\alpha_1 - \alpha_2\right)\sin\varphi\cos\varphi,\\
S_4 &= \frac{-ik^3}{4\pi}\left(\alpha_1 - \alpha_2\right)\sin\varphi\cos\varphi.
\end{aligned}
\tag{4.7}
$$

Placing the particle at the focal plane of a lens, whose optical axis is aligned with incident direction (z), we can study the scattered field in the Fourier plane of the lens. This is to convert spherical wave into plane-like wave in order to compare their polarization more readily.

For a focused incident beam polarized along x axis direction, its Fourier space field is also a plane wave polarized in x axis direction. As shown in Fig. 4.1(c), for scattered field, its Fourier space expression is

$$
\begin{pmatrix} E_s^x \\ E_s^y \end{pmatrix} = \begin{pmatrix} \cos\varphi & \sin\varphi \\ \sin\varphi & -\cos\varphi \end{pmatrix}\begin{pmatrix} E_{\parallel s} \\ E_{\perp s} \end{pmatrix}. \tag{4.8}
$$

In addition, the incident field experienced by the nanoparticle can be seen as a uniform plane wave since the size of nanoparticle is much smaller than the focused beam. The parallel and perpendicular components of incident field with polarization along x axis can be expressed as $\begin{pmatrix} E_{\|i} \\ E_{\perp i} \end{pmatrix} = \begin{pmatrix} \cos\varphi \\ \sin\varphi \end{pmatrix} E_0^c$, where E_0^c is the field amplitude at the beam center while in focus.

Suppose the incident light plane wave before focusing lens has a uniform field amplitude of E_0, the optical field amplitude distribution E_f at focal plane can be calculated using Fraunhofer approximation as

$$E_f\left(r_f\right) = e^{jkf_L} e^{j\frac{kr_f^2}{2f_L}} \frac{kD^2}{j8f_L} E_0 \frac{2J_1\left(kDr_f/2f_L\right)}{kDr_f/2f_L}, \tag{4.9}$$

where r_f denotes the distance from axis within focal plane, f_L is the focal length of objective length, D is the circular aperture diameter of the focusing lens, and J_1 is the Bessel function of first kind. Thus the relationship between focusing beam center amplitude E_0^c and plane wave amplitude at Fourier space E_0 can be determined as $\eta = \frac{E_0^c}{E_0} = \frac{kD^2}{8f_L^2} = \frac{1}{2}\left(\frac{NA}{n}\right)^2$, where NA denotes the numerical aperture of objective lens and n is the refractive index of the surrounding medium for the nanoparticle.

Based on Eqs. (4.4) and (4.5), the scattered field in Fourier plane of focusing lens can be shown as

$$\begin{aligned} E_s^x &= \frac{k^2}{4\pi} E_0^c \alpha_1 \left(\sin^2\varphi + \cos^2\varphi\cos\theta\right), \\ E_s^y &= \frac{k^2}{4\pi} E_0^c \alpha_1 \sin\varphi\cos\varphi\left(\cos\theta - 1\right), \end{aligned} \tag{4.10}$$

where a common term of $\frac{e^{jkr}}{r}$ is dropped for simplicity. It can be seen from above that the majority of power is in the x component. The y component is small, particularly for small θ. Regardless, due to y component being anti-symmetric about x and y axes with respect to ϕ,

the y component will not be coupled into the fundamental mode of the fiber, which is circularly symmetric, and thus can be ignored.

From above discussion, we can show that, along any direction within focal plane, the polarization component of scattered field introduced by nanoparticle is only related to its polarizability along this direction (α_1). For incident polarization along y axis, the above equation would change to α_2 . Therefore, in the following, we can drop the subscript noting that it is the polarizability of the axis aligned with the incident polarization.

4.3.2. Combined field analysis in Fourier plane of objective lens

The beam measured in the far field or at the detector is a combination of incident field and scattered field from the particle.

Take transmission based measurement setups for example, the incident field part, due to Gouy phase shift ($\pi/\mathbf{2}$ from focus to infinity or π between two extremes), can be expressed as

$$E_{inc} = \frac{e^{jkr}}{kr} E_{\mathbf{0}} e^{-j\frac{\pi}{\mathbf{2}}}. \tag{4.11}$$

After dropping $\frac{e^{jkr}}{r}$, the combined field in transmission mode can be written as

$$\begin{aligned} E_T &= E_{inc} + E_{scat}^{x} = \frac{-jE_{\mathbf{0}}}{k} + \frac{k^{\mathbf{2}}}{\mathbf{4}\pi} E_{\mathbf{0}}^{c} \alpha \left(\sin^{\mathbf{2}} \varphi + \cos^{\mathbf{2}} \varphi \cos\theta \right) \\ &= \frac{-jE_{\mathbf{0}}}{k} \left[\mathbf{1} + \frac{j\eta k^{\mathbf{3}}}{\mathbf{4}\pi} \alpha \left(\sin^{\mathbf{2}} \varphi + \cos^{\mathbf{2}} \varphi \cos\theta \right) \right] = \frac{-jE_{\mathbf{0}}}{k} \left[\mathbf{1} + \frac{j\eta k^{\mathbf{3}}}{\mathbf{4}\pi} \alpha f\left(\theta, \varphi\right) \right], \end{aligned} \tag{4.12}$$

where η has been shown to be a coefficient determined by the shape of the focused spot and $f\left(\theta, \varphi\right)$ represents an angular factor that is approximately one for moderately large range of θ.

Since α is complex in nature due to m being a complex number for metallic particles, we write

$$\alpha = \alpha_R + j\alpha_I, \tag{4.13}$$

where α_R and α_I have different spectroscopic behaviors. Equation (4.12) becomes

$$\begin{aligned} E_T &= \frac{-jE_0}{k}\left[\mathbf{1}+\frac{j\eta k^3}{\mathbf{4}\pi}\left(\alpha_R + j\alpha_I\right) f\left(\theta,\varphi\right)\right] \\ &= \frac{-jE_0}{k}\left[\mathbf{1}-\kappa\alpha_I + j\kappa\alpha_R\right] \propto \sqrt{\left(\mathbf{1}-\kappa\alpha_I\right)^2+\kappa^2{\alpha_R}^2}\, e^{j\arctan\frac{\kappa\alpha_R}{\mathbf{1}-\kappa\alpha_I}}, \end{aligned} \tag{4.14}$$

where $\kappa = \frac{\eta k^3 f}{\mathbf{4}\pi}$. Hence, the presence of a nanoparticle in a focused beam will cause an intensity variance as well as phase shift in the beam, which is related to the particle's polarizability along the incident polarization.

For reflection based measurement setups, the total reflected field under the first Born approximation is

$$E_R = rE_{inc} + j2rE_F - j(1+r^2)E_B, \tag{4.15}$$

where r represents the reflectance at substrate surface, E_F stands for the forward scattered field, and E_B represents the backward scattered field. Since nanoparticles can be modelled as Raleigh scatters in most cases, E_F and E_B are essentially the same.

The perfectly reflecting surface is not required in practice. In fact, a reduced reflection will help enhance the relative strength of E_B by rebalancing the intensity ratio between E_F and E_B. With an amplitude reflectivity of $r \ll \mathbf{1}$, the combined reflected field becomes

$$\begin{aligned} E_R &\cong rE_{inc} - jE_B \\ &= -\frac{jE_0}{k}\left[r+\kappa\alpha_I - j\kappa\alpha_R\right] \propto \sqrt{\left(r+\kappa\alpha_I\right)^2+\kappa^2{\alpha_R}^2}\, e^{-j\arctan\frac{\kappa\alpha_R}{r+\kappa\alpha_I}}. \end{aligned} \tag{4.16}$$

Therefore, a small r effectively eliminate E_F in Eq. (4.15), only backscattering needs to be considered. Since only one single scattering component left at this circumstance, it leads to the phase expression of weak reflective surface case similar to Eq. (4.14). Therefore, we can note the intensity parameter as $s = \sqrt{\left(r+\kappa\alpha_I\right)^2+\kappa^2{\alpha_R}^2}$ and the phase change as

$\theta_s = -\arctan\frac{\kappa\alpha_R}{r+\kappa\alpha_I}$. To take the sensitivity advantage of weak reflection based measurement setup, the actual experiment setup is illustrated in Fig. 4.1(d), which employs a water-immersion objective and a glass substrate.

4.3.3. Polarizability for special cases

To demonstrate how to measure polarizability-determined birefringence of anisotropic nanostructures using proposed QBS technique, we will use gold nanorod particles deposited on glass substrate as an anisotropic object representative. Although there's no exact solution to describe the polarizability of rod-like nanoparticles, a few special cases can be considered here to estimate the expecting birefringence signals from polarizability.

For a spheroid-shaped nanoparticle, exact solution can be found to describe its polarizability as $\alpha_i = \frac{\mathbf{4}\pi abc}{\mathbf{3}}\frac{m^2-\mathbf{1}}{L_i\left(m^2-\mathbf{1}\right)+\mathbf{1}}$, where $m^2 = \frac{\varepsilon_1}{\varepsilon_m}$ is dielectric constant ratio between particle and surrounding medium. For prolate (cigar-shaped) spheroids with $b = c$, $L_i = \frac{\mathbf{1}-e^2}{e^2}\left(-\mathbf{1}+\frac{\mathbf{1}}{\mathbf{2}e}\ln\frac{\mathbf{1}+e}{\mathbf{1}-e}\right)$, where $e^2 = \mathbf{1}-\frac{b^2}{a^2}$ is a factor related to the aspect ratio of the spheroid. Prolate spheroid can be used as a good approximation when describing the polarizability of rod-shaped nanoparticles. For a spheroid particle with moderate to large aspect ratio, the transverse polarizability α_2 (minor axis) may be neglected as compared to longitudinal value α_1 (major axis). Therefore, the detected phase term is mostly determined by the major polarizability component.

For an ideal nanosphere, its polarizability is constant for any direction so the measured θ_s will be zero. However, there will always be some level of asymmetry due to imperfect manufacturing. Simulations demonstrated in later part have shown that even a small deviation from aspect ratio 1 will create substantial change between α_1 and α_2, especially around its resonance peak.

In the following section, numerical simulations will be established to characterize the polarizability of the gold nanorod particles, and be further used as references in experimental validation.

4.4. Gold Nanorod Sample Preparation and DDA Simulations

Gold nanorod particles were fabricated and deposited on glass as an example of anisotropic nanoparticles to be investigated by QBS technique. To employ the sensitivity advantage of weak reflection measurement, a water-immersion objective will be used in the system to introduce a water-glass interface at the bottom of gold nanorod particles. The sample preparation procedure and scattering simulation method will be discussed as follows.

4.4.1. Gold nanorods preparation

The sample of gold nanorod particles on glass substrate is prepared by following procedures:

(a) Gold seeds preparation. Add 250μL of 0.01M chloroauric acid solution (gold solution) into the 0.1M 10ml Cetyltrimethylammonium Bromide (CTAB) solution in the vial under 28°C and stir vigorously. Add 600μL 0.01M $NaBH_4$ into the gold and CTAB solution quickly. Let it stir for 10 minutes. The solution should change to brown after the addition of $NaBH_4$. It is important to note that the gold solution mixture (chloroauric acid and CTAB) should be stirred vigorously, creating a vortex, before adding sodium borohydride. The seeds need to be stored at temperature 28-29°C in order to prevent CTAB crystallization and can be used within 24 hours.

(b) Synthesis of Gold nanorods. Gold nanorods are synthesized by hydroquinone reduction of gold ions and further reduction by gold seeds. The aspect ratio of the nanorods are controlled by changing the amounts of silver ions in the gold growth solution. Add 0.5mL of 0.01M $HAuCl_4$ (gold solution) to 10mL of 0.1M CTAB solution. Add 120μL of 0.1M AgNO3 (silver solution) and stir for 1min. Add 200uL 1M HCl and 80uL 0.1M L-Ascorbic Acid. Solution should turn completely transparent. This indicates that Au(III) is reduced to Au(I). Add 24μL of seeds solution. Gently stir at 28˚C for 3 hours and store overnight. Centrifuge at 3500rcf for 15 minutes to remove the supernatant and redisperse in DI water. The final products are red

to brown color depending on the amounts of silver solution. It varies red through brown with increasing silver amounts resulting in increasing the aspect ratios of gold nanorods. The centrifugation parameters may depend on the sample volume and concentration. Settling time can be estimated from the Stokes equation and optimized by trial and error. If temperature setting is available in the centrifuge, set it to 28°C to avoid crystallization of excess CTAB in the gold nanorod solution.

(c) Deposit gold nanorod on glass substrate. Centrifuge 1ml CTAB-coated nanorods solution at 3500rcf for 15 minutes once and replace supernatant with DI water. Add 300μL 5mM Poly Sodium-p-Styrenesulfonate (PSS) into the solution, and let the coating last for 2 hours under stir. Centrifuge PSS-coated nanorods at 3500rcf for 15 minutes twice and replace supernatant with DI water every time. For preparing Poly Allylamine Hydrochloride (PAH) coated substrate, immerse piranha cleaned, pre-cut glass substrate into PAH solution (10mM, pH=7) for 3 hours then rinse with DI water. Dilute PSS-coated nanorods by 80 times and dropcast on PAH film on silicon substrate for 2 hours. Rinse with DI water and blow dry, then the samples are ready to use.

4.4.2. Discrete Dipole Approximation

As for the numerical simulation approach to estimate the polarizability of fabricated gold nanorod particles, DDA method is used with the help of examples reported in [9-11]. Fortune code on Discrete Dipole Scattering (DDSCAT) introduced in [12] was used as analytical solution to understand near and far-field properties as well as scattered spectra quantitatively. Simulations were performed on Thunderbird cluster in Virginia Tech Physics Department. Task was split by wavelength.

The shape of the gold nanorod particles were generated by Blender. In this study particle width varies from 10nm to 30nm, and aspect ratio ranges from 2.5 to 5. The dielectric constant of gold is given by Johnson and Christy [13]. With dipole density equals 1 dipole/nm and the polarization of the incident light was set the same as the orientation of the GNR's long axis, DDA simulations performed on different incident wavelength varied from 600nm to 1000nm, with the step of 10nm. Complex amplitude scattering matrix was obtained for scattering angle from 0 to θ_{NA}.

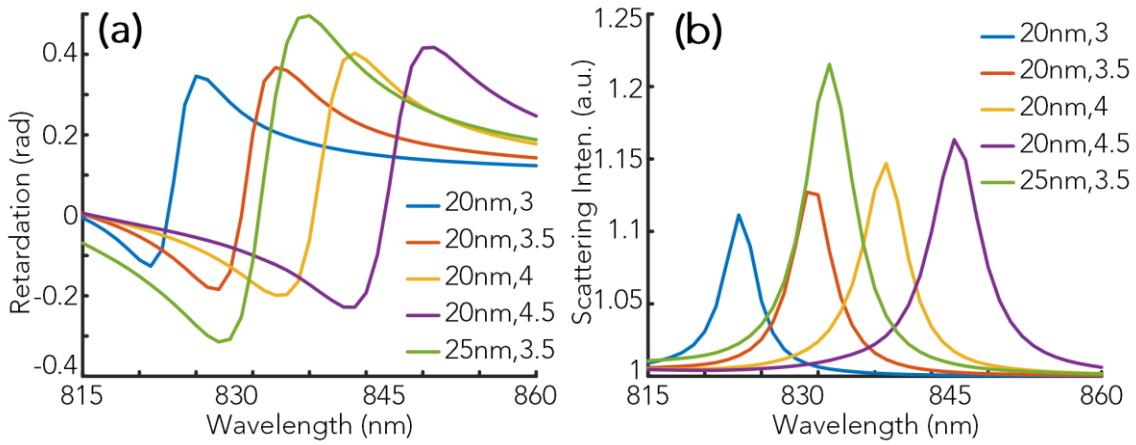

Figure 4.2. (a) Simulated retardation spectra and (b) simulated intensity ratio spectra between major/minor axes of gold nanorod particles on glass substrate in water environment using DDA simulation. Short axis diameter and long/short aspect ratio of nanorod particles were indicted in legend.

Figures 4.2(a) and 4.2(b) show the simulated birefringence retardation and scattering intensity ratio given by DDA simulation over gold nanorod particles on glass substrate, with different sizes and aspect ratios of nanorod indicated in legend. Simulations were established over estimated QBS system parameters for water-glass interface reflectance, objective NA, etc. As expected from anisotropic nanoparticle scattering behavior, the cross-zero region of birefringence retardation is largely determined by aspect ratio because of the shape of polarizability's real part, while the phase retardation magnitude is more related to the general particle size.

4.5. Quantitative Birefringence Imaging and Spectroscopic Analysis

Birefringence imaging and spectroscopic analysis were demonstrated with SXI system on individual gold nanorod particles on glass substrate. Water immersion microscope objective of NA 0.8 was used (corresponding to $\cos\theta_{NA} = 0.6$). Field of view was set as 15μm×15μm, while the integration time was 300μs for each interference spectrum acquisition. The averaging major/minor axis width for nanorod particles were pre-calibrated using TEM as 64nm/17nm (aspect ratio: 3.76). SEM image was also measured beforehand in the interest area, as shown in Fig. 4.3(a).

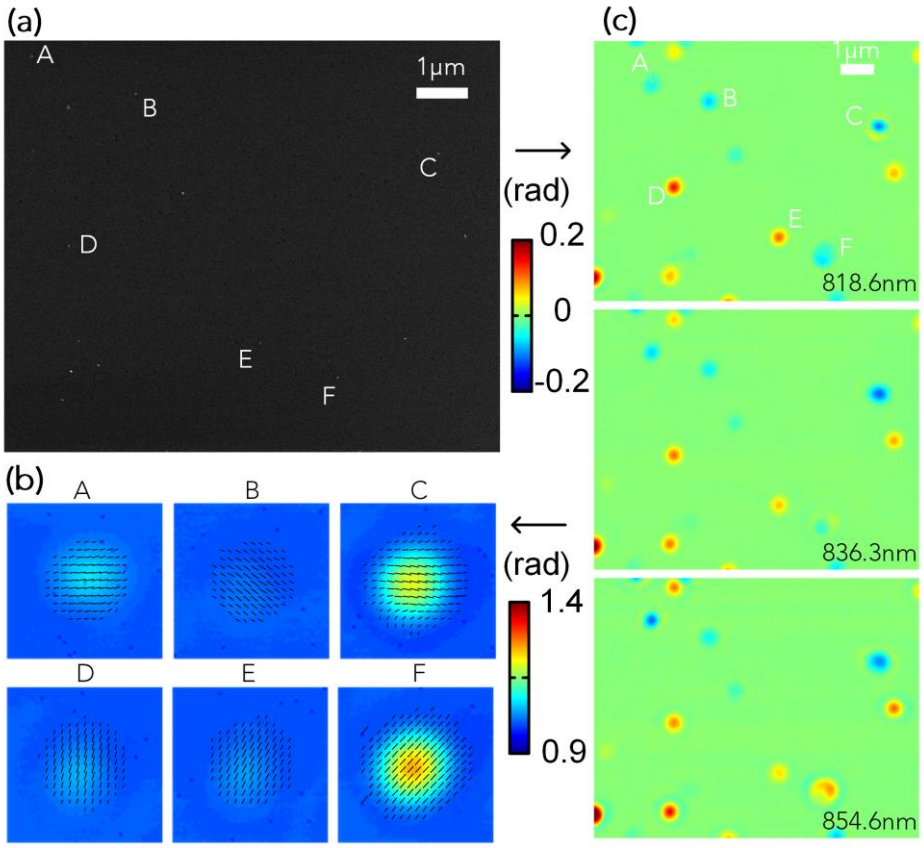

Figure 4.3. (a) SEM image in the interest area, with 6 single gold nanorod particles labelled for scattering and birefringence analysis. (c) Scattering intensity ratio s' and birefringence direction measured on nanorods labelled in (a). (c) Birefringence retardation θ_s for the interest area with respect to different wavelengths.

The scattering intensity ratio s' for each particle within detected wavelength range were illustrated in Fig. 4.3(b), along with the averaged birefringence direction β depicted with cursors. The length of the cursors also indicates the birefringence magnitude θ_s. It might be noted that, there is a 90˚ ambiguity for birefringence orientation angle β along with positive/negative sign of phase retardation. The birefringence direction for some of nanorod particles (B&C) in Fig. 4.3(b) was corrected by 90˚ based on SEM image, while the sign of phase retardation is also switched in the following spectroscopic analysis. The ambiguity can be avoided when a larger wavelength range being used for birefringence spectroscopy measurement.

Phase retardation measured on different wavelength (818.6nm, 836.3nm and 854.6nm) were shown in Fig. 4.3(c). The majority of nanorod particles show all positive/negative birefringence retardation within the detected wavelength range. However, for particle F, the retardation spectrum passes through 0 between different wavelengths, which indicates the sign of birefringence retardation changes in the detected wavelength range.

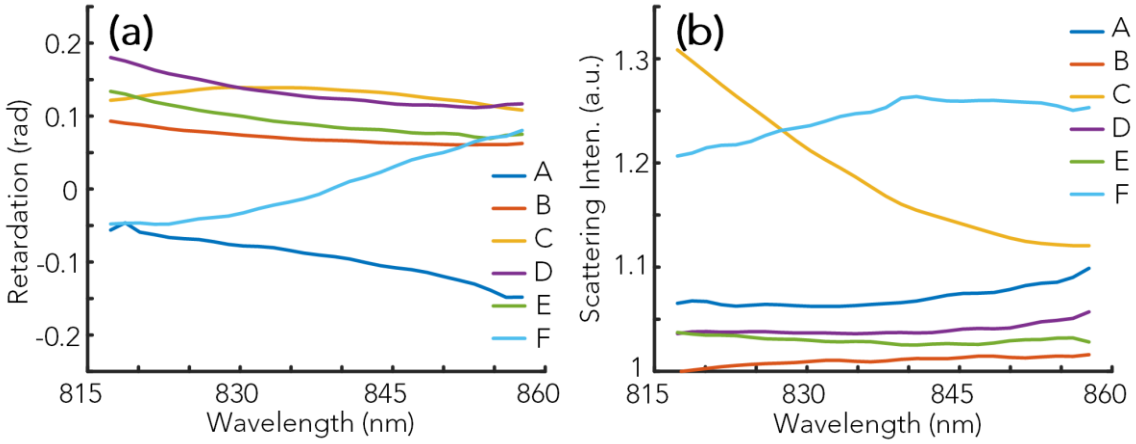

Figure 4.4. Measured (a) phase spectra θ_s and (b) scattering intensity ratio spectra s' from particles shown in Fig. 4.3.

The birefringence spectra and scattering intensity ratio measured on the particles (shown in Fig. 4.3) are depicted in Fig. 4.4. The phase retardation of particle F passes 0 at ~835nm, while its scattering intensity reaches the maxima as well. Meanwhile, the phase retardation of particle A is negative, implying this particle has a much smaller aspect ratio, when compared with adjacent particles in the scanning range. The birefringence retardation detected for particle C indicates the detected wavelength range locating around the positive extremum point on the real part of its polarizability, which can also be verified by relatively stronger scattering intensity detected.

4.6. Conclusions

Based on Jones Matrix analysis of the SXI setup, for a given anisotropic nanostructure under detection, the measured scattering intensity ratio and phase difference between its major and minor axes are originated from its shape-determined polarizability. The proposed QBS system can thus give simultaneous particle orientation and birefringence spectroscopy

measurement, which can further reveal size, shape and orientation information of nanostructures when DDA simulations are available to correlate birefringence and polarizability.

With QBS technique developed, quantitative birefringence spectroscopy measurement was demonstrated over gold nanorod particles deposited on glass substrate, with a weak reflection measurement setup. We showed that a small anisotropic nanoparticle within the focused beam can produce a scattered field with well detectable birefringence. Birefringence direction, retardation as well as scattering intensity ratio between two main axes were determined quantitatively. In addition, the size/aspect ratio information can also be estimated with nanorods' polarizability characterized with simulation.

For future work, a wider wavelength range is desired to avoid the ambiguity on sign of birefringence retardation along with direction (parallel/perpendicular) of nanoparticles' major axis orientation. As a label-free noncontact quantitative approach, QBS technique can also be used to study dynamic behavior of nanoparticles without any extra sample treatment.

References

[1] V. Sharma, K. Park, and M. Srinivasarao, "Colloidal dispersion of gold nanorods: Historical background, optical properties, seed-mediated synthesis, shape separation and self-assembly," *Materials Science and Engineering: R: Reports,* vol. 65, no. 1, pp. 1-38, 2009.

[2] O. Salata, "Applications of nanoparticles in biology and medicine," *Journal of Nanobiotechnology,* vol. 2, no. 1, p. 3, Apr 2004.

[3] H. Ditlbacher, J. R. Krenn, G. Schider, A. Leitner, and F. R. Aussenegg, "Two-dimensional optics with surface plasmon polaritons," *Applied Physics Letters,* vol. 81, no. 10, pp. 1762-1764, 2002.

[4] J. S. Batchelder and M. A. Taubenblatt, "Interferometric detection of forward scattered light from small particles," *Applied Physics Letters,* vol. 55, no. 3, pp. 215-217, 1989.

[5] K. Lindfors, T. Kalkbrenner, P. Stoller, and V. Sandoghdar, "Detection and Spectroscopy of Gold Nanoparticles Using Supercontinuum White Light Confocal Microscopy," *Physical Review Letters,* vol. 93, no. 3, p. 037401, 2004.

[6] C. Li and Y. Zhu, "Quantitative polarized light microscopy using spectral multiplexing interferometry," *Optics Letters,* vol. 40, no. 11, pp. 2622-2625, Jun 2015.

[7] C. Li, S. Chen, M. Klemba, and Y. Zhu, "Integrated quantitative phase and birefringence microscopy for imaging malaria-infected red blood cells," *Journal of Biomedical Optics*, 21(9), 090501, 2016.

[8] C. F. Bohren and D. R. Huffman, *Absorption and scattering of light by small particles*. John Wiley & Sons, 2008.

[9] T. Jensen, L. Kelly, A. Lazarides, and G. C. Schatz, "Electrodynamics of Noble Metal Nanoparticles and Nanoparticle Clusters," *Journal of Cluster Science,* vol. 10, no. 2, pp. 295-317, Jun 1999.

[10] K. L. Kelly, E. Coronado, L. L. Zhao, and G. C. Schatz, "The Optical Properties of Metal Nanoparticles: The Influence of Size, Shape, and Dielectric Environment," *The Journal of Physical Chemistry B,* vol. 107, no. 3, pp. 668-677, Jan 2003.

[11] E. Hao and G. C. Schatz, "Electromagnetic fields around silver nanoparticles and dimers," *The Journal of Chemical Physics,* vol. 120, no. 1, pp. 357-366, 2004.

[12] M. Liu, P. Guyot-Sionnest, T.-W. Lee, and S. K. Gray, "Optical properties of rodlike and bipyramidal gold nanoparticles from three-dimensional computations," *Physical Review B,* vol. 76, no. 23, p. 235428, 2007.

[13] P. B. Johnson and R. W. Christy, "Optical Constants of the Noble Metals," *Physical Review B,* vol. 6, no. 12, pp. 4370-4379, Dec 1972.

Chapter 5 Cramer-Rao Bounds of Parameter Estimation for Interference Signals

Interference frequency estimation is essential in spectral-domain interferometric sensing and imaging, and its performance determines system sensitivity. To date an objective and practical criterion is still absent for the proper evaluation of fundamental sensitivity limit in a given system. The Cramer-Rao bound (CRB) of such estimation determines measurement sensitivity limit. Unlike the well-studied complex sinusoids in communication theory, optical interference signal is distinctly different in its model parameters and noise statistics. The connection between these parameters and their estimation bounds has not been well understood. Here we propose a complete, realistic multi-parameter interference model corrupted by a combination of shot noise, dark noise and readout noise. We derive the Fisher information matrix and CRBs for all model parameters, including intensity, visibility, optical pathlength (frequency) and initial phase. We also show that CRBs of frequency and phase are coupled but not affected by the knowledge of intensity and visibility. Knowing the initial phase offers significant sensitivity advantage, which is verified by both theoretical derivations and numerical simulations. In addition to the complete model, a shot noise-limited case is studied, which permits the calculation of CRBs directly from measured data.

5.1. Introduction

Parameter estimation, in particular frequency estimation, of an optical interference in the presence of noise is a fundamental problem for interferometry applications [1, 2], with the lower limit of the variance of an unbiased estimator determined by CRB [3-6]. Given the fundamental similarity between spatial, temporal and spectral interference signals in modeling as well as processing, in this chapter we concentrate on spectral interference. The results can be readily generalized.

In the past decades, spectral interferometry has proved to be an effective approach for measuring optical pathlength (OPL) without ambiguity. With exquisite OPL estimation

sensitivity and large dynamic range, spectral interferometry is a widely used technique for a variety of applications, such as optical metrology [7, 8], fiber-optic sensing [9, 10], phase microscopy [11-13], and femtosecond spectroscopy [14].

Single-tone frequency estimation has been well studied in signal processing and communications [3-5, 15]. However, its typical model assumes a complex signal, constant amplitude, zero offset (DC), and uniform Gaussian noise. This is in clear contrast to a realistic signal model of spectral interferometry, which is real-valued and involves multiple additional parameters, such as spectrum envelope, fringe visibility, and initial phase. Since the spectral interference demodulation is a multi-parameter estimation problem, the knowledge of certain parameters may greatly affect the estimation bounds (sensitivity) of other parameters. To date, a systematic analysis of such bounds based on a realistic interference model is still absent. Importantly, the impact of these unknown parameters on the sensitivity of OPL (frequency) estimation has not been well understood.

In addition to these new interference parameters, we also adopt a new approach for noise modeling [16]. Most existing works are based on uniform, Gaussian, white noise models that are standard in communication theory [6, 15, 16]. In contrast, optical detection is typically dominated by Poisson shot noise, which is non-uniform across an interference spectrum due to intensity oscillation. It also involves dark noise (Poisson) and readout noise (Gaussian), although to a much lesser extent. Our previous work [17] considered a complete noise statistics model but assumes OPL as the only unknown parameter. Therefore, how to analyze multiple noise sources with different statistical behaviors and to derive the CRB for a complete model with multiple unknown parameters poses another challenge in finding the sensitivity limit of interference signal demodulation.

In this chapter, a complete, multi-parameter interference signal model is introduced, corrupted by a combination of shot noise, dark noise and readout noise. A Poisson random variable (RV) approach is then utilized to derive the Fisher information matrix and the associated CRBs for all parameters. In addition, we discuss the shot noise-limited case and its sensitivity performance through both theory and simulation.

5.2. Interference Spectrum Model and Cramer-Rao Bounds

5.2.1. Interference spectrum model

To derive the sensitivity limit for the estimation of interference parameters, such as spectral interference frequency, a statistical model of the spectrum is needed. The digital readout from the detector is used to define the model, which allows the estimation results to be directly accessed from spectral data and thus be more convenient for practical uses.

For a typical two-beam spectral interferometry, we can consider a sinusoidal signal model as

$$\bar{I}_n = I_0 \alpha_n \left[1 + V \cos\left(k_n L + \varphi \right) \right], \tag{5.1}$$

where $\bar{I}_n$ is the noise-free interference spectral intensity in analog-to-digital unit (ADU), I_0 is the spectrum intensity defined in ADU as well, α_n is normalized source spectral envelope, V is visibility, k_n is sampling wavenumbers, L is OPL (frequency) and the main subject of estimation, and φ is a system-specific phase term.

Among all model parameters, we will consider α_n and k_n as known, since the source spectrum envelope and sampling wavenumbers are determined by light source and detector, and can be well pre-calibrated. Here we use Θ to denote the vector of unknown parameters from the interference spectrum observation. If I_0 , V , L , φ are all unknown, $\Theta = \left[\theta_1, \theta_2, \theta_3, \theta_4 \right]$ $= \left[I_0, V, L, \varphi \right]$.

With the expected interference signal model, we denote a detected spectrum as $\mathbf{X} = \left[x_1, ..., x_n \right]$, with $\mathbf{X}$ representing a noise-corrupted observation of $E\left(x_n \right)$ and x_n being the number of electrons for the n-th wavenumber. For a typical spectral interferometry system, the detected spectrum consists of three independent components,

$$x_n = s_n + d_n + r_n, \tag{5.2}$$

where s_n is the number of photo-generated electrons representing the interference signal with shot noise. It follows Poisson distribution $Po(s_n; g\bar{I}_n)$, with g being the conversion/camera gain, i.e. the number of electrons per ADU.

In addition to shot noise, dark noise and readout noise are another two components in the detected spectrum with well understood behavior. Two RVs d_n and r_n are included in Eq. (5.2) respectively, with d_n standing for the number of thermally generated electrons (dark current), and r_n representing readout electron fluctuations. We assume uniform dark current and readout noise for all sampling points. Hence d_n follows Poisson distribution $Po(d_n; g\bar{I}_d)$ with $\bar{I}_d$ being the dark current intensity in ADU, and the readout noise r_n is modeled as a zero-mean Gaussian distribution $N(r_n; \mathbf{0}, \sigma_r^2)$ [17].

5.2.2. Fisher information matrix and Cramer-Rao bounds

For each unknown parameter θ_i in the vector Θ, the signal processing algorithm produces an estimator $\hat{\theta}_i$ from the detected spectrum $\mathbf{X}$ with certain random error. For unbiased estimators, the variance of $\hat{\theta}_i$ satisfies $\sigma_{\theta_i}^2 \geq CRB_{\theta_i}$, which means that the measurement sensitivity of θ_i cannot be better than CRB_{θ_i}. Here the sensitivity is defined as the standard deviation of a parameter estimation, i.e. the root of the variances between multiple estimations.

As known from estimation theory and statistics, the unbiased CRBs are the diagonal elements of the inverse of the Fisher information matrix J, i.e. $CRB_{\theta_i} = \left[J^{-1} \right]_{ii}$. And the element of Fisher information matrix can be expressed as

$$J_{ij} = E\left\{ \frac{\partial}{\partial \theta_i} \ln P\left(\mathbf{X}; \Theta\right) \frac{\partial}{\partial \theta_j} \ln P\left(\mathbf{X}; \Theta\right) \right\} = -E\left\{ \frac{\partial^2}{\partial \theta_i \partial \theta_j} \ln P\left(\mathbf{X}; \Theta\right) \right\}, \qquad \textbf{(5.3)}$$

where $E\{\cdot\}$ denotes the expected value with respect to the sample vector $\mathbf{X}$, and $P\left(\mathbf{X}; \Theta\right)$ stands for the joint probability distribution function (PDF) of the elements in $\mathbf{X}$.

Using Eq. (5.2) as the statistics model, we can derive CRB for each unknown parameter. However, the joint PDF of Poisson and Gaussian RVs is difficult to process. To simplify its derivation, a Poisson distribution model is used for x_n with the Gaussian RV r_n being approximated by a Poisson RV in Section 5.3. CRBs for all unknown parameters are derived. Section 5.4 follows with a detailed discussion on the shot noise-limited case (s_n only). The implication of these results is discussed in Section 5.5.

5.3. CRB of Complete Model using Poisson RV

As stated in the interference signal model, s_n and d_n are Poisson RVs with r_n typically being modeled as a Gaussian RV. In this section, a Poisson RV is used to approximate the complete signal model x_n and to derive the CRBs for the unknown parameters in Θ.

Practically, a Gaussian distribution $N(x;\lambda,\lambda)$ can often be very well approximated as a Poisson distribution $Po(x;\lambda)$ when λ is not too small. Therefore, a shifted read noise $r_n+\sigma_r^2$, which follows $N(r_n;\sigma_r^2,\sigma_r^2)$, can be considered to be $Po(r_n;\sigma_r^2)$. Adding σ_r^2 to both sides of Eq. (5.2) leads to a shifted complete model,

$$x_n' = x_n + \sigma_r^2 = s_n + d_n + (r_n + \sigma_r^2), \tag{5.4}$$

which becomes the sum of three independent Poisson RVs and also Poisson. Therefore the shifted complete model follows Poisson distribution $Po(x_n';\lambda_n)$, with its rate being the combined rate of all three components, i.e. $\lambda_n = g\bar{I}_n + g\bar{I}_d + \sigma_r^2$.

Then we can follow the standard CRB derivation with the knowledge that $P(\mathbf{X};\Theta) = P(\mathbf{X}';\Theta)$ and each x_n' is an independent Poisson RV. The likelihood function of having observed the data vector $\mathbf{X}$ given Θ can be expressed as

$$P(\mathbf{X};\Theta) = \prod_{n=1}^{N} \frac{\lambda_n^{x_n'} \cdot e^{-\lambda_n}}{x_n'!}. \tag{5.5}$$

Therefore, the derivatives can be obtained as

$$\frac{\partial}{\partial \theta_i} \ln P\left(\mathbf{X};\Theta\right) = \sum_{n=1}^{N}\left[\left(\frac{x_n^{'}}{\lambda_n} - \mathbf{1}\right)\cdot\frac{\partial \lambda_n}{\partial \theta_i}\right], \tag{5.6}$$

and

$$\frac{\partial^2}{\partial \theta_i \partial \theta_j} \ln P\left(\mathbf{X};\Theta\right) = \sum_{n=1}^{N}\left[\left(\frac{x_n^{'}}{\lambda_n} - \mathbf{1}\right)\cdot\frac{\partial^2 \lambda_n}{\partial \theta_i \partial \theta_j} - \frac{x_n^{'}}{\lambda_n^{\,2}}\cdot\frac{\partial \lambda_n}{\partial \theta_i}\cdot\frac{\partial \lambda_n}{\partial \theta_j}\right]. \tag{5.7}$$

Its expected value is determined by the rate of the shifted complete model x_n', i.e. $E\left(x_n'\right) = \lambda_n = g\bar{I}_n + g\bar{I}_d + \sigma_r^2$. The expression for the element of the Fisher information matrix can then be written as

$$J_{ij} = \sum_{n=1}^{N}\left\{-\left[\frac{E\left(x_n^{'}\right)}{\lambda_n} - \mathbf{1}\right]\cdot\frac{\partial^2 \lambda_n}{\partial \theta_i \partial \theta_j} + \frac{E\left(x_n^{'}\right)}{\lambda_n^{\,2}}\cdot\frac{\partial \lambda_n}{\partial \theta_i}\cdot\frac{\partial \lambda_n}{\partial \theta_j}\right\} = \sum_{n=1}^{N}\left(\frac{\mathbf{1}}{\lambda_n}\cdot\frac{\partial \lambda_n}{\partial \theta_i}\cdot\frac{\partial \lambda_n}{\partial \theta_j}\right). \tag{5.8}$$

As dark noise and read noise are both irrelevant to the estimated parameters in Θ, which means $\frac{\partial \lambda_n}{\partial \theta_i} = g\frac{\partial \bar{I}_n}{\partial \theta_i}$ can also be substituted into the above equation to produce

$$J_{ij} = \sum_{n=1}^{N}\left(\frac{g^2}{g\bar{I}_n + g\bar{I}_d + \sigma_r^2}\cdot\frac{\partial \bar{I}_n}{\partial \theta_i}\cdot\frac{\partial \bar{I}_n}{\partial \theta_j}\right). \tag{5.9}$$

With the unknown parameter vector $\Theta = \left[I_0, V, L, \varphi\right]$, the elements for Fisher information matrix can be calculated accordingly,

$$J_{11}=\frac{g}{I_0}\sum_{n=1}^{N}\alpha_n\left[1+V\cos\left(k_nL+\varphi\right)\right]Q\left(\Theta,n\right),\qquad J_{23}=J_{32}=-\frac{V}{2}\sum_{n=1}^{N}k_n\sin 2\left(k_nL+\varphi\right)R\left(\Theta,n\right),$$

$$J_{12}=J_{21}=g\sum_{n=1}^{N}\alpha_n\cos\left(k_nL+\varphi\right)Q\left(\Theta,n\right),\qquad J_{24}=J_{42}=-\frac{V}{2}\sum_{n=1}^{N}\sin 2\left(k_nL+\varphi\right)R\left(\Theta,n\right),$$

$$J_{13}=J_{31}=-gV\sum_{n=1}^{N}\alpha_nk_n\sin\left(k_nL+\varphi\right)Q\left(\Theta,n\right),\quad J_{33}=\sum_{n=1}^{N}k_n{}^2T\left(\Theta,n\right), \tag{5.10}$$

$$J_{14}=J_{41}=-gV\sum_{n=1}^{N}\alpha_n\sin\left(k_nL+\varphi\right)Q\left(\Theta,n\right),\qquad J_{34}=J_{43}=\sum_{n=1}^{N}k_nT\left(\Theta,n\right),$$

$$J_{22}=\sum_{n=1}^{N}\cos^2\left(k_nL+\varphi\right)R\left(\Theta,n\right),\qquad J_{44}=\sum_{n=1}^{N}T\left(\Theta,n\right),$$

where the notations are defined as follows,

$$Q\left(\Theta,n\right)=\frac{I_0\alpha_n\left[1+V\cos\left(k_nL+\varphi\right)\right]}{I_0\alpha_n\left[1+V\cos\left(k_nL+\varphi\right)\right]+\bar{I}_d+\sigma_r^2/g},$$

$$R\left(\Theta,n\right)=\frac{gI_0{}^2\alpha_n{}^2}{I_0\alpha_n\left[1+V\cos\left(k_nL+\varphi\right)\right]+\bar{I}_d+\sigma_r^2/g}, \tag{5.11}$$

$$T\left(\Theta,n\right)=\frac{gI_0{}^2\alpha_n{}^2V^2\sin^2\left(k_nL+\varphi\right)}{I_0\alpha_n\left[1+V\cos\left(k_nL+\varphi\right)\right]+\bar{I}_d+\sigma_r^2/g}.$$

The Fisher information matrix for any other unknown parameter combination can be obtained directly from Eqs. (5.10) and (5.11). For example, if V is known with $\Theta=\left[I_0,L,\varphi\right]$, then J is the 3-by-3 matrix obtained by deleting the second row and second column from Eq. (5.10).

It can be well noted that all the elements in the matrix are summations across all sampling points and wavenumbers. Highly accurate approximations can thus be applied to significantly simplify the CRB derivation. The condition is that L is relatively large such that a number of interference fringes are present within the spectral range. In other words, in the Fourier transform of Eq. (5.1), the interference peak is well separated from the DC peak. This is a condition that is almost always met in modern metrology and sensing applications.

Here $Q(\Theta,n)$ and $R(\Theta,n)$ are Θ-determined functions with non-negative values and related to $\cos(k_nL+\varphi)$ only. In addition, α_n and k_n both act as slow varying envelope factors. Therefore, if some fast oscillating components, such as $\sin(\cdot)$ or $\cos(\cdot)$ due to large L, are multiplied with above non-negative factors, the integral of their product is vanishingly small and negligible compared to the integration of non-negative component. For example, the second component $\sum_{n=1}^{N}\alpha_n V\cos(k_nL+\varphi)Q(\Theta,n)$ in J_{11} is negligibly small when compared with the first component $\sum_{n=1}^{N}\alpha_n Q(\Theta,n)$. The validity of this approximation will be examined with simulations in next section.

Apply similar approximations to all the matrix elements, the simplified Fisher information matrix can be shown as

$$J=\begin{bmatrix} \frac{g}{I_0}\sum_{n=1}^{N}\alpha_n Q(\Theta,n) & \mathbf{0} & \mathbf{0} & \mathbf{0} \\ \mathbf{0} & \sum_{n=1}^{N}\cos^2(k_nL+\varphi)R(\Theta,n) & \mathbf{0} & \mathbf{0} \\ \mathbf{0} & \mathbf{0} & \sum_{n=1}^{N}k_n{}^2T(\Theta,n) & \sum_{n=1}^{N}k_nT(\Theta,n) \\ \mathbf{0} & \mathbf{0} & \sum_{n=1}^{N}k_nT(\Theta,n) & \sum_{n=1}^{N}T(\Theta,n) \end{bmatrix}. \quad \textbf{(5.12)}$$

It can be seen that the behavior of I_0 (J_{11}) is decoupled from other parameters, and so is V (J_{22}). The elements of L and φ, however, are coupled to each other, but are independent from I_0 and V. The inverse of above Fisher information matrix then leads to following sets of CRBs for the unknown parameters in Θ:

(a) CRB for I_0 no matter other parameters are known or unknown :

$$\sigma_{I_0} \geq \left[\frac{g}{I_0} \sum_{n=1}^{N} \alpha_n Q(\Theta, n) \right]^{-1/2}. \tag{5.13}$$

(b) CRB for V no matter other parameters are known or unknown:

$$\sigma_V \geq \left[\sum_{n=1}^{N} \cos^2 (k_n L + \varphi) R(\Theta, n) \right]^{-1/2}. \tag{5.14}$$

As we can see, the OPL and phase sensitivity bounds are independent to known or unknown of spectral intensity and interference visibility.

(c) CRB for L if φ is unknown and I_0, V known or not:

$$\sigma_{L-I} \geq \left[\frac{\sum_{n=1}^{N} T(\Theta, n) \cdot \sum_{n=1}^{N} k_n^2 T(\Theta, n) - \left[\sum_{n=1}^{N} k_n T(\Theta, n) \right]^2}{\sum_{n=1}^{N} T(\Theta, n)} \right]^{-1/2}. \tag{5.15}$$

CRB for L if φ is known and I_0, V known or not:

$$\sigma_{L-II} \geq \left[\sum_{n=1}^{N} k_n^2 T(\Theta, n) \right]^{-1/2}, \tag{5.16}$$

which is identical to our previous derivation under much restricted assumptions of known I_0, V, φ [17].

(d) CRB for φ if L is unknown and I_0, V known or not:

$$\sigma_{\varphi-I} \geq \left[\frac{\sum_{n=1}^{N} T(\Theta, n) \cdot \sum_{n=1}^{N} k_n^2 T(\Theta, n) - \left[\sum_{n=1}^{N} k_n T(\Theta, n) \right]^2}{\sum_{n=1}^{N} k_n^2 T(\Theta, n)} \right]^{-1/2}. \tag{5.17}$$

CRB for φ if L is known and I_0, V known or not:

$$\sigma_{\varphi-II} \geq \left[\sum_{n=1}^{N} T\left(\Theta, n\right)\right]^{-1/2}. \tag{5.18}$$

It can be seen that the demodulation sensitivity of OPL is irrelevant to the knowledge of I_0 or V and only depends on whether φ is known or not. To date, numerous algorithms have been proposed to demodulate the OPL of an interference spectrum, which can be classified into two types based on whether φ is known or unknown. With φ unknown or unused, σ_{L-I} gives the sensitivity bound for Type I demodulation algorithms, while σ_{L-II} is the bound for Type II demodulation with a known φ. It can be easily shown from Eqs. (5.15) and (5.16) that $CRB_{L-I} \geq CRB_{L-II}$, which indicates a known φ will introduce a sensitivity ratio for OPL demodulation. The sensitivity ratio can be significant and will be further addressed in the following section.

5.4. CRB for Shot Noise-limited Case

5.4.1. Shot noise-limited model

In the majority of modern interferometry applications, photo-generated electrons are mostly dominant so that $x_n = s_n$. In this section, we will focus on shot noise-limited case, with d_n and r_n removed from the interference signal model. The derivations in Section 5.3 are still applicable, with x_n following Poisson distribution $Po\left(x_n; \lambda_n\right)$ and $\lambda_n = g\bar{I}_n$.

The Fisher information matrix expression for shot noise-limited case is identical to Eq. (5.10) but with an updated version of Eq. (5.11) as

$$\begin{aligned} Q\left(\Theta, n\right) &= \mathbf{1}, \\ R\left(\Theta, n\right) &= \frac{gI_0\alpha_n}{\mathbf{1} + V\cos\left(k_n L + \varphi\right)}, \\ T\left(\Theta, n\right) &= \frac{gI_0\alpha_n V^2 \sin^2\left(k_n L + \varphi\right)}{\mathbf{1} + V\cos\left(k_n L + \varphi\right)}. \end{aligned} \tag{5.19}$$

Take Type II OPL demodulation as an example, CRB for L with the knowledge of φ can be expressed as

$$\sigma_{L-II} \geq \left[gV^2 \sum_{n=1}^{N} \frac{I_0 \alpha_n k_n^{\,2} \sin^2\left(k_n L+\varphi\right)}{1+V\cos\left(k_n L+\varphi\right)} \right]^{-1/2}. \tag{5.20}$$

With this much simplified version of CRB, it can be seen that higher values of I_0, α_n and V lead to a smaller σ_{L-II}, indicating a better estimation performance. This can be easily interpreted since higher demodulation sensitivity can be achieved from interference spectrum with a better SNR.

5.4.2. Sensitivity ratio with known φ

With the simplified CRB expressions of shot noise-limited model discussed above, the sensitivity ratio from Type I to Type II OPL demodulation can be characterized as

$$G_{I-II} = \frac{\sum_{n=1}^{N} T\left(\Theta,n\right) \cdot \sum_{n=1}^{N} k_n^{\,2} T\left(\Theta,n\right)}{\sum_{n=1}^{N} T\left(\Theta,n\right) \cdot \sum_{n=1}^{N} k_n^{\,2} T\left(\Theta,n\right) - \left[\sum_{n=1}^{N} k_n T\left(\Theta,n\right)\right]^2}, \tag{5.21}$$

with $T\left(\Theta,n\right)$ defined in Eq. (5.19).

Still the expression is somewhat complicated, so simulations are used to study the sensitivity difference between Type I and Type II methods. The values of simulation parameters are as follows [17]: $N=\mathbf{1024}$, $I_0=\mathbf{2000}$, $V=\mathbf{0.9}$, $L=\mathbf{200}\mu m$, $\varphi=\mathbf{0}^\circ$, $g=\mathbf{43.7}e^-/ADU$, k_n is evenly spaced in [800nm, 880nm], and background envelope α_n is a Gaussian window generated with built-in function *gausswin* in Matlab R2016a ($\alpha=\mathbf{2.5}$) with its peak value of 1. The simulated spectrum has approximately 23 sinusoid periods, which can be estimated as $\frac{\left|k_1-k_n\right|L}{2\pi}$. The sensitivity ratio G_{I-II} is calculated as 54.96, which indicates that a knowledge of φ can significantly improve the measurement sensitivity of OPL.

The sensitivity ratio G_{I-II} has also been studied with varying V and L, as shown in Fig. 5.1(a)(b). The ratio between the sensitivities of Type I and Type II OPL demodulation stay essentially unchanged across the entire visibility range or over each relatively large OPL. In addition, from simulations using a wide range of parameters, G_{I-II} is shown to be largely independent of N, I_0, V, L, φ and g. While the independence of I_0 and g is obvious from their proportionality in Eq. (5.19) so they are cancelled in the ratio, it is challenging to analytically prove the independence of G_{I-II} on other parameters since they are involved in the form of $V\cos\left(k_n L+\varphi\right)$ and $V\sin\left(k_n L+\varphi\right)$. But qualitatively, the fast oscillation approximation used earlier can be again adopted to understand this independence of these terms. Additionally, the conclusion from simulations can be validated using a special case of the shot noise-limited model. When $V\to\mathbf{0}$,

$$G_{I-II}\xrightarrow{V\to\mathbf{0}}\frac{\sum_{n=1}^{N}\alpha_n\cdot\sum_{n=1}^{N}\alpha_n k_n^{\,2}}{\sum_{n=1}^{N}\alpha_n\cdot\sum_{n=1}^{N}\alpha_n k_n^{\,2}-\left[\sum_{n=1}^{N}\alpha_n k_n\right]^2}. \tag{5.22}$$

Since G_{I-II} has been shown to be largely independent of V, the sensitivity ratio shown in Eq. (5.22) can thus be applied to general cases, as G_{I-II} is primarily determined by α_n and k_n. As a result, Type II demodulation methods have a fixed, quasi-constant sensitivity advantage over Type I methods if the light source (α_n) and detector (k_n) remain fixed for the interferometry system. For example, the ratio changes to 36.39 when a uniform background envelope is assumed for the interference signal. The sensitivity ratio has also been calculated with different sets of k_n, as illustrated in Fig. 5.1(c). The sensitivity ratio raises to 109.55 when k_n is evenly spaced in [820nm, 860nm], and becomes 18.36 with a wider wavelength range of [720nm, 960nm]. In all cases, this indicates a significant sensitivity advantage of 1-2 orders of magnitude for Type II OPL demodulation methods.

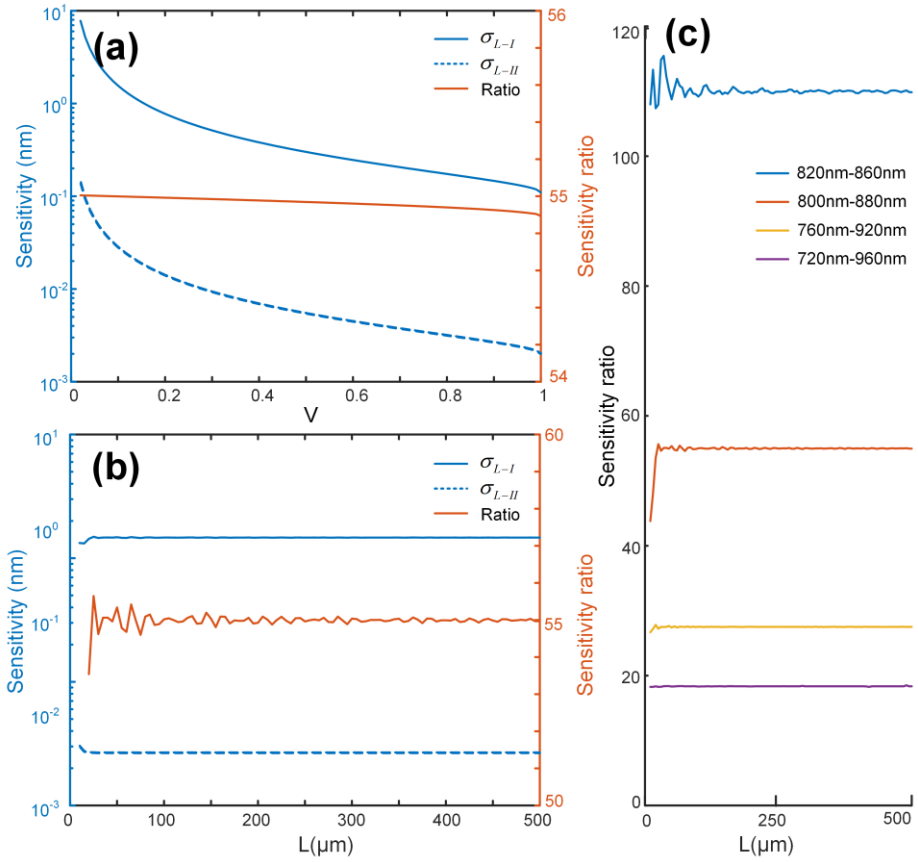

Figure 5.1. Comparison of CRBs for Type I and Type II OPL demodulation and their ratio with (a) different interference visibilities and (b) different OPLs, (c) sensitivity ratio over different wavelength ranges.

5.4.3. Approximation efficiency for fisher information matrix

Since all the derived CRBs depends on the validity of the applied approximations from Eq. (5.10) to Eq. (5.12), numerical simulations have been carried out to examine its robustness. Two sets of CRBs are calculated using the same simulation parameters as in Section 5.4.2 and compared in Table 5.1: one from the original Fisher information matrix in Eq. (5.10) and the other from the simplified matrix in Eq. (5.12). Relative difference for each CRB has been shown to be minimal, which demonstrates remarkable agreement between the accurate and approximated Fisher information matrix.

Table 5.1. Comparison of Accurate and Approximated Fisher Information Matrix

	CRB From Original Fisher Information Matrix	CRB From Fisher Information Matrix With Approximations	Relative Difference
σ_{I_0}	30.0672	30.0588	2.81×10^{-4}
σ_V	0.0119	0.0119	3.89×10^{-7}
σ_{L-I}	0.1466	0.1466	1.62×10^{-6}
σ_{L-II}	0.0027	0.0027	4.05×10^{-7}
$\sigma_{\varphi-I}$	1.0989	1.0989	1.60×10^{-6}
$\sigma_{\varphi-II}$	0.0200	0.0200	3.81×10^{-7}

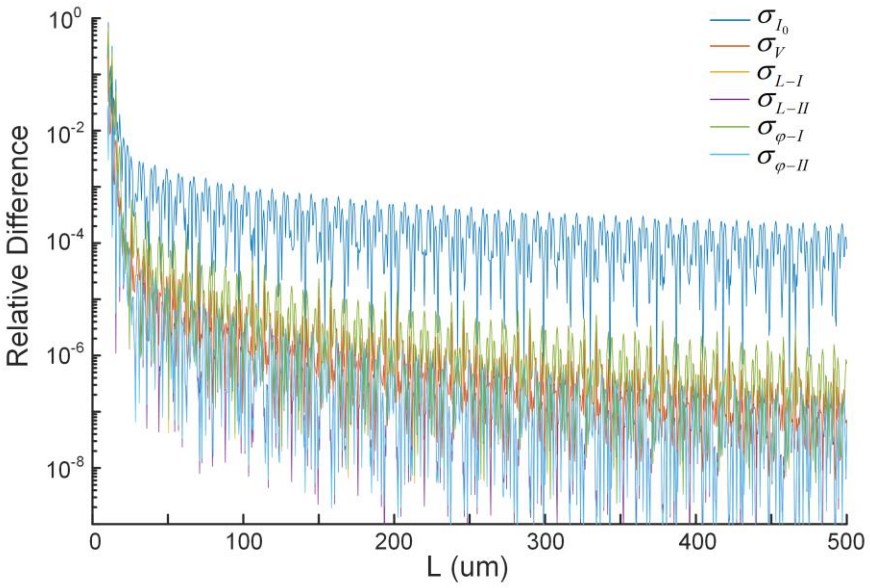

Figure 5.2. Relative difference between CRBs calculated from accurate Fisher information matrix and approximated Fisher information matrix with different OPLs.

While the accuracy of the approximation may vary with the simulation parameters, especially OPL, which determines the number of sinusoid periods in the interference signal, simulations using same parameters but varying the OPLs are further demonstrated, as shown in Fig. 5.2. The relative differences between CRBs for V, L and φ from accurate to approximated Fisher information matrix can be smaller than 10^{-4} when L is relatively large. And the CRB

relative difference for I_0 is the largest among all unknown parameters but is still desirable, which means our approximations are efficient and the CRBs derived above are exceptionally accurate.

5.5. Conclusion

In summary, we derive the CRBs of parameter estimation using a realistic interference signal model with background spectral envelope and initial phase term. The detected spectrum is modeled with three noise components with different statistical behaviors, corresponding to shot noise, dark noise and readout noise respectively. By using a Poisson RV to approximate the complete model, CRBs are derived to provide additional insights into the statistical behavior of this multi-parameter estimation problem.

In particular, we investigate how other unknown parameters in the model change the sensitivity limit of OPL estimation. For shot noise-limited case, when CRBs for different sets of unknown parameters are compared, the system sensitivity limit for OPL (frequency) estimation is shown to be unrelated to the knowledge of spectral intensity or fringe visibility, while only depending on whether the initial phase is known or not. This is consistent with our empirical experience in interference signal processing, where the knowledge of intensity and visibility is never used in estimating OPL [1, 2]. For OPL estimation, cases of known initial phase (Type II demodulation) show significant sensitivity advantage over cases of unknown or unused initial phase (Type I demodulation). The sensitivity advantage is derived with theoretical analysis using shot noise-limited model and is further quantified as significant based on numerical simulations. This suggests that, for high sensitivity OPL measurements, the initial phase should be determined or at least estimated and that Type II demodulation should be the choice.

In addition to theoretical significance, a practical application of CRBs reported in this chapter is for system evaluation and optimization [17, 18]. From acquired spectra, one can calculate the CRBs and use them as target performance indicators of the algorithm efficiency and system efficiency [18]. For example, our previous study has revealed that the typical Fourier-transform based OPL algorithm underperforms as compared to CRB [17]. Its algorithm sensitivity can be as much as $\sqrt{2}$ times worse than CRB for high visibility interference signals. The results here show that this conclusion is also valid for the general interference signal model.

Such discrepancy is likely due to the negligence of noise statistics in the signal processing algorithm. The theoretical discussions in this chapter provide insights into the behavior of this estimation problem and may potentially point out ways toward better estimation procedures.

References

[1] C. Ma and A. Wang, "Signal processing of white-light interferometric low-finesse fiber-optic Fabry-Perot sensors," *Applied Optics,* vol. 52, no. 2, pp. 127-138, Jan 2013.

[2] F. Shen and A. Wang, "Frequency-estimation-based signal-processing algorithm for white-light optical fiber Fabry-Perot interferometers," *Applied Optics,* Article vol. 44, no. 25, pp. 5206-5214, Sep 2005.

[3] S. Kay, "A fast and accurate single frequency estimator," *IEEE Transactions on Acoustics, Speech, and Signal Processing,* vol. 37, no. 12, pp. 1987-1990, 1989.

[4] S. Tretter, "Estimating the frequency of a noisy sinusoid by linear regression ," *IEEE Transactions on Information Theory,* vol. 31, no. 6, pp. 832-835, 1985.

[5] D. Rife and R. Boorstyn, "Single tone parameter estimation from discrete-time observations," *IEEE Transactions on Information Theory,* vol. 20, no. 5, pp. 591-598, 1974.

[6] P. Stoica and A. Nehorai, "MUSIC, maximum likelihood, and Cramer-Rao bound," *IEEE Transactions on Acoustics Speech and Signal Processing,* vol. 37, no. 5, pp. 720-741, May 1989.

[7] J. Schwider and L. Zhou, "Dispersive interferometric profilometer," *Optics Letters,* vol. 19, no. 13, pp. 995-997, Jul 1994.

[8] L. Deck and P. Degroot, "High-speed noncontact profiler based on scanning white-light interferometry," *Applied Optics,* vol. 33, no. 31, pp. 7334-7338, Nov 1994.

[9] Y. Zhu and A. Wang, "Miniature fiber-optic pressure sensor," *IEEE Photonics Technology Letters,* vol. 17, no. 2, pp. 447-449, 2005.

[10] A. Wang, H. Xiao, J. Wang, Z. Wang, W. Zhao, and R. May, "Self-Calibrated Interferometric-Intensity-Based Optical Fiber Sensors," *Journal of Lightwave Technology,* vol. 19, no. 10, p. 1495, Oct 2001.

[11] R. Shang, S. Chen, C. Li, and Y. Zhu, "Spectral modulation interferometry for quantitative phase imaging," *Biomedical Optics Express,* vol. 6, no. 2, pp. 473-479, Feb 2015.

[12] M. V. Sarunic, S. Weinberg, and J. A. Izatt, "Full-field swept-source phase microscopy," *Optics Letters,* vol. 31, no. 10, pp. 1462-1464, May 2006.

[13] M. Choma, A. Ellerbee, C. Yang, T. Creazzo, and J. Izatt, "Spectral-domain phase microscopy," *Optics Letters,* vol. 30, no. 10, pp. 1162-1164, May 2005.

[14] L. Lepetit, G. Chériaux, and M. Joffre, "Linear techniques of phase measurement by femtosecond spectral interferometry for applications in spectroscopy," *Journal of the Optical Society of America B,* vol. 12, no. 12, pp. 2467-2474, Dec 1995.

[15] S. Djukanović, "An Accurate Method for Frequency Estimation of a Real Sinusoid," *IEEE Signal Processing Letters,* vol. 23, no. 7, pp. 915-918, 2016.

[16] D. Snyder, C. Helstrom, A. Lanterman, R. White, and M. Faisal, "Compensation for readout noise in CCD images," *Journal of the Optical Society of America A,* vol. 12, no. 2, pp. 272-283, Feb 1995.

[17] C. Li and Y. Zhu, "Cramer-Rao Bound for Frequency Estimation of Spectral Interference and Its Shot Noise-Limited Behavior," *IEEE Journal of Selected Topics in Quantum Electronics,* vol. 23, no. 2, pp. 1-7, 2017.

[18] S. Chen, J. Ryu, K. Lee, and Y. Zhu, "Swept source digital holographic phase microscopy," *Optics Letters,* vol. 41, no. 4, pp. 665-668, Feb 2016.

Chapter 6 Maximum Likelihood Estimation of Optical Pathlength in Spectral Interferometry

Optical pathlength demodulation is a subject of fundamental importance in spectral interferometry applications. We propose an algorithm based on maximum likelihood estimation to achieve absolute optical pathlength demodulation with high sensitivity and noise resistance, and to elucidate the cause and behavior of undesirable demodulation discontinuity. From an interference spectrum model with additive Gaussian noise, a maximum likelihood estimator is derived in Fourier domain to determine the optical pathlength. To assess its sensitivity performance, the Cramer-Rao bound of sensitivity is derived from Fisher information matrix. By simulations and experimental validations, the proposed method demonstrates its capability of achieving the Cramer-Rao bound over a large dynamic range of optical pathlengths, initial phases and signal-to-noise ratios. When compared with some state-of-the-art demodulation methods, it also demonstrates improved resistance to demodulation jumps at low signal-to-noise ratios. Importantly, the mechanism of such jumps can be readily explained from a new, intuitive perspective, which may permit the quantification of jump occurrences in the future.

6.1. Introduction

Spectral interferometry has proved to be an effective approach for measuring optical pathlength (OPL) with exquisite sensitivity and wide dynamic range. Its application can be found in many areas such as fiber-optic sensing [1, 2], optical metrology [3], phase microscopy [4, 5], and femtosecond spectroscopy [6]. The demodulation of two beam interference in spectral domain is fundamentally a frequency estimation problem for periodic discrete signals. The majority of current methods for sinusoidal frequency estimation address complex sinusoids in signal processing and communications [7-9]. In spectral interferometry, however, the interference spectra are discrete, real-valued sequences, often with an additional initial phase term. Although substantial progress has been made in the past to accurately demodulate OPL [10], much remains to be investigated. For example, how to obtain absolute OPLs with the

highest sensitivity and no demodulation discontinuity ("jump")? How to understand the origin of such jumps, and to predict and minimize its occurrence? Addressing these questions is critical for optimizing demodulation performance.

6.2. Interference Spectrum Model and Existing Algorithms

For a typical two-beam spectral interferometry, we can consider a sinusoidal signal model of the interference spectrum:

$$I_n = A\cos\left(k_n L_0 + \phi\right) + C, n = 0, 1, ..., N-1, \quad \textbf{(6.1)}$$

where amplitude A and offset C determine the interference fringe visibility $V = A/C$, k_n represent the wavenumber, L_0 denotes the OPL which is the subject of estimation, and ϕ represents the initial phase, the value of which depends on the specific type of the interferometer. We use Φ_n to denote the total phase of the spectrum, i.e. $\Phi_n = k_n L_0 + \phi$. A representative spectrum is shown in Fig. 6.1(a) with its discrete Fourier transform (DFT) in Fig. 6.1(b).

To date, a number of efficient algorithms have been proposed to demodulate the OPL (frequency) of an interference spectrum. They can be classified into two types based on the treatment of ϕ [10]. In Type I frequency estimation, ϕ is either unknown or unused. These algorithms are fundamentally equivalent to finding the interference peak position in DFT, as shown in Fig. 6.1(b). However, the OPL sensitivity of Type I demodulation is poor. In contrast, Type II estimation takes advantage of the knowledge of ϕ, and is equivalent to finding the phase of the interference peak in DFT. It attains significant sensitivity improvement of 1-2 orders of magnitude over Type I estimation. In this chapter, we will focus on Type II estimations.

The value of ϕ is typically determined by the structure of an interferometer. For example, $\phi = 0$ for a standard Michelson or Mach-Zehnder interferometer when the two interference arms are perfectly symmetric. However, different surface materials or transmission media may give rise to a non-zero initial phase. It becomes more complicated in some other cases, such as fiber-optic interferometric sensors, where ϕ depends on multimode propagation [11] or beam divergence in an extrinsic Fabry-Perot cavity [12]. For these applications, a physical model is needed to theoretically estimate ϕ.

Thanks to its sensitivity advantage, Type II estimation has become the dominant signal processing scheme for spectral interferometry with a variety of algorithms proposed. As mentioned above, a direct implementation is the Fourier domain peak phase (FDPP) method, which extracts the phase at a fixed position on the interference peak in Fourier domain, and then converts it to OPL. In order to maximize signal-to-noise ratio (SNR) and sensitivity, a zero-padded DFT is often used to locate the peak position more precisely, indicated by point C in Fig. 6.1(c) as compared to points A and B in the non-zero-padded, non-interpolated DFT. A major drawback of FDPP is that it produces only a relative OPL due to phase wrapping, thus severely limiting its dynamic range. In addition, when the peak starts to shift away from the selected position, SNR and OPL sensitivity will deteriorate.

To obtain absolute OPL, a linear regression (LR) or least squares fitting method is developed in [13, 14]. The algorithm starts with using a band-pass filter to select the single-band interference component $\frac{A}{2}e^{j(k_n L_0+\phi)}$, as illustrated in Fig. 6.1(d). The phase of the filtered analytic signal is then extracted and unwrapped. There is a difference of $2m\pi$ between the unwrapped phase and the total phase Φ_n, with m being an integer to be solved for. A linear least square fitting follows next to decide m using the unwrapped phase and k_n. The problem is equivalent to estimating the slope and the intercept of a linear phase ramp corrupted by additive noises. LR has been shown to be very accurate at high SNRs. However, a discontinuity in demodulated OPLs may occur when, under noises, the estimation of m incorrectly jumps to adjacent integers. Although it has been shown that such OPL jump originates from the initial phase ϕ [14], the detailed mechanism and behavior have yet to be thoroughly understood. Additionally, how to practically solve the 2π ambiguity to minimize jump occurrence requires further investigation.

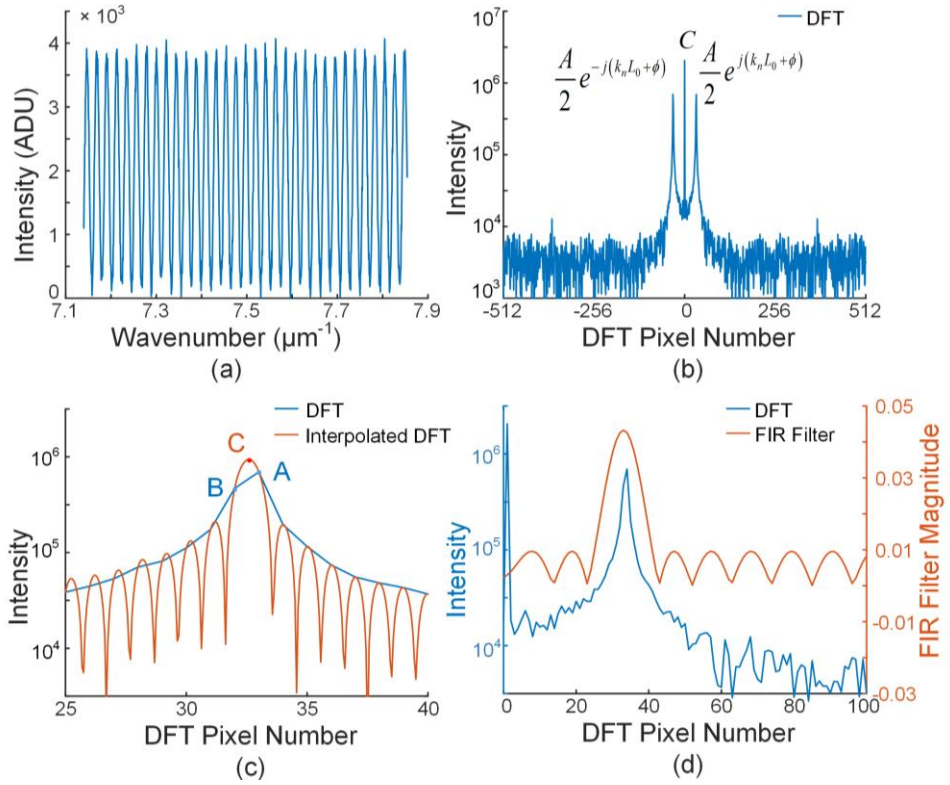

Figure 6.1. (a) Simulated interference spectrum with Gaussian noise (in analog-to-digital unit, ADU), SNR 20dB. (b) DFT of the spectrum in (a). (c) Comparison between non-interpolated DFT and interpolated DFT. (d) Finite Impulse Response (FIR) filter designed for LR algorithm.

In addition to LR, a fast peak locating (FPL) method was developed recently for high-speed demodulation of absolute OPL [15]. The FPL algorithm only utilizes non-zero-padded DFT spectrogram, avoiding the time-consuming interpolation step. First, two adjacent points on the interference peak, shown as A and B in Fig. 6.1(c), are selected for a coarse peak position calculation employing Buneman frequency estimation method. Next, the 2π ambiguity in Φ_n is determined using known ϕ. The precise peak position is then located with the solved m, known ϕ, and the phase of peak point B in Fig. 6.1(c). FPL offers impressive real-time demodulation speed of 70kHz on a typical laptop computer, but its sensitivity performance has not yet been studied. As we will show later, the algorithm suffers sensitivity degradation, sometimes severe, because the SNR at point B is lower than that at point C and fluctuates widely as OPL shifts.

For an interferometry-based OPL demodulation algorithm aimed at high sensitivity, such as FDPP, LR and FPL, OPLs must be sufficiently large to introduce enough fringe density into

the interference spectrum. This will allow the interference peaks in Fourier domain to be clearly separated from DC component. As a result, they are insensitive to changes in the spectral envelope of the light source, and are capable of multi-peak detection. In contrast, if only a few fringes exist in the interference spectrum, algorithms based on spectral domain fringe analysis will be better choices, but are considerably limited in resolution, accuracy, as well as robustness and flexibility [16, 17].

In this chapter, to achieve absolute OPL demodulation with high sensitivity and minimized OPL demodulation jump occurrence, a new method based on maximum likelihood (ML) estimation is proposed. In Section 6.3, the ML estimator is derived based on an interference model with additive Gaussian noises and described in detail. Cramer-Rao bound (CRB) is obtained and compared with the algorithm sensitivity of FDPP and FPL in Section 6.4. Section 6.5 validates the sensitivity analysis using simulations and demonstrates the ML method's capability of achieving CRB across a large dynamic range of OPLs. Significantly, the ML estimator offers a clear, intuitive interpretation of the cause and behavior of the OPL jumps. In Section 6.6, the sensitivity advantage of the ML algorithm is experimentally verified.

6.3. Maximum Likelihood Estimator and Signal Processing Algorithm

6.3.1. Signal and noise model

Let $\boldsymbol{S} = \left[S_{\mathbf{0}}, S_{\mathbf{1}}, S_{\mathbf{2}}, ..., S_{N-\mathbf{1}}\right]$ represent a detected spectrum corrupted by Gaussian noise W_n, where

$$S_n = I_n + W_n = A\cos\left(k_n L_{\mathbf{0}} + \phi\right) + C + W_n, \;\; n = \mathbf{0}, \mathbf{1}, ..., N - \mathbf{1}. \tag{6.2}$$

The quantities in Eq. (6.2) are all real-valued and evenly spaced by a constant sampling interval of δk defined by

$$k_n = k_{\mathbf{0}} + n\delta k = \left(n_{\mathbf{0}} + n\right)\delta k. \tag{6.3}$$

It should be noted that, for most optical spectral interferometry applications, $n_{\mathbf{0}} \gg N$, and $n_{\mathbf{0}}$ is not necessarily an integer. Without loss of generality, for interference spectra originally not evenly sampled in wavenumber, various interpolation approaches have been developed to

yield equal sampling interval in wavenumber to take advantage of standard signal processing techniques [18, 19]. The minimized interpolation error has been shown with negligible influence on demodulation quality [10] and will not be discussed here.

The noise components W_n are assumed to be independent identically distributed Gaussian noises with zero mean and a variance of σ^2. The SNR can then be defined as $A^2/2\sigma^2$.

The goal of signal processing in spectral interferometry is to estimate the carrier frequency L_0 from an interference signal I_n corrupted by the noise W_n. With $\boldsymbol{S}$ and ϕ provided as input, the OPL estimation generated by the proposed estimator is denoted as $\hat{L}$, which can be seen as an unbiased estimator (at least at high SNRs) [8].

6.3.2. Maximum likelihood estimator

With the unknown parameter L_0 and the independent Gaussian random variables, the probability density function of $\boldsymbol{S}$ for L is given by

$$f\left(\boldsymbol{S};L\right)=\left(\frac{1}{\sigma\sqrt{2\pi}}\right)^{N}\exp\left[-\frac{1}{2\sigma^{2}}\sum_{n=0}^{N-1}\left(S_n-I_n\right)^{2}\right]. \tag{6.4}$$

The ML estimator maximizes $f\left(\boldsymbol{S};L\right)$ as well as its logarithm $\log\left[f\left(\boldsymbol{S};L\right)\right]$, where

$$\hat{L}=\max_{L}\left\{\log\left[f\left(\boldsymbol{S};L\right)\right]\right\}=\max_{L}\left\{N\log\left(\sigma\sqrt{2\pi}\right)-\frac{1}{2\sigma^{2}}\sum_{n=0}^{N-1}\left[\begin{array}{l}S_n^{2}-2AS_n\cos\left(k_nL+\phi\right)-2CS_n+C^{2}+\\2AC\cos\left(k_nL+\phi\right)+A^{2}\cos^{2}\left(k_nL+\phi\right)\end{array}\right]\right\}. \tag{6.5}$$

Since A,C,σ,S_n are all constants once an observation has been made, we can drop all components unrelated to L so that

$$\hat{L}=\max_{L}\left\{\sum_{n=0}^{N-1}\left[S_n\cos\left(k_nL+\phi\right)\right]-\sum_{n=0}^{N-1}\left[C\cos\left(k_nL+\phi\right)\right]-\sum_{n=0}^{N-1}\left[\frac{A}{2}\cos^{2}\left(k_nL+\phi\right)\right]\right\}. \tag{6.6}$$

Furthermore, given L being sufficiently large, $\sum_{n=0}^{N-1}\left[C\cos\left(k_nL+\phi\right)\right]$ and $\sum_{n=0}^{N-1}\left[\frac{A}{2}\cos^2\left(k_nL+\phi\right)\right]$ can be well approximated by 0 and $NA/4$, respectively, and thus can also be dropped from Eq. (6.6) to produce

$$\begin{aligned}\hat{L} &= \max_{L}\left\{\sum_{n=0}^{N-1}\left[S_n\cos\left(k_nL+\phi\right)\right]\right\} = \max_{L}\left\{\mathrm{Re}\left[e^{-jk_0L}e^{-j\phi}\sum_{n=0}^{N-1}\left(S_ne^{-jn\delta kL}\right)\right]\right\} \\ &= \max_{L}\left\{\mathrm{Re}\left[e^{-jk_0L}e^{-j\phi}\mathcal{F}\left(\boldsymbol{S}\right)\right]\right\}.\end{aligned} \tag{6.7}$$

Hence the ML estimation of L is converted to the problem of finding $\hat{L}$ that, under the condition that L is large, maximizes the ML estimator M_L defined as

$$M_L = \mathrm{Re}\left[e^{-jk_0L}e^{-j\phi}\mathcal{F}\left(\boldsymbol{S}\right)\right]. \tag{6.8}$$

As shown in Fig. 6.1(b), when the frequency is high, $\mathcal{F}\left(\boldsymbol{S}\right)$ is essentially contributed by $\frac{A}{2}e^{j(k_nL+\phi)}+W_n$. To better illustrate the relationship between M_L and $\mathcal{F}\left(\boldsymbol{S}\right)$, the DFT spectrogram and the ML estimator are depicted around the frequency $\hat{L}$ with interpolation, as shown in Fig. 6.2(a). Compared with $\left|\mathcal{F}\left(\boldsymbol{S}\right)\right|$, the ML estimator has significantly higher fringe density as introduced by e^{-jk_0L} and much narrower peak width. As a result, it has a significantly higher sensitivity when locating the center position of its highest peak, as compared to finding the peak position of $\left|\mathcal{F}\left(\boldsymbol{S}\right)\right|$ in Type I demodulation. Therefore, the ML algorithm directly visualizes the sensitivity advantage of Type II demodulation.

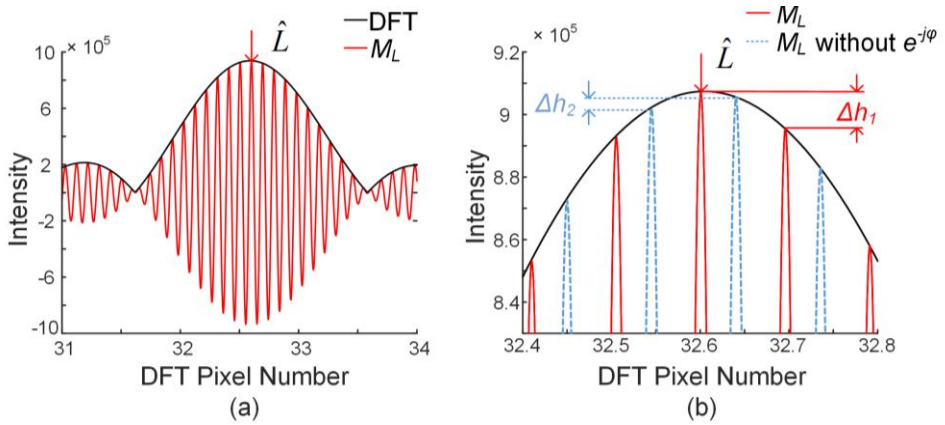

Figure 6.2. (a) $\left|\mathcal{F}\left(\boldsymbol{S}\right)\right|$ and the proposed M_L estimator. (b) The estimator with and without $e^{-j\phi}$.

Fig. 6.2(a) also illustrates the origin of demodulation jumps in OPL. In the presence of noise, there is a certain probability that an adjacent peak will be higher than the center peak and its position will be mistaken as the correct OPL, thus resulting in a demodulation jump from time to time.

Further, the knowledge of ϕ is important in the probability of jump occurrence and demodulation accuracy, because $e^{-j\phi}$ in M_L compensates the phase shift in $\frac{A}{2}e^{j(k_n L_0+\phi)}$. The ML estimators with and without $e^{-j\phi}$ are illustrated in Fig. 6.2(b) for $\phi=\mathbf{150}^\circ$. Not using $e^{-j\phi}$ is equivalent to not knowing ϕ and assuming it is $\mathbf{0}^\circ$. In this case, the highest peak will shift and lead to a systematic demodulation error in OPL. Additionally and perhaps more importantly, the height difference between the highest peak and its adjacent peak is drastically reduced from Δh_1 to Δh_2, making it easier for adjacent peaks under noise to be misidentified as the correct one and more likely to generate a jump.

In brief, an absent or inaccurate knowledge of ϕ mis-compensates the interference signal and leads to higher probability of OPL demodulation jump. With Fig. 6.2(b), a path to quantify the probability of jump is offered potentially by using peak height difference and noise statistics, although it is beyond the scope of current discussions.

6.3.3. Signal processing algorithm

With the ML estimator, the signal processing algorithm starts with computing M_L based on DFT of the interference spectrum. In practice, due to the discrete nature of the DFT, interpolation in Fourier domain is needed for locating $\hat{L}$ accurately. Therefore, a two-step approach is applied as follows.

For the first step, a coarse peak locating is performed in maximizing non-zero-padded DFT spectrogram to find A in Fig. 6.1(c). As long as we have a general knowledge of L_0 from A, M_L will be computed with high-order interpolation but only locally around the coarse peak. Compared with standard zero-padding, the algorithm complexity can be significantly reduced from $O(MN\log_2 MN)$ to $O(PMN)$, where M is the interpolation order and P is the M_L computing range in terms of DFT pixel space. For an interference spectrum of $N=\mathbf{1024}$, with $M=\mathbf{512}$ and $P=\mathbf{2}$, the time complexity of local estimator computing is equivalent to a Fast Fourier-transform (FFT) of 64 times zero-padding.

A quadratic fitting is computed afterwards given the estimator values around the peak and corresponding frequencies. The center of the quadratic fitted curve is interpreted as the fine peak position $\hat{n}$, which is in DFT pixel number. The relationship between $\hat{n}$ and $\hat{L}$ can be applied as

$$\hat{L}=\hat{n}\delta L=\hat{n}\frac{\mathbf{2}\pi}{(N-\mathbf{1})\delta k}, \tag{6.9}$$

where δL is the corresponding OPL between adjacent pixels in non-interpolated DFT.

6.4. Cramer-Rao Bound and Algorithm Sensitivity

To investigate the sensitivity performance of the proposed method compared with existing ones, we use CRB as a benchmark and also derive the algorithm sensitivity of FDPP and FPL as follows.

An unbiased estimator that achieves CRB is said to be "efficient", in the sense that it achieves the best possible performance from the given observation. Based on estimation theory [20], CRB can be derived from the Fisher Information matrix $\boldsymbol{J}_L$ for the unknown parameter L,

$$\mathrm{var}_{CRB}\left(\hat{L}\right) \geq \boldsymbol{J}_L^{-1}, \tag{6.10}$$

where $\boldsymbol{J}_L$ can be written as,

$$\boldsymbol{J}_L = E\left\{\left[\frac{\partial}{\partial L}\log f\left(\boldsymbol{S};L\right)\right]^2\right\} = \frac{A^2}{2\sigma^2}\left[\sum_{n=0}^{N-1}k_n^2 - \sum_{n=0}^{N-1}k_n^2\cos 2\left(k_n L+\phi\right)\right]. \tag{6.11}$$

The second component in Eq. (6.11) is the combination of an oscillating function. It is therefore much smaller than the first one and becomes negligible when L is sufficiently large. This is similar to the approximation applied to Eq. (6.6).

The CRB for L can then be expressed by

$$\mathrm{var}_{CRB}\left(\hat{L}\right) \geq \frac{2\sigma^2}{A^2\sum_{n=0}^{N-1}k_n^2} \cong \frac{2\sigma^2}{A^2 N k_c^{\,2}} = \frac{1}{N k_c^{\,2}}\cdot\frac{1}{SNR}, \tag{6.12}$$

where $k_c = k_0 + \frac{N-1}{2}\delta k$ denotes the center wavenumber. As expected, the variance is inversely proportional to SNR.

Even though CRB sets a theoretical limit on the OPL sensitivity, it may not necessarily be achievable by signal processing algorithms, which typically have their own sensitivity performance. Now we focus on the algorithm sensitivity of FDPP, which is also based on interpolated DFT as ML. A similar derivation without DFT interpolation has been derived in [21]. In the following we will present a more general derivation.

Here we assume the OPL corresponded peak is located at an integer pixel p in the interpolated DFT spectrogram $\mathcal{F}_i\left(\boldsymbol{S}\right)$ with $\left(M-1\right)N$ zeros padded to $\boldsymbol{S}$. This is valid since with increasingly higher order interpolation, the interference peak will eventually be close to one

integer pixel in interpolated DFT spectrogram. Therefore, finding the variance of phase at pixel p will lead to the algorithm sensitivity. Since the amplitude of the peak can be expressed as

$$\mathcal{F}_i(\boldsymbol{S})_p = \sum_{n=0}^{N-1} S_n e^{-j2\pi p\frac{n}{MN}} = \frac{NA}{2} + \sum_{n=0}^{N-1} W_n e^{-j2\pi p\frac{n}{MN}}, \tag{6.13}$$

with its phase term being approximated as the ratio between the imaginary part and the real part,

$$\angle p \cong \frac{2\sum_{n=0}^{N-1} W_n \sin\frac{2\pi pn}{MN}}{NA}. \tag{6.14}$$

The real part related to W_n in the denominator is neglected. The standard deviation of $\hat{L}$ can be derived from the variance of $\angle p$ using the center wavenumber,

$$\mathrm{var}_{\mathcal{F}_i}\left(\hat{L}\right) = \frac{\mathrm{var}_{\mathcal{F}_i}\left(\angle p\right)}{k_c^{\,2}} \cong \frac{2\sigma^2}{A^2 N k_c^{\,2}}. \tag{6.15}$$

Comparing Eq. (6.15) with Eq. (6.12), FDPP can achieve CRB when appropriate interpolation is applied.

However, for methods based on non-interpolated DFT, such as FPL, there is typically a deviation between the real OPL peak position and the pixel where phase is extracted. This discrepancy leads to a decrease of the denominator in Eq. (6.15), a larger variance for the extracted phase, and ultimately deteriorated algorithm sensitivity. The sensitivity degradation can be severe when the pixel of phase extraction deviates far from the interference peak.

6.5. Algorithm Comparison

In this section, the proposed ML method is compared with FDPP, LR and FPL using simulated interference spectra with Gaussian noises. The results will be used to validate the above sensitivity analysis and also to investigate the behavior of demodulation jump.

The interference spectra are generated using Eq. (6.2), with the OPL demodulation sensitivity calculated over 10000-sample Monte Carlo simulations. The sensitivity is defined as the standard derivation of demodulated OPLs, i.e. the square root of OPL variances. The values of the simulation parameters are as follows if not specified otherwise: $N = \mathbf{1024}$, $A = \mathbf{1800}$,

$C = \mathbf{2000}$, $\phi = \mathbf{0}^{\circ}$, $SNR = \mathbf{20}$dB, and k_n are evenly spaced by wavenumber in [800nm, 880nm]. The interference peak is located at 32.6th pixel in DFT spectrogram, with an equivalent OPL of 286.6μm.

6.5.1. Sensitivity vs. OPLs

To verify the sensitivity analysis in Section 6.4, we first evaluate the demodulation sensitivity with different OPLs. The simulations are conducted with the interference peak locating in the DFT pixel space of [30, 35], in step of 0.1. The equivalent OPL range is [263.74μm, 307.70μm].

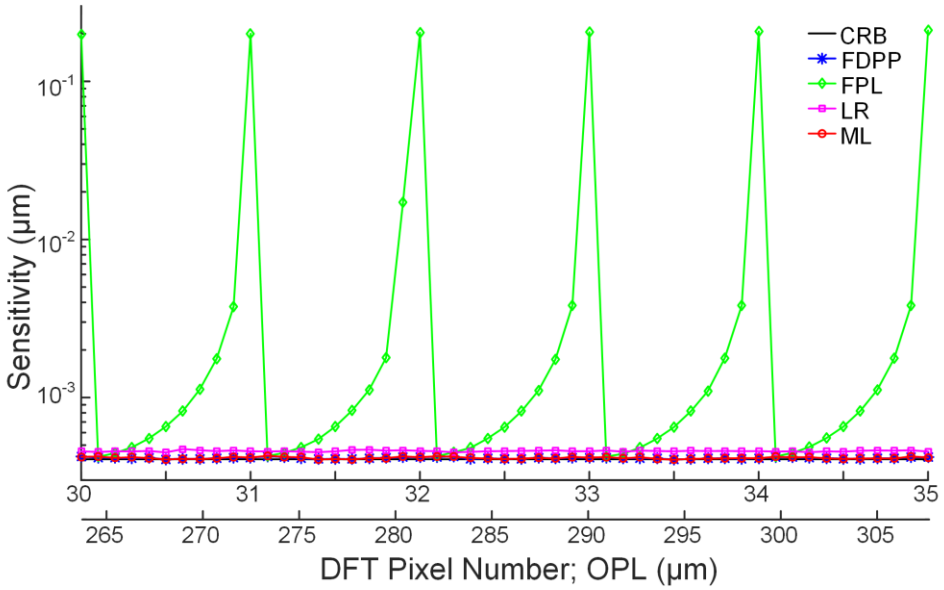

Figure 6.3. OPL demodulation sensitivity vs. OPLs. Simulated OPLs in DFT pixel space of [30, 35], in step of 0.1.

Figure 6.3 demonstrates that the proposed ML algorithm can achieve CRB for all OPLs with a 512-times locally zero-padded estimator. The CRB has also been achieved by FDPP using a 16-times interpolated DFT. However, the OPL standard deviation demodulated by FPL varies widely when the pixel of phase extraction deviates from the interference peak position. As discussed, for algorithms based on DFT but without interpolation, like FPL, the SNR of phase-extracted pixel is often weaker than the true interference peak. Using non-interpolated DFT lends FPL high demodulation speed, but at the expense of demodulation sensitivity, which can be

several times, or even up to orders of magnitude, worse than CRB. On the other hand, interpolation will improve sensitivity but cost its speed advantage.

Meanwhile, a sensitivity gap exists in the full range of simulated OPLs between LR algorithm and CRB. This gap originates from the reduced SNR of the filtered analytic signals, since some data points have to be removed on one or both edges of the spectrum either to eliminate the transition region of the filter or to suppress the ringing artifacts. Therefore, there is a trade-off between noise filtering and sensitivity, closely depending on the design of the band-pass filter.

6.5.2. Sensitivity vs. Initial Phases

The OPL demodulation sensitivity using different methods versus different initial phases are shown in Fig. 6.4. Initial phase introduces a constant shift in the phase terms of DFT. For FDPP, the standard deviation of demodulated OPLs remains the same since the variance of phase stays the same. Meanwhile, three absolute OPL demodulation methods, ML, FPL and LR, have utilized known ϕ to either shift the estimator peak back to the correct position or compensate the phase change in Φ_n to help solve $\mathbf{2}\pi$ ambiguity. As expected, all simulated algorithms show consistent sensitivity performance in the simulated range of $[\mathbf{0}, \mathbf{2}\pi]$ for ϕ.

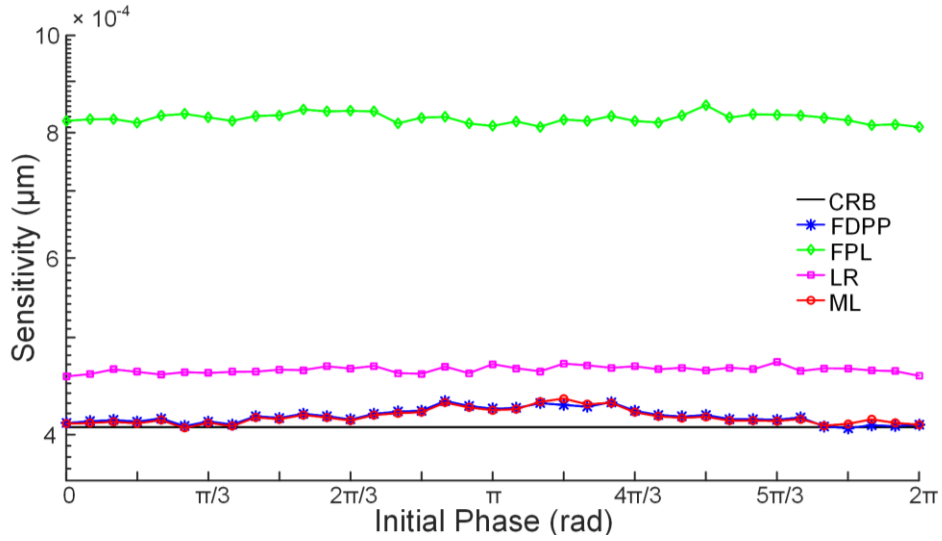

Figure 6.4. OPL demodulation sensitivity vs. initial phases. Simulated initial phase range $[\mathbf{0}, \mathbf{2}\pi]$, in step of $\pi/\mathbf{18}$.

6.5.3. Sensitivity vs. SNR

As the ML method has shown consistent sensitivity performance with different OPLs and initial phases, how the method performs with different SNRs is another important feature that needs to be examined. The SNRs are selected within [-30dB, 40dB], in step of 1dB, and the results are shown in Fig. 6.5. Consistent with Eq. (6.12), the sensitivity vs. SNR curve has a slope of -1/2 in log scale.

Based on the sensitivity behavior of ML, the simulated SNR range can be classified into three regions. In Region I, OPL demodulation can be carried out correctly by ML achieving CRB without any demodulation jump. Meanwhile, two regimes of sensitivity degradation exist for Region II and III respectively. The SNR boundary of Region I-II (5dB) reveals the algorithm's capability to avoid demodulation jumps from not able to determine the 2π ambiguity correctly. No jump occurs (or extremely rare statistically) for ML when SNRs are higher than 5dB. At the same time, the SNR boundary of Region II-III (-10dB) indicates that the introduced Gaussian noises start to become too strong for the algorithm correctly locating the OPL corresponded interference peak in Fourier domain. When the SNR is low, $\left|\mathcal{F}\left(\boldsymbol{S}\right)\right|$ will occasionally be so badly distorted that the global maximum occurs at a frequency far from L_0, which is classified as "outliners". The OPL sensitivity behavior in Region III is consistent with the outliner probability derived in [7]. It becomes increasingly worse as the SNR approaches -20dB and reaches a saturation level. And the level is determined by the width of coarse peak searching range in Fourier domain.

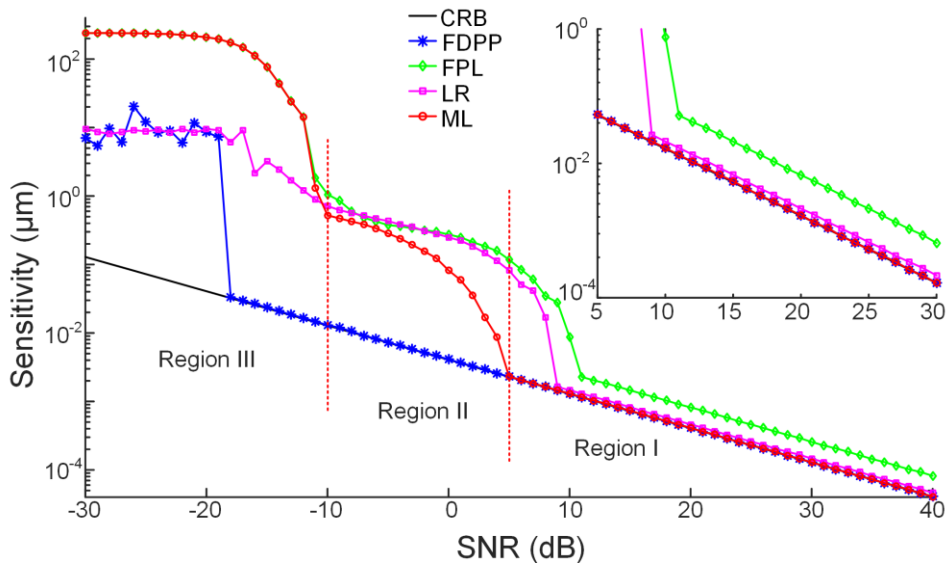

Figure 6.5. OPL demodulation sensitivity vs. SNRs. Simulated SNR range [-30dB, 40dB], in step of 1dB. Inset: a zoom-in section in Region I.

Comparing the SNR boundaries of Region I-II for three absolute OPL demodulation methods, ML demonstrates that it can work with 2.5 and 4 times larger Gaussian noises than LR (9dB) and FPL (11dB) respectively, in terms of achieving algorithm sensitivity with correct $\mathbf{2}\pi$ ambiguity determination. Therefore, ML outperforms the other two in reducing the OPL demodulation jump occurrences.

Since ML and FPL both use similar coarse peak search approach as their first step, their sensitivity behavior are quite similar in Region III. Region II-III boundary is lower for FDPP since an unwrapping procedure is applied among different simulations, which helps close the phase gap in unit of π when the phase-extracted pixel is instable.

6.5.4. Simulation on different wavenumber range

The capability of absolute OPL demodulation without jump for the proposed method is further examined using a different simulation wavenumber range in [733nm, 978nm]. The center wavenumber k_c remains the same but the wavenumber sampling interval δk is three times larger. The interference peak still locates at 32.6th pixel in Fourier domain, with the equivalent OPL now being 95.5μm. According to Eq. (6.12), the CRBs for the simulations in two

wavenumber ranges are identical. The demodulation sensitivity for each method is shown in Fig. 6.6.

The OPL demodulation sensitivity shows similar behaviors in Region I and III. However, all three absolute OPL demodulation methods, ML, LR and FPL, show significantly better resistance to OPL jumps, as the Region I-II SNR thresholds are -7dB, -3dB and -3dB respectively. The ML method still outperforms the other two with a 4dB advantage in achieving jump-free OPL demodulation.

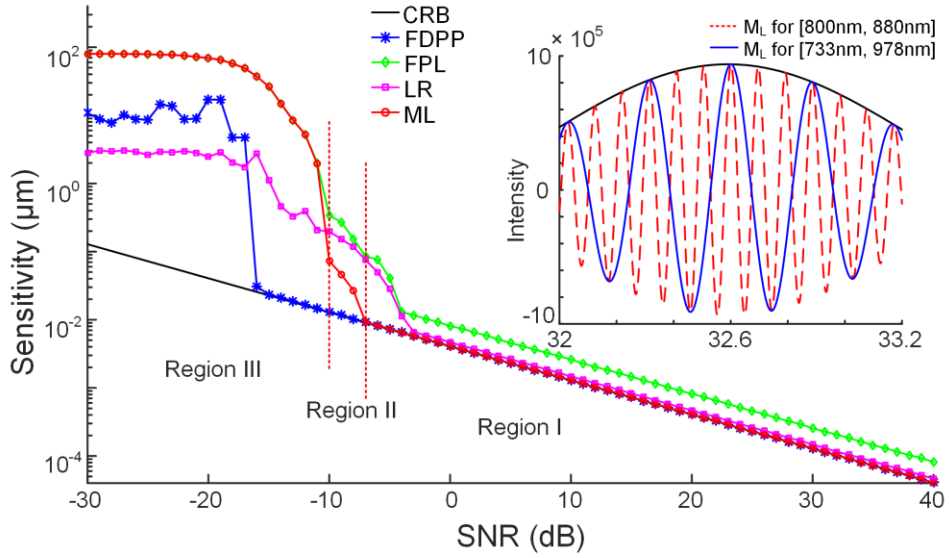

Figure 6.6. OPL demodulation sensitivity vs. SNRs with wavelength range [733nm, 978nm]. Simulated SNR range [-30dB, 40dB], in step of 1dB. Inset: The ML estimators for simulation in wavelength range of [800nm, 880nm] and [733nm, 978nm] respectively.

Compared with the simulation results in Fig. 6.5, the better performance in avoiding OPL demodulation jumps can be interpreted with the help of the estimator M_L, as shown in the inset of Fig. 6.6. With the same interference peak position $\hat{n}$ simulated, DFT envelopes are identical for two simulation setups. But a larger δk means a smaller L_0 is simulated from Eq. (6.9), and the fringe density in M_L is thus lower. Therefore, the height difference between adjacent peaks becomes larger. At same SNR level, it is significantly less likely to lead to incorrect peak identification (jump), as compared to the case of narrower wavenumber range.

The results shown in Fig. 6.6 demonstrate that, even with the same fringe density in spectral domain of the interference signal, a wider wavelength range can help to reduce the occurrences of jumps. With the proposed ML estimator, the behavior of OPL demodulation jumps can be clearly explained and be further quantified when the estimator peak height difference is evaluated with the peak magnitude variance based on given SNR. This would be critical when characterizing an OPL measurement system.

6.6. Experimental Validation

The above theory and simulation are further verified experimentally with a Michelson spectral interferometry system. The system utilizes a broadband superluminescent diode (Superlum; 837nm, FWHM 54nm) as light source, and a custom spectrometer built with a line-scan camera (e2v; EM1, 1024 pixels) as detector. The intensity of one interference arm can be adjusted to change interference visibility and SNR, similar to the simulations in Section 6.5.3. At each power level, we recorded 10000 interference spectra, with examples shown in Fig. 6.7(a). The round-trip OPL difference between the two arms is 350.4μm, with the interference peak locates around 31.68th pixel in non-zero-padded DFT spectrum.

All algorithms, FDPP, FPL, LR and ML, have been applied for OPL demodulation, using the same algorithm parameters described in Section 6.5. The demodulation results for 10000 interference spectra of group C have been illustrated in Fig. 6.7(b). While FDPP produces a relative OPL due to wrapped phase, the other three algorithms give absolute OPL results. A noticeable temporal drift is observed in all four OPL results, likely due to hardware instability yet be able to be removed through a linear fitting. In addition, there is a minor difference in the demodulated absolute OPLs from FPL, LR and ML. This may be attributed to the deviation of real interference signal from ideal model. Thus different algorithms may generate slightly different results.

Among the 12 groups of interference spectra with different interference visibilities, the corresponding SNRs have also been estimated from a peak-valley fringe analysis. The OPL demodulation sensitivity against estimated SNRs are plotted in Fig. 6.7(c). We can see that the OPL sensitivities for these four algorithms are consistent with theory (Fig. 6.5). ML can achieve the best sensitivity among the three absolute OPL demodulation algorithms, which is CRB and

can also be achieved by FDPP. Meanwhile, the sensitivities of FPL and LR are 1.64 and 1.12 times worse.

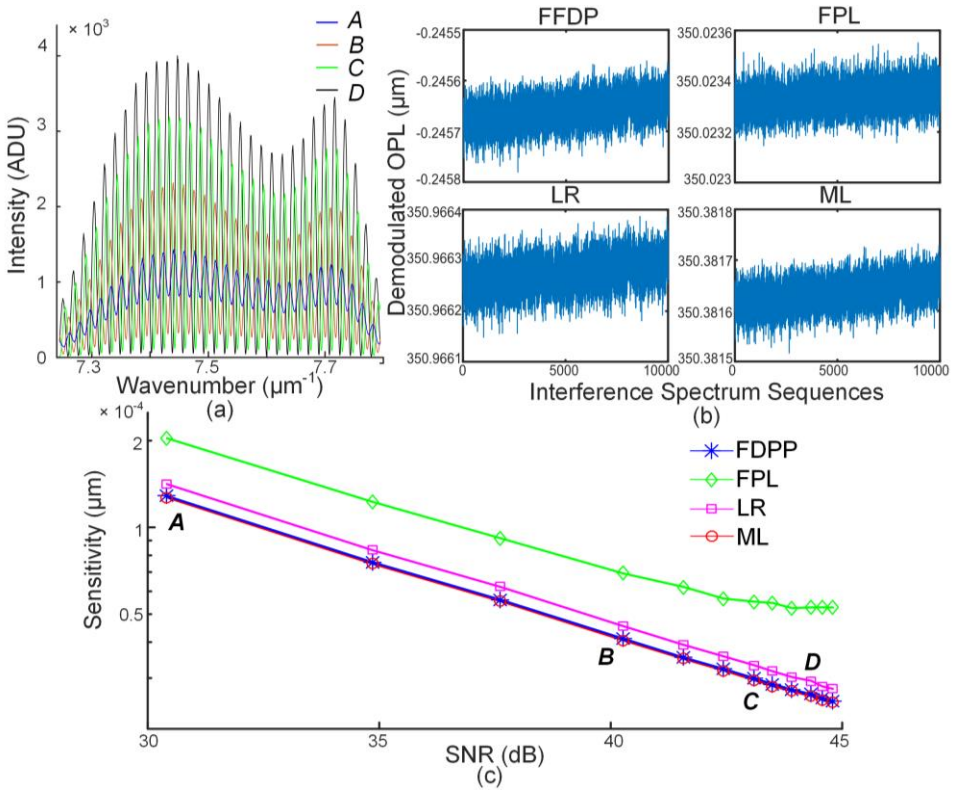

Figure 6.7. (a) Sample interference spectra with different interference visibilities. (b) Comparison of demodulated OPLs from 10000 interference spectra in group C. (c) Experimental OPL demodulation sensitivity vs. SNRs.

The averaged execution time for 10000 spectra demodulation has also been recorded, as 3.94s, 3.86s, 0.90s and 71.04s for FFDP, LR, FPL and ML, respectively. As designed, FPL achieves the best time efficiency. Our ML algorithm, which is not optimized, is 1-2 orders of magnitude slower, but is still more than adequate for offline demodulation or monitoring slower dynamics (141 spectra/sec). We believe careful algorithm optimization could improve its speed to some extent. At the same time, it is unsurprising that there will be a trade-off in speed for the advantages of the new algorithm.

Compared to sensitivity experiments, it is more complicated to experimentally confirm ML method's better resistance to demodulation jumps. This is because jumps will occur not only under low SNR, but more often so in practice when the initial phase is not accurately known and

compensated (even at high SNRs). To address the latter cause requires a challenging level of experimental control and determination of the initial phase. Nonetheless, such experiments would offer better insights into algorithm performance and are a subject of further investigation.

6.7. Conclusion

In summary, an absolute OPL demodulation estimator based on ML estimation is derived with defined interference spectrum model with Gaussian noises. The proposed algorithm maximizes the estimator and achieves CRB over a large dynamic range of OPLs and different initial phases. The main advantage of the ML algorithm is that it is the only absolute OPL demodulation method that can achieve CRB for all OPLs, when compared to FDPP, FPL and LR. This has been demonstrated with both simulations and experiments. Further, simulations show the ML method offers better noise resistance and delayed onset of OPL demodulation jumps, when compared to FPL and LR. Importantly, the ML estimator offers a clear, intuitive picture to understand and to potentially quantify the behavior of OPL demodulation jumps, which will be the subject of our further investigations. In addition, while only single-tone spectral interference is modelled and discussed in the chapter, the estimator derivation and algorithm are also valid for spatial or temporal oscillations, and may be generalized for multiplexed signals as well.

References

[1] A. Wang, H. Xiao, J. Wang, Z. Wang, W. Zhao, and R. May, "Self-Calibrated Interferometric-Intensity-Based Optical Fiber Sensors," *Journal of Lightwave Technology,* vol. 19, no. 10, p. 1495, Oct 2001.

[2] Y. Zhu and A. Wang, "Miniature fiber-optic pressure sensor," *IEEE Photonics Technology Letters,* vol. 17, no. 2, pp. 447-449, 2005.

[3] J. Schwider and L. Zhou, "Dispersive interferometric profilometer," *Optics Letters,* vol. 19, no. 13, pp. 995-997, Jul 1994.

[4] M. Choma, A. Ellerbee, C. Yang, T. Creazzo, and J. Izatt, "Spectral-domain phase microscopy," *Optics Letters,* vol. 30, no. 10, pp. 1162-1164, May 2005.

[5] P. Bon, G. Maucort, B. Wattellier, and S. Monneret, "Quadriwave lateral shearing interferometry for quantitative phase microscopy of living cells," *Optics Express,* vol. 17, no. 15, pp. 13080-13094, Jul 2009.

[6] L. Lepetit, G. Chériaux, and M. Joffre, "Linear techniques of phase measurement by femtosecond spectral interferometry for applications in spectroscopy," *Journal of the Optical Society of America B,* vol. 12, no. 12, pp. 2467-2474, Dec 1995.

[7] D. Rife and R. Boorstyn, "Single tone parameter estimation from discrete-time observations," *IEEE Transactions on Information Theory,* vol. 20, no. 5, pp. 591-598, 1974.

[8] S. Kay, "A fast and accurate single frequency estimator," *IEEE Transactions on Acoustics, Speech, and Signal Processing,* vol. 37, no. 12, pp. 1987-1990, 1989.

[9] L. Marple, "Computing the discrete-time 'analytical' signal via FFT," *IEEE Transactions on Signal Processing,* vol. 47, no. 9, pp. 2600-2603, 1999.

[10] C. Ma and A. Wang, "Signal processing of white-light interferometric low-finesse fiber-optic Fabry-Perot sensors," *Applied Optics,* vol. 52, no. 2, pp. 127-138, Jan 2013.

[11] M. Han and A. Wang, "Exact analysis of low-finesse multimode fiber extrinsic Fabry-Perot interferometers," *Applied Optics,* vol. 43, no. 24, pp. 4659-4666, Aug 2004.

[12] C. Ma, B. Dong, J. Gong, and A. Wang, "Decoding the spectra of low-finesse extrinsic optical fiber Fabry-Perot interferometers," *Optics Express,* vol. 19, no. 24, pp. 23727-23742, Nov 2011.

[13] S. Tretter, "Estimating the frequency of a noisy sinusoid by linear regression," *IEEE Transactions on Information Theory,* vol. 31, no. 6, pp. 832-835, 1985.

[14] F. Shen and A. Wang, "Frequency-estimation-based signal-processing algorithm for white-light optical fiber Fabry–Perot interferometers," *Applied Optics,* vol. 44, no. 25, pp. 5206-5214, 2005.

[15] Z. Yu and A. Wang, "Fast White Light Interferometry Demodulation Algorithm for Low-Finesse Fabry–Pérot Sensors," *IEEE Photonics Technology Letters,* vol. 27, no. 8, pp. 817-820, 2015.

[16] V. Bhatia, K. Murphy, R. Claus, T. Tran, and J. Greene, "Recent developments in optical-fiber-based extrinsic Fabry-Perot interferometric strain sensing technology," *Smart Materials and Structures,* vol. 4, no. 4, p. 246, 1995.

[17] B. Qi *et al.*, "Novel data processing techniques for dispersive white light interferometer," *Optical Engineering,* vol. 42, no. 11, pp. 3165-3171, 2003.

[18] H. Hsieh and H. Andrews, "Cubic splines for image interpolation and digital filtering," *IEEE Transactions on Acoustics, Speech, and Signal Processing,* vol. 26, no. 6, pp. 508-517, 1978.

[19] T. Schanze, "Sinc interpolation of discrete periodic signals," *IEEE Transactions on Signal Processing,* vol. 43, no. 6, pp. 1502-1503, 1995.

[20] S. Kay, "Fundamentals of statistical signal processing, volume I: estimation theory," 1993.

[21] C. Li and Y. Zhu, "Cramer-Rao Bound for Frequency Estimation of Spectral Interference and Its Shot Noise-Limited Behavior," *IEEE Journal of Selected Topics in Quantum Electronics,* vol. 23, no. 2, pp. 1-7, 2017.

Chapter 7 Conclusion and Future Work

Overall, the entire study covered the following aspects: 1) quantitative birefringence imaging based on spectral multiplexing interferometry method; 2) multimodal quantitative phase and birefringence imaging with removable Nomarski prism; 3) quantitative birefringence spectroscopy technique for single anisotropic nanoparticle orientation and polarizability measurement; 4) theoretical sensitivity limit for spectral interference spectrum demodulation; 5) novel optical pathlength demodulation method based on maximum likelihood estimation.

There are still several remaining tasks around the topic, and hopefully the topics can be addressed in future. On the application front, with our integrated quantitative phase and anisotropy imaging systems, the scattering, phase and birefringence information can provide us different ways to evaluate the specimens. For example, we can trace the dry mass and birefringence distribution changes in sperm cells or thin collagen tissues, which can be used to reveal the internal structure, to evaluate tissue quality and to monitor biophysical process. In another direction, birefringence spectroscopy of different anisotropic nanoparticles can be further investigated. We believe the exquisite sensitivity provided by our multimodal imaging system can certainly help discover more and more interesting microscopic behaviors. In addition to explore the applications, designing a commercial microscope add-on component that achieves same function, will make more impact for research/industry applications.

In terms of spectral interference signal processing, our previous work reveals that, for shot-noise limited interference spectrum, current Fourier transform-based algorithm achieves CRB for low fringe visibility cases, while it is up to $\sqrt{2}$ times worse than CRB for high visibility cases. The performance gap suggests higher sensitivity may be possible with the same data. Although algorithms achieving CRB are not guaranteed to exist, it should be pointed out that current algorithms could potentially be improved considering that none has taken advantage of all available information such as noise statistics. Such additional information, if properly utilized, may produce sensitivity close or identical to CRB. It may also be argued that algorithms that do not consider noise statistics will have performance deficiency similar to that of the FT algorithm. Given these considerations and the potential benefits of achieving CRB, methods of improvement are worth investigating.